


Spring 5-2022

The Use of Spectral Imaging to Reveal Inorganics and Organics Identity in The Biological Samples

Qamar Alshammari

Chapman University, qalshammari@chapman.edu

Follow this and additional works at: https://digitalcommons.chapman.edu/pharmaceutical_sciences_dissertations

 Part of the [Investigative Techniques Commons](#), [Nanomedicine Commons](#), and the [Other Pharmacy and Pharmaceutical Sciences Commons](#)

Recommended Citation

Alshammari, QA. *The Use of Spectral Imaging to Reveal Inorganics and Organics Identity in The Biological Samples*. [dissertation]. Irvine, CA: Chapman University; 2022. <https://doi.org/10.36837/chapman.000341>

This Dissertation is brought to you for free and open access by the Dissertations and Theses at Chapman University Digital Commons. It has been accepted for inclusion in Pharmaceutical Sciences (PhD) Dissertations by an authorized administrator of Chapman University Digital Commons. For more information, please contact laughtin@chapman.edu.

The Use of Spectral Imaging to Reveal Inorganics and Organics
Identity in The Biological Samples

A Dissertation by
Qamar Aqeel Alshammari

Chapman University

Irvine, CA

School of Pharmacy

Submitted in partial fulfillment of the requirements for the degree of

Doctor of Philosophy in Pharmaceutical Sciences

May 2022

Committee in charge:

Surya M. Nauli, Ph.D., Chair

Aftab Ahmed, Ph.D.

Ajay Sharma, Ph.D.

Amir Ahsan, Ph.D.

The dissertation of Qamar Aqeel Alshammari is approved.

Surya Nauli

Surya M. Nauli, Ph.D., Chair

Aftab Ahmed

Aftab Ahmed, Ph.D.

Ajay Sharma

Ajay Sharma, Ph.D.

Amir Ahsan

Amir Ahsan, Ph.D.

October 2021

The use of spectral imaging to reveal inorganics and organics identity in
the biological samples

Copyright © 2022

by Qamar Aqeel Alshammari

ACKNOWLEDGEMENTS

I'm thankful to Allah Almighty, who blesses me with sound health, knowledge, abilities, and gives me the chance and strength to perform and finish my research in a successful manner. My gratefulness and appreciation are extended to the following persons who have contributed in making this dissertation possible.

Firstly, I would like to express my sincere appreciation to my respected advisor Prof. Surya Nauli, for giving me the opportunity to join his lab. I'm thankful for his instructions, encouragement, and guidance that have benefited in the accomplishment of my Ph.D. study; he gave his attentions, timely suggestions and enthusiasms which allowed me to complete my Ph.D. dissertation. He is a wonderful person and the greatest scientist I've ever met. I'm very thankful for having such a smart and distinguished mentor like him.

I would also like to thank the other members of my committee, Dr. Aftab Ahmed, Dr. Ajay Sharma, and Dr. Amir Ahsan for their valuable recommendations and comments which have been beneficial for the study. I would like to thank my friends and lab mates at Chapman University for their support and advice.

My special thanks go to my husband Saud, who has been extremely supportive of me throughout these entire years, his countless love, advice, and sacrifice helped me to complete my Ph.D. dissertation. I dedicate this dissertation to my lovely sons Azzam and Abdulaziz, for their tolerance and being a source of happiness and delight in my life. I submit my heartiest gratitude to my parents and family members, who have been a source of encouragement and emotional support. I'm thankful for their prayers throughout my years of study, giving me the strength to finish this dissertation.

Finally, my best appreciations to Northern Border University, Saudi Arabia, for providing me the academic scholarship and financial support during my studies at Chapman University.

VITA

Education

- Master's degree in Pharmaceutical Sciences from School of Pharmacy at Chapman University in 2019, Irvine, United States.
- Pharm D. degree from Faculty of Pharmacy at Northern Border University in 2016, Saudi Arabia.

Academic Employment:

Lecturer in Pharmacology department – Faculty of Pharmacy, Northern Border University, Saudi Arabia.

Publications:

- **Alshammari, Q. A.**, Pala, R., Barui, A. K., Alshammari, S. O., Nauli, A. M., Katzir, N., Mohieldin, A. M., & Nauli, S. M. (2022). The use of advanced spectral imaging to reveal nanoparticle identity in biological samples. *Nanoscale*, 14(11), 4065–4072. <https://doi.org/10.1039/D1NR07551A>.
- **Alshammari, Q. A.**, Pala, R., Katzir, N., & Nauli, S. M. (2021). Label-free spectral imaging to study drug distribution and metabolism in single living cells. *Scientific reports*, 11(1), 2703. <https://doi.org/10.1038/s41598-021-81817-0>.
- Pala, R., Jamal, M., **Alshammari, Q.**, & Nauli, S. M. (2018). The Roles of Primary Cilia in Cardiovascular Diseases. *Cells*, 7(12), 233. <https://doi.org/10.3390/cells7120233>.
- Riahifard, N., Mozaffari, S., Aldakhil, T., Nunez, F., **Alshammari, Q.**, Alshammari, S., Yamaki, J., Parang, K., & Tiwari, R. K. (2018). Design, Synthesis, and Evaluation of Amphiphilic Cyclic and Linear Peptides Composed of Hydrophobic and Positively-Charged Amino Acids as Antibacterial Agents. *Molecules (Basel, Switzerland)*, 23(10), 2722. <https://doi.org/10.3390/molecules23102722>.

ABSTRACT

The use of spectral imaging to reveal inorganics and organics identity in the biological samples

by Qamar Aqeel Alshammari

The wavelength is used to identify the exact location and quantify the number of molecules in the spectral imaging system. It aids in identifying materials and studying their quantities by examining how they interact with light. A traditional spectrometer provides spectrum information of chemical compounds, while standard imaging provides the intensity at each pixel of the image. Spectral imaging (SI) combines these two aspects by equipping intensity and spectral data for each pixel. In biomedical research, it is important to assess the inorganics/organics molecules to understand drug activity, cellular toxicity, and distribution. Using the microscopy technique, we found for the first time that spectral imaging can provide a high temporal and spatial resolution of gold (Au) and silver (Ag) nanoparticles (NPs) in fixed, living cells and tissue samples. We discovered that SI has a tremendous potential to study NPs localization and identification in biological samples at a single living cell and tissue, based primarily on the spectra information. In addition, we revealed for the first time that without labeling the drug and destroying the samples, spectral imaging is a novel method that allows us to analyze the dynamics of drug distribution and metabolism in single living cells. The spectral microscopy provides a high image resolution to track and identifies doxorubicin (dox) metabolite, which is doxorubicinol (dox'ol). The microscopy approach confirms that both dox and dox'ol are translocated to the nucleus at different rates, while rhodamine remains in the cytoplasm.

TABLE OF CONTENTS

	<u>Page</u>
ACKNOWLEDGEMENTS	IV
VITA.....	V
ABSTRACT.....	VI
LIST OF TABLES	IX
LIST OF FIGURES	X
LIST OF ABBREVIATIONS	XII
CHAPTER 1: LABEL- FREE NANOPARTICLES OVERVIEW	1
1.1 Introduction.....	1
1.2 Therapeutics based on NPs approved for clinical use	3
1.3 Metallic NPs and their application.....	5
1.4 Approaches to detect label-free NPs.....	7
References.....	11
CHAPTER 2: THE USE OF SPECTRAL IMAGING TO REVEAL NANOPARTICLE IDENTITY IN THE BIOLOGICAL SAMPLES	20
2.1 Abstract.....	20
2.2 Introduction.....	21
2.3 Materials and Methods.....	23
2.4. Results.....	32
2.5 Discussion.....	50
2.6 Conclusion	52
References.....	53
CHAPTER 3: IDENTIFICATION OF ORGANICS METABOLITE VERSION... 58	
3.1 Abstract.....	58
3.2 Introduction.....	59
3.3 Materials and Methods.....	61
3.4 Results.....	70
3.5 Discussion.....	83
3.6 Conclusion	85
References.....	86
CHAPTER 4: SUMMARY	90
Future Directions:	91

SUPPLEMENTARY INFORMATION..... 92

LIST OF TABLES

	<u>Page</u>
Table 1-1: Nanoparticle-based medicines that have been approved clinically.....	4
Table 1-2: Metallic nanoparticles applications.....	5
Table 2-1: H&E staining steps.....	30

LIST OF FIGURES

	<u>Page</u>
Figure 1-1: Different type of commonly used nanoparticles	2
Figure 2-1: Identification of Ag(s)-NPs Spectra.....	34
Figure 2-2: Identification of Ag-NPs Spectra.....	35
Figure 2-3: Identification of Au-NPs Spectra.....	37
Figure 2-4: Time-lapse Imaging of Ag(s)-NPs.....	39
Figure 2-5: Time-lapse Imaging of Au-NPs	41
Figure 2-6: TEM & Silver Staining of Ag(s)-NPs and Ag-NPs	42
Figure 2-7: TEM & Silver Staining of AuNPs	43
Figure 2-8: Distribution of Ag(s)-NPs in Animal Tissues.....	45
Figure 2-9: Distribution of AgNPs in Animal Tissues	46
Figure 2-10: Distribution of AuNPs in Animal Tissues	47
Figure 2-11: Correlation analysis of Ag(s)-NP and Ag-NP distributions in the tissues using spectral imaging and ICP-MS.....	48
Figure 2-12: Correlation analysis of AuNP distributions in the tissues using spectral imaging and ICP-MS.....	49
Figure 3-1: Diagram of the spectral microscopy set-up.....	66
Figure 3-2: Diagram of Dox Converted to Dox'ol at the Side Chain of the C-13 Carbonyl Group.....	68
Figure 3-3: Spectral Imaging on dox'ol.....	72
Figure 3-4: Analysis of linearity of dox'ol in spectral imaging.....	74
Figure 3-5: Time-lapse Imaging for The Cells That Treated With 1 nM Dox.	76
Figure 3-6: Line Graphs Represent Dox Wavelengths at Different Time Points.	78
Figure 3-7: Linear Regression Analysis of Dox'ol Cell-free & Dox Cell Lysate	79
Figure 3-8: Curve-fit Analyses of Time-lapse Imaging for The Cells Treated With Dox	81

Figure 3-9: Metabolism of dox to dox'ol in Single Living Cells82

LIST OF ABBREVIATIONS

<u>Abbreviation</u>	<u>Meaning</u>
Dox	Doxorubicin
Dox'ol	Doxorubicinol
Gold	Au
HGF	Hematopoietic growth factors
ICP-MS	Inductively coupled plasma mass spectrometry
i.t.	Intrathecal
i.v.	Intravenous
NPs	Nanoparticles
PEG	Polyethylene glycol
s.c.	Subcutaneous
SEM	Scanning electron microscopy
Silver	Ag
Spectral Imaging	SI
TEM	Transmission electron microscopy

Chapter 1: Label-Free Nanoparticles Overview

1.1 Introduction

NPs are a wide-ranging class of materials having an overall size of less than 100 nanometers (Laurent et al., 2008). These materials have emerged as key players in modern medicine in recent years, with uses from contrast agents in medical imaging to gene carriers for specific cell distribution. Because NPs are not simple molecules; they are made of three layers, including: (a) the surface layer, which can be functionalized with various small molecules, metal ions, surfactants, and polymers; (b) the shell layer, which is chemically and physically distinct from the core; and (c) the core, which is the central section of the NP and commonly refers to the NP itself (Shin et al., 2016) (**Fig 1-1**). NPs have many properties that can distinguish them from bulk materials not only by their sizes, such as chemical reactivity, energy absorption, and biological mobility (Murthy, 2007). The ability to adjust essential qualities such as solubility, diffusivity, blood circulation half-life, drug release characteristics, and immunogenicity is unrivaled when using nanoscale materials. In the last two decades, many NP-based diagnostic and therapeutic agents have been developed for the treatment of cancer, diabetes, pain, asthma, allergies, infections, etc (Brannon-Peppas & Blanchette, 2004), (Kawasaki & Player, 2005). These nano-level pharmaceuticals can provide more effective and/or more convenient routes of administration, reduce therapeutic toxicity, extend product life cycle, and ultimately reduce medical care costs (Murthy, 2007). Recent biomedical science researches have resulted in the successful redesign of therapeutic medicines for disease therapy (Yetisgin et al., 2020). A promising technique of delivering a wide range of molecules to specific areas in the body is to combine therapeutic

medicines with NPs that have distinct physicochemical and biological properties and design their paths for appropriate targeting (Jahan et al., 2017). This targeting technique increases the concentration of the therapeutic agent in cells/tissues, allowing for the use of low doses, especially if the agent's therapeutic activity and toxic effects are incompatible.

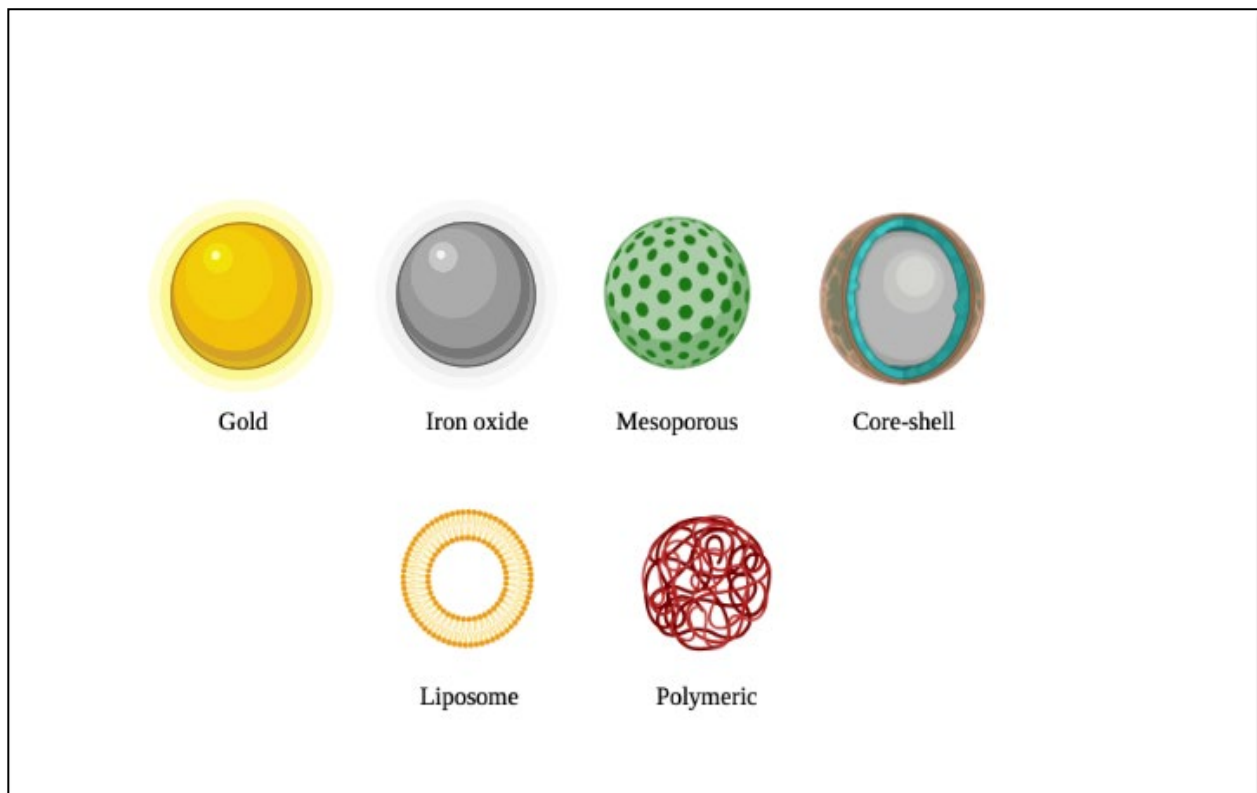


Figure 1-1: Different type of commonly used nanoparticles

1.2 Therapeutics based on NPs approved for clinical use

Many healthcare applications require direct detection and quantification of synthetic and naturally occurring NPs, such as determining viral load for infectious disease diagnostics (Cretich et al., 2015), assessing the quality of drug delivery reagents for therapy (De Jong & Borm, 2008), and discovering and evaluating new biomarkers such as exosomes for disease diagnosis and treatment monitoring (Srinivas et al., 2001). NP-based medicine delivery has several advantages that have been recognized. It enhances the solubility of poorly water-soluble medications, reduces immunogenicity and so prolongs the half-life of drugs in the systemic circulation, releases drugs at a steady rate or in an environmentally sensitive manner, and thus reduces the frequency of administration, administers medications in a targeted manner to reduce systemic side effects and simultaneously delivers two or more drugs for combination therapy to have a synergistic impact and inhibit drug resistance (Emerich & Thanos, 2007), (Kawasaki & Player, 2005). The number of commercially accessible NP-based medicinal products has been steadily increasing. More than 150 companies are developing nanoscale medicines, according to a global survey conducted by the European Science and Technology Observatory in 2006. There have been 24 nanotechnology-based medicinal medicines approved for clinical use thus far, with cumulative sales exceeding \$5.4 billion (Wagner et al., 2006). Liposomal medicines and polymer-drug conjugates are the two most common types of these products, accounting for more than 80% of the total (**Table 1-1**). Liposomes are spherical lipid vesicles with a bilayered membrane structure made of amphiphilic lipid molecules that can be natural or manufactured (L. Zhang & Granick, 2006), (Torchilin, 2005). Liposomes have become popular as pharmaceutical carriers in recent years due to their unique ability to (a) efficiently encapsulate both hydrophilic and hydrophobic medicinal ingredients, (b) protect the encapsulated medications from the undesired effects of the environment, (c) be

imbued with specific ligands that can be used to target specific cells, tissues, and organs (Torchilin, 2005), (Moghimi & Szebeni, 2003). Polymer–drug conjugates are another well-studied NP drug delivery method that is currently in clinical use (Duncan, 2006). Small-molecule therapeutic drugs, particularly anticancer chemotherapeutics, typically have two disadvantages: a short circulation half-life, which necessitates repeated administrations, and non-site-specific targeting, which results in unwanted systemic side effects. Small-molecule medications can be conjugated to polymeric nanocarriers to reduce unwanted side effects.

Table 1-1: NP-based medicines that have been approved clinically

Composition	Indication	Administration
<i>Liposomal platforms</i>		
Liposomal amphotericin B	Fungal infections	i.v.
Liposomal cytarabine	Malignant lymphomatous meningitis	i.t.
Liposomal dox	Combination therapy with cyclophosphamide in metastatic breast cancer	i.v.
Liposomal morphine	Postsurgical analgesia	Epidural
<i>Polymeric platforms</i>		
Methoxy-PEG-poly(D,L-lactide) taxol	Metastatic breast cancer	i.v.
L-Glutamic acid, L-alanine, L-lysine, and L-tyrosine copolymer	Multiple sclerosis	s.c.
PEG–HGF	Acromegaly	s.c.

1.3 Metallic NPs and their application

Metallic NPs feature an inorganic metal or metal oxide core usually surrounded by an organic or inorganic substance or metal oxide shell. Metal NPs have piqued the curiosity of scientists for decades due to their enormous potential in nanotechnology. Because metal NPs may be synthesized in a variety of sizes, shapes, and surface modifications, they can be coupled with antibodies, targeting ligands, and medicines, allowing for a wide range of applications. Metal NPs are used in a variety of ways in our daily lives (**Table 1-2**) (Khan, 2020). The introduction of pilot-scale production of metallic NPs, which have acquired the market in numerous consumer products such as lotions, shampoos, apparel, footwear, and plastic containers, has resulted from the development of new economically effective processes for metallic NPs manufacture (Diegoli et al., 2008).

Table 1-2: Metallic NPs applications

Metals	NPs application
Gold (Au)	Photodynamic treatment, cellular imaging
Silver (Ag)	Antimicrobial, batteries, electrical, photography
Zinc (Zn)	Sunscreen, skin protection
Copper (Cu)	Antimicrobial (i.e., antiviral, antibacterial), antibiotic treatment, lubricants, inks
Aluminum (Al)	Coating additive, fuel additive, explosive

(Schrand et al., 2010)

The gold NP is one of the first metals to be found, with a study and use history that dates back at least a thousand years. The first reports on colloidal gold can be detected in treatises by Chinese, Arabian, and Indian scientists; they used it for a wide range of purposes, including medicine (Chinese "golden solution" and Indian "liquid gold") (Dykman & Khlebtsov, 2011). Over the last half-century, reliable and high-yielding procedures for synthesizing AuNPs, including those with spherical and nonspherical forms, have been established. The resulting AuNPs have unique characteristics such as electronic and optical properties related to size and shape, a high surface-to-volume ratio, and surfaces that can be easily modified with functional groups such as thiols, phosphines, and amines, which show an affinity for gold surfaces (Daniel & Astruc, 2004). The development of gold nanoconjugates has enabled a wide range of investigations, including the controlled assembly and crystallization of materials (Mirkin et al., 1996), (S. Y. Park et al., 2008), on DNA templates, NPs can be arranged into dimers and trimers (Alivisatos et al., 1996), detection methods (J. Liu & Lu, 2003), biosensors (Kreibig & Vollmer, 2013), hyperthermia therapy (X. Huang et al., 2006), Therapeutic drug and genetic materials delivery systems (Paciotti et al., 2004), and anti-bacterial drugs (Sondi & Salopek-Sondi, 2004a), (Hsiao et al., 2006). Gold nanoconjugates and their characteristics have led to innovative and interesting advancements in biology and medicine in recent years. These studies exemplify a different direction that greatly differs from the more traditional use of gold nanoconjugates as labels for electron microscopy (Faulk & Taylor, 1971). Silver NPs (Ag NPs) are silver particles with a particle size of 1 to 100 nm. Similar to gold NPs, ionic silver has a long history and was originally utilized to dye the glass for yellow. At present, there are also efforts to include silver NPs into a broad range of medical devices, involving bone cement, surgical instruments, and surgical masks, etc. Furthermore, it has been demonstrated that ionic silver can be used to cure wounds in the correct amounts (Qin, 2005),

(Atiyeh et al., 2007), (Lansdown, 2006). Ag's antibacterial effect is well-known, and it's employed in a variety of medical preparation against pathogens (Sondi & Salopek-Sondi, 2004b), (Kumar & Yadav, 2009), (Sotiriou & Pratsinis, 2011). AgNPs have been shown to have antifungal properties (Vivek et al., 2011), and their use as antifungal agents has been found to be safer than traditional fungicides (Y. Park et al., 2011). Recent antimicrobial investigations of Ag NPs have revealed that bio-sorption and cellular absorption can cause significant membrane damage and DNA toxicity (Brayner et al., 2006), (Simon-Deckers et al., 2009). AgNPs are already used as antimicrobial agents in many widely accessible medicinal and consumer goods. Despite its decades of use, the evidence of its toxicity has yet to be adequately investigated. Many commercial products, such as computer keyboards, acne creams, and apparel (e.g., socks and athletic wear) that protect the wearer from generating body odor in addition to deodorizing sprays, now contain silver (D. Zhang et al., 2020).

1.4 Approaches to detect label-free NPs

Nanomaterial detection is challenging not only because of the particles' small size and potential for sequestration and agglomeration but also because of their distinct physical and chemical properties (Picó & Andreu, 2014). NP detection and identification methods are varied. The maturity of the nanoobject and the matrix in which it is contained, as well as the investigation's goals, determine which technique is used (Burlison et al., 2004). NPs with radioactive (Nemmar et al., 2002), magnetic (J. S. Kim et al., 2006), or fluorescent (Kwon et al., 2009) qualities make it easier to detect them in cells and tissues. However, the majority of inorganic nanosized particles lack these characteristics. The absence of universal methods or integrated protocols of analysis with the use of different methods is the key difficulty of NP control in bio-samples. Inexpensive

instruments are deficient for operational measurements, mass concentration control, surface area control, and size distribution control (Gendrikson et al., 2011).

Microscopy and other related techniques

Electron and scanning probe microscopy are the most common techniques of NPs visualization, with resolution up to the subnanometer scale. This approach uses beams of electrons focused on the surface of the sample through various electromagnetic lenses. Electrons are scattered through the sample and then refocused and magnified by another series of electromagnetic lenses in the image column to generate a projected image (Mayhew et al., 2009), (Robson et al., 2018a). There are several different types of the electron microscope, Scanning electron microscopy (SEM) and transmission electron microscopy (TEM). In the TEM ~~method~~, the focused electron beam passes through the sample, which should have a very small thickness, for example, the ultra-thin section obtained on the ultra-thin microtome or the dry suspension thin film. In the case of SEM, scattering of electrons occurs at the surface of the sample, and then an image is formed when the scattered electrons are focused (García-Negrete et al., 2015), (Robson et al., 2018a). Tissue samples are typically fixed with chemicals (most commonly formalin), then dehydrated with serial alcohol before embedment in embedding resin. Although this technique is typically considered semi-quantitative, there are several drawbacks to consider when using it to assess NP biodistribution. When compared to standard histology, electron microscopy is more expensive and incapable of evaluating large tissue sections. Moreover, to assess and approximate biodistribution in each organ, a small number of ultra-thin tissue sections (50–150 nm thickness) are commonly chosen, which may alter the results because not all sections are studied. Electron microscopy is also a time-consuming method, typically taking more than 3 to 4 hours to analyze a single sample (Kempen

et al., 2013). Since this method includes using lipid-soluble solvents, NPs composed of materials that are easily dissolved by these solvents (for example, liposomes, solid lipid NPs, and micelles) must use other biodistribution technologies.

Chromatographic methods

NPs can be isolated from complex samples using chromatographic techniques. They may have a high sensitivity depending on the detector used. By using detection methods, such as inductively coupled plasma mass spectrometry (IC-PMS), various NPs can be quantitatively determined in the composition of biological samples. In ICP, liquid samples are sprayed in a nebulizer to ionize elements by exciting the electrons of individual atoms through the thermal source of high temperatures (such as argon plasma). An ion guide separates the ionized atoms from neutral particles in a vacuum chamber, where they are measured by a mass spectrometer (MS). To separate the elements, the mass-to-charge ratio of the ions is applied, and the concentration of each element is calculated utilizing the ion signal percentage relative to an internal calibration standard (Wilschefski & Baxter, 2019). There are many disadvantages and challenges of ICP-MS. Sample destruction and digestion are required because ICP-MS samples must be in liquid form to permit ionization. In addition, equipment and operating (argon) cost. ICP-MS accuracy can be reduced by matrix effects, which can change analyte sensitivity caused by a high concentration of matrix components.

Spectroscopy and related methods

One of the most frequent techniques for assessing biodistribution after *in vivo* administration in animals is microscopic imaging of NPs in tissue sections. Under a microscope, typically light and

fluorescence microscopy, this technique examines the association of NPs with the cellular microenvironment. Most NPs, on the other hand, lack intrinsic fluorescence. Labeling NPs with fluorophores is a popular way of observing the dynamic events of these NPs within cells (Meinardi et al., 2015). The issue is that fluorophores are photobleached and might induce cell damage, limiting imaging to extremely short periods of time (Ji et al., 2008). As a result, the fluorescence signal may be reduced. Labeling NPs with fluorescent dyes may change their physicochemical properties and subsequent in vivo behavior in fluorescence imaging (Robson et al., 2018b). Several label-free methods have been developed for observing NPs in live cells, such as scatter-enhanced phase-contrast microscopy (Zimmerman et al., 2016a), Raman scattering microscopy (B. Huang et al., 2018a), and optical diffraction tomography (D. Kim et al., 2018a). However, for real-time imaging of label-free NPs, no strategies have been used except one approach, which is scattered light imaging, requiring a specific wavelength range. (F. Wang et al., 2019)

References

- Alivisatos, A. P., Johnsson, K. P., Peng, X., Wilson, T. E., Loweth, C. J., Bruchez, M. P., & Schultz, P. G. (1996). Organization of “nanocrystal molecules” using DNA. *Nature*, 382(6592), 609–611. <https://doi.org/10.1038/382609a0>
- Atiyeh, B. S., Costagliola, M., Hayek, S. N., & Dibo, S. A. (2007). Effect of silver on burn wound infection control and healing: Review of the literature. *Burns: Journal of the International Society for Burn Injuries*, 33(2), 139–148. <https://doi.org/10.1016/j.burns.2006.06.010>
- Brannon-Peppas, L., & Blanchette, J. O. (2004). Nanoparticle and targeted systems for cancer therapy. *Advanced Drug Delivery Reviews*, 56(11), 1649–1659. <https://doi.org/10.1016/j.addr.2004.02.014>
- Brayner, R., Ferrari-Iliou, R., Brivois, N., Djediat, S., Benedetti, M. F., & Fiévet, F. (2006). Toxicological impact studies based on Escherichia coli bacteria in ultrafine ZnO nanoparticles colloidal medium. *Nano Letters*, 6(4), 866–870. <https://doi.org/10.1021/nl052326h>
- Burleson, D. J., Driessen, M. D., & Penn, R. L. (2004). On the characterization of environmental nanoparticles. *Journal of Environmental Science and Health. Part A, Toxic/Hazardous Substances & Environmental Engineering*, 39(10), 2707–2753. <https://doi.org/10.1081/ese-200027029>
- Cretich, M., Daaboul, G. G., Sola, L., Ünlü, M. S., & Chiari, M. (2015). Digital detection of biomarkers assisted by nanoparticles: Application to diagnostics. *Trends in Biotechnology*, 33(6), 343–351. <https://doi.org/10.1016/j.tibtech.2015.03.002>

- Daniel, M.-C., & Astruc, D. (2004). Gold nanoparticles: Assembly, supramolecular chemistry, quantum-size-related properties, and applications toward biology, catalysis, and nanotechnology. *Chemical Reviews*, *104*(1), 293–346. <https://doi.org/10.1021/cr030698+>
- De Jong, W. H., & Borm, P. J. A. (2008). Drug delivery and nanoparticles: applications and hazards. *International Journal of Nanomedicine*, *3*(2), 133–149. <https://doi.org/10.2147/ijn.s596>
- Diegoli, S., Manciuola, A. L., Begum, S., Jones, I. P., Lead, J. R., & Preece, J. A. (2008). Interaction between manufactured gold nanoparticles and naturally occurring organic macromolecules. *The Science of the Total Environment*, *402*(1), 51–61. <https://doi.org/10.1016/j.scitotenv.2008.04.023>
- Duncan, R. (2006). Polymer conjugates as anticancer nanomedicines. *Nature Reviews. Cancer*, *6*(9), 688–701. <https://doi.org/10.1038/nrc1958>
- Dykman, L. A., & Khlebtsov, N. G. (2011). Gold nanoparticles in biology and medicine: Recent advances and prospects. *Acta Naturae*, *3*(2), 34–55.
- Faulk, W. P., & Taylor, G. M. (1971). An immunocolloid method for the electron microscope. *Immunochemistry*, *8*(11), 1081–1083. [https://doi.org/10.1016/0019-2791\(71\)90496-4](https://doi.org/10.1016/0019-2791(71)90496-4)
- García-Negrete, C. A., Jiménez de Haro, M. C., Blasco, J., Soto, M., & Fernández, A. (2015). STEM-in-SEM high resolution imaging of gold nanoparticles and bivalve tissues in bioaccumulation experiments. *The Analyst*, *140*(9), 3082–3089. <https://doi.org/10.1039/c4an01643b>
- Gendrikson, O. D., Safenkova, I. V., Zherdev, A. V., Dzantiev, B. B., & Popov, V. O. (2011). [Methods of detection and identification of manufactured nanoparticles]. *Biofizika*, *56*(6), 965–994.

- Hsiao, M.-T., Chen, S.-F., Shieh, D.-B., & Yeh, C.-S. (2006). One-pot synthesis of hollow Au₃Cu₁ spherical-like and biomineral botallackite Cu₂(OH)₃Cl flowerlike architectures exhibiting antimicrobial activity. *The Journal of Physical Chemistry. B*, *110*(1), 205–210. <https://doi.org/10.1021/jp054827x>
- Huang, B., Yan, S., Xiao, L., Ji, R., Yang, L., Miao, A.-J., & Wang, P. (2018a). Label-Free Imaging of Nanoparticle Uptake Competition in Single Cells by Hyperspectral Stimulated Raman Scattering. *Small (Weinheim an Der Bergstrasse, Germany)*, *14*(10). <https://doi.org/10.1002/sml.201703246>
- Huang, X., Jain, P. K., El-Sayed, I. H., & El-Sayed, M. A. (2006). Determination of the minimum temperature required for selective photothermal destruction of cancer cells with the use of immunotargeted gold nanoparticles. *Photochemistry and Photobiology*, *82*(2), 412–417. <https://doi.org/10.1562/2005-12-14-RA-754>
- Jahan, S. T., Sadat, S. M. A., Walliser, M., & Haddadi, A. (2017). Targeted Therapeutic Nanoparticles: An Immense Promise to Fight against Cancer. *Journal of Drug Delivery*, *2017*, 9090325. <https://doi.org/10.1155/2017/9090325>
- Ji, N., Magee, J. C., & Betzig, E. (2008). High-speed, low-photodamage nonlinear imaging using passive pulse splitters. *Nature Methods*, *5*(2), 197–202. <https://doi.org/10.1038/nmeth.1175>
- Kawasaki, E. S., & Player, A. (2005). Nanotechnology, nanomedicine, and the development of new, effective therapies for cancer. *Nanomedicine: Nanotechnology, Biology, and Medicine*, *1*(2), 101–109. <https://doi.org/10.1016/j.nano.2005.03.002>
- Kempen, P. J., Thakor, A. S., Zavaleta, C., Gambhir, S. S., & Sinclair, R. (2013). A scanning transmission electron microscopy approach to analyzing large volumes of tissue to detect

- nanoparticles. *Microscopy and Microanalysis: The Official Journal of Microscopy Society of America, Microbeam Analysis Society, Microscopical Society of Canada*, 19(5), 1290–1297. <https://doi.org/10.1017/S143192761300192X>
- Khan, S. A. (2020). Chapter 1 - Metal nanoparticles toxicity: Role of physicochemical aspects. In M. R. Shah, M. Imran, & S. Ullah (Eds.), *Metal Nanoparticles for Drug Delivery and Diagnostic Applications* (pp. 1–11). Elsevier. <https://doi.org/10.1016/B978-0-12-816960-5.00001-X>
- Kim, D., Oh, N., Kim, K., Lee, S., Pack, C.-G., Park, J.-H., & Park, Y. (2018a). Label-free high-resolution 3-D imaging of gold nanoparticles inside live cells using optical diffraction tomography. *Methods (San Diego, Calif.)*, 136, 160–167. <https://doi.org/10.1016/j.ymeth.2017.07.008>
- Kim, J. S., Yoon, T.-J., Yu, K. N., Kim, B. G., Park, S. J., Kim, H. W., Lee, K. H., Park, S. B., Lee, J.-K., & Cho, M. H. (2006). Toxicity and tissue distribution of magnetic nanoparticles in mice. *Toxicological Sciences: An Official Journal of the Society of Toxicology*, 89(1), 338–347. <https://doi.org/10.1093/toxsci/kfj027>
- Kreibig, U., & Vollmer, M. (2013). *Optical Properties of Metal Clusters*. Springer Science & Business Media.
- Kumar, V., & Yadav, S. K. (2009). Plant-mediated synthesis of silver and gold nanoparticles and their applications. *Journal of Chemical Technology & Biotechnology*, 84(2), 151–157. <https://doi.org/10.1002/jctb.2023>
- Kwon, J.-T., Kim, D.-S., Minai-Tehrani, A., Hwang, S.-K., Chang, S.-H., Lee, E.-S., Xu, C.-X., Lim, H. T., Kim, J.-E., Yoon, B.-I., An, G.-H., Lee, K.-H., Lee, J.-K., & Cho, M.-H. (2009). Inhaled fluorescent magnetic nanoparticles induced extramedullary hematopoiesis in the

- spleen of mice. *Journal of Occupational Health*, 51(5), 423–431.
<https://doi.org/10.1539/joh.18159>
- Lansdown, A. B. G. (2006). Silver in health care: Antimicrobial effects and safety in use. *Current Problems in Dermatology*, 33, 17–34. <https://doi.org/10.1159/000093928>
- Laurent, S., Forge, D., Port, M., Roch, A., Robic, C., Vander Elst, L., & Muller, R. N. (2008). Magnetic iron oxide nanoparticles: Synthesis, stabilization, vectorization, physicochemical characterizations, and biological applications. *Chemical Reviews*, 108(6), 2064–2110.
<https://doi.org/10.1021/cr068445e>
- Liu, J., & Lu, Y. (2003). A colorimetric lead biosensor using DNAzyme-directed assembly of gold nanoparticles. *Journal of the American Chemical Society*, 125(22), 6642–6643.
<https://doi.org/10.1021/ja034775u>
- Mayhew, T. M., Mühlfeld, C., Vanhecke, D., & Ochs, M. (2009). A review of recent methods for efficiently quantifying immunogold and other nanoparticles using TEM sections through cells, tissues and organs. *Annals of Anatomy = Anatomischer Anzeiger: Official Organ of the Anatomische Gesellschaft*, 191(2), 153–170.
<https://doi.org/10.1016/j.aanat.2008.11.001>
- Meinardi, F., McDaniel, H., Carulli, F., Colombo, A., Velizhanin, K. A., Makarov, N. S., Simonutti, R., Klimov, V. I., & Brovelli, S. (2015). Highly efficient large-area colourless luminescent solar concentrators using heavy-metal-free colloidal quantum dots. *Nature Nanotechnology*, 10(10), 878–885. <https://doi.org/10.1038/nnano.2015.178>
- Mirkin, C. A., Letsinger, R. L., Mucic, R. C., & Storhoff, J. J. (1996). A DNA-based method for rationally assembling nanoparticles into macroscopic materials. *Nature*, 382(6592), 607–609. <https://doi.org/10.1038/382607a0>

- Moghimi, S. M., & Szebeni, J. (2003). Stealth liposomes and long circulating nanoparticles: Critical issues in pharmacokinetics, opsonization and protein-binding properties. *Progress in Lipid Research*, 42(6), 463–478. [https://doi.org/10.1016/s0163-7827\(03\)00033-x](https://doi.org/10.1016/s0163-7827(03)00033-x)
- Murthy, S. K. (2007). Nanoparticles in modern medicine: State of the art and future challenges. *International Journal of Nanomedicine*, 2(2), 129–141.
- Nemmar, A., Hoet, P. H. M., Vanquickenborne, B., Dinsdale, D., Thomeer, M., Hoylaerts, M. F., Vanbilloen, H., Mortelmans, L., & Nemery, B. (2002). Passage of inhaled particles into the blood circulation in humans. *Circulation*, 105(4), 411–414. <https://doi.org/10.1161/hc0402.104118>
- Paciotti, G. F., Myer, L., Weinreich, D., Goia, D., Pavel, N., McLaughlin, R. E., & Tamarkin, L. (2004). Colloidal gold: A novel nanoparticle vector for tumor directed drug delivery. *Drug Delivery*, 11(3), 169–183. <https://doi.org/10.1080/10717540490433895>
- Park, S. Y., Lytton-Jean, A. K. R., Lee, B., Weigand, S., Schatz, G. C., & Mirkin, C. A. (2008). DNA-programmable nanoparticle crystallization. *Nature*, 451(7178), 553–556. <https://doi.org/10.1038/nature06508>
- Park, Y., Hong, Y. N., Weyers, A., Kim, Y. S., & Linhardt, R. J. (2011). Polysaccharides and phytochemicals: A natural reservoir for the green synthesis of gold and silver nanoparticles. *IET Nanobiotechnology*, 5(3), 69–78. <https://doi.org/10.1049/iet-nbt.2010.0033>
- Picó, Y., & Andreu, V. (2014). 12—Nanosensors and other techniques for detecting nanoparticles in the environment. In K. C. Honeychurch (Ed.), *Nanosensors for Chemical and Biological Applications* (pp. 295–338). Woodhead Publishing. <https://doi.org/10.1533/9780857096722.2.295>

- Qin, Y. (2005). Silver-containing alginate fibres and dressings. *International Wound Journal*, 2(2), 172–176. <https://doi.org/10.1111/j.1742-4801.2005.00101.x>
- Robson, A.-L., Dastoor, P. C., Flynn, J., Palmer, W., Martin, A., Smith, D. W., Woldu, A., & Hua, S. (2018a). Advantages and Limitations of Current Imaging Techniques for Characterizing Liposome Morphology. *Frontiers in Pharmacology*, 9, 80. <https://doi.org/10.3389/fphar.2018.00080>
- Robson, A.-L., Dastoor, P. C., Flynn, J., Palmer, W., Martin, A., Smith, D. W., Woldu, A., & Hua, S. (2018b). Advantages and Limitations of Current Imaging Techniques for Characterizing Liposome Morphology. *Frontiers in Pharmacology*, 9, 80. <https://doi.org/10.3389/fphar.2018.00080>
- Rubakhin, S. S., Romanova, E. V., Nemes, P., & Sweedler, J. V. (2011). Profiling metabolites and peptides in single cells. *Nature Methods*, 8(4 Suppl), S20-29. <https://doi.org/10.1038/nmeth.1549>
- Schrand, A. M., Rahman, M. F., Hussain, S. M., Schlager, J. J., Smith, D. A., & Syed, A. F. (2010). Metal-based nanoparticles and their toxicity assessment. *Wiley Interdisciplinary Reviews. Nanomedicine and Nanobiotechnology*, 2(5), 544–568. <https://doi.org/10.1002/wnan.103>
- Shin, W.-K., Cho, J., Kannan, A. G., Lee, Y.-S., & Kim, D.-W. (2016). Cross-linked Composite Gel Polymer Electrolyte using Mesoporous Methacrylate-Functionalized SiO₂ Nanoparticles for Lithium-Ion Polymer Batteries. *Scientific Reports*, 6, 26332. <https://doi.org/10.1038/srep26332>
- Simon-Deckers, A., Loo, S., Mayne-L'hermite, M., Herlin-Boime, N., Menguy, N., Reynaud, C., Gouget, B., & Carrière, M. (2009). Size-, composition- and shape-dependent toxicological

- impact of metal oxide nanoparticles and carbon nanotubes toward bacteria. *Environmental Science & Technology*, 43(21), 8423–8429. <https://doi.org/10.1021/es9016975>
- Sondi, I., & Salopek-Sondi, B. (2004a). Silver nanoparticles as antimicrobial agent: A case study on *E. coli* as a model for Gram-negative bacteria. *Journal of Colloid and Interface Science*, 275(1), 177–182. <https://doi.org/10.1016/j.jcis.2004.02.012>
- Sondi, I., & Salopek-Sondi, B. (2004b). Silver nanoparticles as antimicrobial agent: A case study on *E. coli* as a model for Gram-negative bacteria. *Journal of Colloid and Interface Science*, 275(1), 177–182. <https://doi.org/10.1016/j.jcis.2004.02.012>
- Sotiriou, G. A., & Pratsinis, S. E. (2011). Engineering nanosilver as an antibacterial, biosensor and bioimaging material. *Current Opinion in Chemical Engineering*, 1(1), 3–10. <https://doi.org/10.1016/j.coche.2011.07.001>
- Srinivas, P. R., Kramer, B. S., & Srivastava, S. (2001). Trends in biomarker research for cancer detection. *The Lancet. Oncology*, 2(11), 698–704. [https://doi.org/10.1016/S1470-2045\(01\)00560-5](https://doi.org/10.1016/S1470-2045(01)00560-5)
- Torchilin, V. P. (2005). Recent advances with liposomes as pharmaceutical carriers. *Nature Reviews. Drug Discovery*, 4(2), 145–160. <https://doi.org/10.1038/nrd1632>
- Vivek, M., Kumar, P. S., Steffi, S., & Sudha, S. (2011). Biogenic Silver Nanoparticles by *Gelidiella acerosa* Extract and their Antifungal Effects. *Avicenna Journal of Medical Biotechnology*, 3(3), 143–148.
- Wagner, V., Dullaart, A., Bock, A.-K., & Zweck, A. (2006). The emerging nanomedicine landscape. *Nature Biotechnology*, 24(10), 1211–1217. <https://doi.org/10.1038/nbt1006-1211>

- Wang, F., Chen, B., Yan, B., Yin, Y., Hu, L., Liang, Y., Song, M., & Jiang, G. (2019). Scattered Light Imaging Enables Real-Time Monitoring of Label-Free Nanoparticles and Fluorescent Biomolecules in Live Cells. *Journal of the American Chemical Society*, *141*(36), 14043–14047. <https://doi.org/10.1021/jacs.9b05894>
- Wilschefski, S. C., & Baxter, M. R. (2019). Inductively Coupled Plasma Mass Spectrometry: Introduction to Analytical Aspects. *The Clinical Biochemist. Reviews*, *40*(3), 115–133. <https://doi.org/10.33176/AACB-19-00024>
- Yetisgin, A. A., Cetinel, S., Zuvun, M., Kosar, A., & Kutlu, O. (2020). Therapeutic Nanoparticles and Their Targeted Delivery Applications. *Molecules (Basel, Switzerland)*, *25*(9), E2193. <https://doi.org/10.3390/molecules25092193>
- Zhang, D., Ma, X.-L., Gu, Y., Huang, H., & Zhang, G.-W. (2020). Green Synthesis of Metallic Nanoparticles and Their Potential Applications to Treat Cancer. *Frontiers in Chemistry*, *8*, 799. <https://doi.org/10.3389/fchem.2020.00799>
- Zhang, L., & Granick, S. (2006). How to stabilize phospholipid liposomes (using nanoparticles). *Nano Letters*, *6*(4), 694–698. <https://doi.org/10.1021/nl052455y>
- Zimmerman, J. F., Parameswaran, R., Murray, G., Wang, Y., Burke, M., & Tian, B. (2016a). Cellular uptake and dynamics of unlabeled freestanding silicon nanowires. *Science Advances*, *2*(12), e1601039. <https://doi.org/10.1126/sciadv.1601039>

Chapter 2: The Use of Advanced Spectral Imaging to Reveal Nanoparticle Identity in Biological Samples

Alshammari, Q. A., Pala, R., Barui, A. K., Alshammari, S. O., Nauli, A. M., Katzir, N., Mohieldin, A. M., & Nauli, S. M. (2022). The use of advanced spectral imaging to reveal nanoparticle identity in biological samples. *Nanoscale*, 14(11), 4065–4072.

<https://doi.org/10.1039/D1NR07551A>

Author Contribution:

QAA collected data, analyzed data and drafted the manuscript. RP synthesized and characterized the NPs and helped design some studies. RB, resynthesized the nanoparticles for characterization purposes. SOA contributed in the H&E and silver staining experiments (double-blind). AMN provided data and statistical analyses. NK participated in the spectral imaging system and software analysis. AMM analyzed the TEM images. SMN conceived the idea, designed research and oversaw the experimental progress. All authors were participating in finalizing the draft of the manuscript.

2.1 Abstract

Inorganic NPs have been used in drug delivery therapy, medical diagnostic strategy, and the current Covid-19 vaccine carriers. We recently introduced SI that could distinguish a drug molecule and its metabolite that are structurally different by only 1 hydrogen atom resulted from

the cellular metabolism (Alshammari et al., 2021). Using the same technique, we here show that we could detect unlabeled Ag-NPs and Au-NPs in single live cells and tissues (liver, heart, spleen and kidney). Our studies were validated using various laborious and time-consuming conventional techniques. Importantly, unlike other breakthrough studies that depend on the plasmon resonance scattering or extinction spectra “intensity”(Zimmerman et al., 2016b), (Chen et al., 2015), (Patskovsky et al., 2015), (Chen et al., 2010), (Ling et al., 2009), SI uses a broader 400-800 nm spectra “identity” to provide a more specific fingerprinting for each single molecule. This in turn allows us to detect surface-functionalization of Ag-NPs with shell (Ag(s)-NPs) from non-shelling core-only Ag-NPs. We propose that SI has a tremendous potential to study NP localization and identification in biological samples at a high temporal and spatial resolution, based primarily on the spectra identity information.

2.2 Introduction

The conventional methods used for the quantification of the inorganic NPs include inductively coupled plasma mass spectrometry (ICP-MS) and inductively-coupled plasma atomic emission spectroscopy (ICP-AES) (António et al., 2016), (Vanhecke et al., 2014), (Lee et al., 2014). In addition to the matrix interference, some disadvantages in ICP associated methods include chemical intervention, the necessity of liquid sample, plasma sensitivity to organic solvents, and ineffectiveness of the nebulizer. Non-destructive techniques have also been developed. These include the use of fluorescent-labeled NPs (Pala, Mohieldin, Sherpa, et al., 2019), (Pala, Mohieldin, Shamloo, et al., 2019) and the modern ultrasonic holography (Shekhawat & Dravid, 2005), (Tetard et al., 2008). While fluorescent-conjugated NPs are generally used to identify NP localization in the live biological samples, such conjugation could interfere with NP function, localization, cytotoxicity and biodistribution (Snipstad et al., 2017), (Tenuta et al., 2011a), (Corbo

et al., 2016). Thus, different imaging modalities have been recently introduced to image unlabeled-NPs without destroying the biological tissues. Based on the light-refractive index of NPs, NPs detections in live cells have been performed (D. Kim et al., 2018b). The specific scattered-light of NPs allows real-time monitoring of unlabeled NPs (F. Wang et al., 2019). In addition to Raman spectroscopy (B. Huang et al., 2018b), a standard optical spectroscopic microscopy has also been used to image NPs, albeit this was done at a much narrow scanning range of 200 nm (Spicer et al., 2018). Different optical microscopy techniques to detect a specific spectrum of NPs have therefore been proposed to capture absorption spectra (Zimmerman et al., 2016b) and the plasmon resonance scattering or extinction spectra of various NPs (Chen et al., 2015), (Patskovsky et al., 2015), (Chen et al., 2010), (Ling et al., 2009). Despite recent advances in optical microscopes, visualizing unlabeled-NPs remains a challenge. This is primarily due to the intensity-based measurements performed at a very narrow spectrum optimized for different studies and systems at different laboratories. We recently introduced a SI in which broader spectral characteristics are first identified, characterized and stored in a library (Alshammari et al., 2021). These spectra are scanned from 400-800 nm with an average resolution of 10 nm, resulting in unique 40 interconnected datapoints. The key feature is that we could recall all spectra with the similar characteristics from the library, based merely on the identity of these 40 datapoints, i.e., the relative intensity of these 40 points toward each other. This strategy allows us to differentiate 2 molecules which are different by only a single hydrogen atom (Alshammari et al., 2021).

2.3 Materials and Methods

Materials

LL-CPK1 (ATCC. CL101.1TM) porcine renal epithelial cells from proximal tubule were purchased from American Type Culture Collection (ATCC; Manassas, VA). Trypsin, penicillin-streptomycin solution (lot# 04619001), phosphate-buffered saline (PBS; lot# 05319001), and Dulbecco's Modified Eagle Medium (DMEM) (lot# 20818006) were purchased from Corning (Manassas, VA). Fetal bovine serum (FBS) was obtained from Seradigm (Logan, UT), paraformaldehyde (PFA) from Electron Microscopy Services (Hatfield, PA), Mounting Media HistoChoice. from Amresco, lysis buffer from Thermo scientific (Rockford, IL), protease inhibitor cocktail from Roche (Mannheim, Germany), Nitric Acid TraceMetal Grade (lot# 1119040) and Hydrochloric Acid TraceMetal Grade (lot# 4119080) from Fisher Scientific (Fair Lawn, NJ 07410), and Silver Staining Kit from Invitrogen (Cat no. LC6070).

Cell culture

LL CPK1 cells were cultured to a confluent monolayer in DMEM supplemented with 10% FBS and 1% penicillin-streptomycin at 37°C in 5% CO₂ and 95% humidity. Cells were trypsinized (using a 0.05% solution of trypsin) regularly for passage when 70-90% confluence was reached. For our experiments, cells were cultured to reach confluence before treatment with vehicle or different types of NPs.

Synthesis of Ag-NPs and Au-NPs

For the synthesis of Ag(s)-NPs, silver nitrate (AgNO₃) and for gold NPs (Au-NPs), chloroauric acid (HAuCl₄) were purchased from Millipore Sigma, USA and was used without further

purification. Ag and Au-NPs synthesis were carried out by taking 5 mL of betel leaf broth (*Piper betle* L.) and adding 90 mL of 1×10^{-3} M aqueous AgNO_3 and HAuCl_4 solutions individually at room temperature, followed by exposing the reaction mixtures to direct sunlight irradiation at Chapman University School of Pharmacy, CA, USA (latitude 33°N) in June 2019 from the time period between 11:00 a.m. and 2:00 p.m. under clear sky conditions with different time periods ranging from 5 min to 1 h. The Ag and Au-NPs colloidal solutions thus obtained were purified by repeated centrifugation (by using a Thermofisher ultra microcentrifuge) at 20,000 rpm for 10 min followed by redispersion of the pellets of Ag and Au- NPs into 20 mL of ultrapure water. To further purify the NPs, the centrifuging and redispersion process was repeated for five times. The bio-reduction of the Ag and Au ions in solutions were monitored by periodic sampling of aliquots of the reaction mixtures and measuring the UV–vis spectrum of the solutions individually. Silver NPs (no-shell) were also synthesized by chemical methods in order to compare with silver (core-shell NPs). Briefly, Ag NPs (no-shell) were prepared by reducing 180 mL of AgNO_3 (1×10^{-3} M) using 20 mL of NaBH_4 (0.04 mg/mL). The loose dark pellet was collected from chemically synthesizing Ag NPs through centrifugation at 20,000 rpm at 26°C for 20 min in a Thermo ultra-microcentrifuge. The chemically synthesized Ag NPs were further purified by the centrifuging and redispersion process was repeated for three times.

UV-VIS Spectrum Detection

Spectrophotometer (SpectraMax M5 Microplate Reader) was used to read the ultraviolet-visible (UV-VIS). The UV-VIS wavelength of Ag-NP and Au-NP clusters were read at concentrations of 0.025, 0.05, 0.125, 0.25, 0.375, 0.5 mg/mL diluted in deionized water, which was filtered through

Milli-Q (MilliporeSigma, Burlington, MA). The wavelength range of 200-800 nm was used to read the UV spectrum for all the chemicals.

Cell Treatment

Cells were seeded on sterilized 22x22 mm coverslip (Globe Scientific), in 6 wells plate (Greiner bio-one Cellstar®, the total volume of 2 mL at each well) under normal growth conditions until reached 70-80% confluency. The cells then incubated with 100 μ L of the selected chemical at different concentrations of NPs for 18 hrs. Then, the cells washed three times by PBS, fixed the cells for 10 min in fixing solution (2.5 mL PFA, 7.5 mL PBS and 0.2 g sucrose) at room temperature. Afterward, the coverslip was placed on the slide that contains 25 μ L of Mounting Media overnight at room temperature.

Spectral Imaging

Spectral imaging instrument (Applied Spectral Imaging's GenASIs™ Hyperspectral Imaging System) and Olympus microscope (Model BX61) were used in this research. Images were manually acquired with 60X magnification objective. Xenon arc lamp was used as our light source in transmission mode through the sample. Contrast was produced through the absorption of light in dense areas of the sample. Ag-NPs and Au-NPs cluster wavelengths were identified by utilizing the brightfield filter. Optical Density (OD) spectra were extracted and used to view and classify spectra.

Our system used a previously described standard microscopy set-up (Alshammari et al., 2021). This set-up was widely available in most laboratories. Hyperspectral system was based on a Sagnac interferometer. The beam splitter split the light originating from the selected area in the sample into two beams. A set of mirrors led the beams down two paths of various lengths. At the end of

the paths, the two beams are combined and superimposed on the sensor. The total intensity of these two superimposed beams at each point of the sensor is a function of the spectrum of this point on the sample and the difference in the distance between the two paths. This difference is called the Optical Path Difference (OPD). The intensity of the merged beams is captured by a Charged-Coupled Device (CCD) camera. Each measurement is called a frame, which is a gray level image measured by the CCD camera. To extract a hyperspectral image a set of frames are acquired, each corresponds to slightly different OPD. This process arose simultaneously for all pixels in the image. The vector of intensities at each pixel, collected from the set of images with shifted OPD's, is called an interferogram. The Hyperspectral image is derived by Fourier Transformation of the interferograms of all pixels.

For each NP type, we defined wavelengths, which represent areas that we selected within the image in order to compare their spectra and to build a spectral library after background subtraction. For instance, inside the chemical image, to compare the chemical substance spectrum with the background spectrum, we defined wavelengths in the area that contained NP clusters, and in the area that contains nothing (background). This background wavelength also represented an empty cover treated the same way but without the addition of NPs. We then displayed the two spectra (NPs and background). The NP spectra were obtained by subtracting the background spectra. After that, we saved these NP spectra in libraries for further cell analysis. At least 10 images were captured randomly from the cells that were treated with NPs. Afterward, we analyzed the captured images by using spectral libraries of the NPs and scanned all the areas to obtain the location that only matched with the NP libraries. For the Ag-NPs and Au-NPs samples, we used the brightfield SUN analysis (within the SpectraView software, Applied Spectral Imaging), which performs Spectral UNmixing, separating an image into layers that corresponded to the absorption spectra

(libraries). This led us to quantify the amount and pinpoint the location of material according to its absorption spectra.

Time-lapse imaging

LLCPK cells were grown on six wells plate and treated with 0.1 mg NPs in 2 mL media. Living cells were imaged using a SI system, every 20 minutes for 8 hrs.

Transmission Electron Microscopy

The cells were treated with Ag-NPs and Au-NPs and incubated for 18 hours. Afterward, the cells were washed three times for 5 minutes with PBS. Then, the cells were trypsinized and fixed for 60 min in primary fixation (2% paraformaldehyde and 2.5% glutaraldehyde in 1% PBS buffer) at room temperature, followed by three washing with PBS. The resulting samples were postfixed with 1% osmium tetroxide for 60 min, followed by three-time washing with buffer and three-time washing with water. Afterward, the cells were dehydrated in a series of alcohol, then embedded in epoxy resin. Ultrathin sections of 120 nm were then stained with uranyl acetate and lead citrate and observed by TEM. The slices were examined under a JEM-2100F transmission microscope (JEOL) and the images were recorded on Gatan Oneview CCD as an image montage with the aid of SerialEM software. For TEM image, the microscope was operated at 200kV, and the images were taken at a minimum magnification of 10,000.

Animal Studies

All animal procedures were performed according to Chapman University Animal Care and Use Committee Guidelines. A total of four groups of mice were injected intravenously with saline solution (vehicle control), Ag(s)-NPs, Ag-NPs or Au-NPs for a total treatment time of 24 hours.

The total NPs were injected at 1 mg/kg in 45-days old wild-type C57BL6 Black with averaged body weight of 27.5 ± 2.8 g. Both male and female mice were used and randomly selected for the treatments. Then, the mice were euthanized to collect liver, kidney, liver, heart, and spleen. Tissues were taken for SI or ICP-MS analyses.

Sample preparation prior to ICP-MS measurement

0.1 g of tissue (liver, kidney, heart, and spleen) weighed and added into 5 mL a mixture of concentrated nitric acid (HNO₃) and hydrochloric acid (HCl) (4:1) in digestion vessels. All the vessels were immediately shaken by hand and covered overnight for pre-dissolution. Afterward, the vessels were placed in oil and heated to about 100 °C for around 3 hours. The Au samples were diluted with 1% (v/v) HNO₃ and 1% (v/v) HCl; and the Ag and Ag (s) samples with 1% HNO₃.

Measurement with ICP-MS

All prepared standards and tissue samples were measured by the ICP-MS system (Thermo Scientific iCAP RQ ICP-MS). Quantification was carried out within elements (100-0.5 ppb) internal standard correction. The main operating conditions for ICP-MS were as follows: the radio frequency (RF) power 1550 W; argon gas flow rates for the plasma, auxiliary, and nebulizer flow were 14 L min⁻¹, 0.8 L min⁻¹, and 1.07 L min⁻¹, respectively.

Hematoxylin and eosin staining

The tissue processing of the organs was performed by STP 120 Spin Tissue Processor (Thermo Fisher Scientific, USA). The dehydration step was performed by immersing the organs in a series of alcohol, 70% for 30 minutes, 80% for 30 minutes, 95% for 45 minutes, and 100% for 45

minutes. The clearing step was performed for 1.5 hours by using xylene. The last step of processing was the infiltration by paraffin for 1.5 hours. The tissues were then sectioned for H&E staining and observed under SI (**Table 2**).

Table 2-1: H&E staining steps

Compound	Time
Xylene	17 min
100% Ethanol	2 min
90% Ethanol	1 min
75% Ethanol	1 min
Tap water	3 min
Hematoxylin	3 min
Tap water	30 sec 3x
Dip (fast) in acid alcohol (200ml of 70% alcohol + 500 µl of HCl)	
DI water	15 min
Eosin	2 min
Tap water	2 min 2x
90% Ethanol	1 min
100% Ethanol	1 min
Xylene	2 min
Mounting media & coverslip	

Silver Staining

The distribution and localization of Ag-NPs and Au-NPs in the cell nucleus were validated with a silver staining Kit following manufacturer's protocol (Invitrogen Co., Thermo Fisher Scientific, Cat. LC6070). Briefly, after sample fixation, 30 % of ethanol was added to the samples for 10 minutes. The sensitizing solution was added, followed by 30 % ethanol, 10 minutes each. The samples were washed with ultrapure water and incubated in a staining solution for 15 minutes. The samples were washed again with ultrapure water for 20-60 seconds and incubated in the developing solution for 4-8 minutes. Lastly, stopper solution was added and gently agitated for 10 minutes, followed by washing with ultrapure water for 10 minutes. The resultant deposits of metallic silver around NPs were visualized using the SI system.

Statistics

Most of our statistical analysis was conducted by using SI software GenASI™ SpectraView version 7.2.7.34276 and GraphPad Prism software version 8.4.2. Microsoft Excel software version 16.37 was also used for linear regression analyses to obtain a standard calibration curve and linear equation. We used Student t-test to compare 2 groups and ANOVA followed by Tukey's posthoc test to compare 3 or more groups. A minimum of 3 independent studies was performed, and a more accurate repeat (N) was indicated in each figure by the dot plots and/or figure legend. Whenever possible, our studies were conducted in pairs by including control groups in each experimental group. The correlation analyses were performed by using Pearson correlation coefficient test. All data were reported as mean \pm standard error of mean (SEM). While $P < 0.05$ was considered significant, the level of significance was indicated accurately in each graph and figure legend.

2.4. Results

We report here that SI can provide a high temporal and spatial resolution of silver NPs with shell (Ag(s)-NPs) or without shell (Ag-NPs), and gold NPs (Au-NPs).

Spectra signatures of Ag(s)-NPs and Ag-NPs were identified with a major peak at 420 nm.

Using a microscope equipped with hyperspectral imaging (GenASIs from Applied Spectral Imaging), we imaged and recorded the spectral characteristics of the clusters of Ag(s)-NPs before and after incubated with the cells (**Fig. 2-1a**). We captured the spectral range between 400-800 nm for Ag(s) NPs in the present and absent of cells. Ag(s)-NPs had characteristics spectra with a distinctive peak at 420 nm (**Fig. 2-1b**). This peak was consistent with previous study (Fayaz et al., 2010). While this peak was the main characteristic of Ag(s)-NPs, we also looked at different features that could contribute to the characteristic of Ag(s)-NPs. Interestingly, we could generate two distinct libraries for Ag(s)-NPs. The peak of Ag(s)-NPs could be distinctively differentiated by the additional “shoulder” that only appeared at the peripheral or shell of the NPs. Of note, silver-polymer coreshell NPs are generally known for their unique optical properties, in which the shell of Ag also plays a critical role in protecting the Ag core (Claes et al., 2018), (Ertem et al., 2017). The shift in the shoulder peak could therefore be used to differentiate the core and shell of Ag-NPs clusters. We quantified the spectral intensities of these peaks before and after 18-hour incubation with cells (**Fig. 2-1c**). As verified with traditional spectrophotometry, the linearity of Ag(s)-NPs was observed at the peak of 420 nm (**Supp Fig. 1a**), indicating that we could predict the singularity or number of NPs in each pixel of an image based on the peak intensity of the spectra.

Extrapolating from these intensity differences, our data suggested that Ag(s)-NPs tended to aggregate more in solution than in the cells (**Fig. 2-1d**).

To confirm our observation of Ag(s)-NPs, we synthesized the Ag-NPs exclusively without the shell. The spectral characteristics of the Ag-NPs before and after incubation with the cells were recorded (**Fig. 2-2a**). Ag-NPs have the same characteristics spectra of Ag(s)-NPs, at ~420 nm, except that Ag-NPs spectra revealed without the additional “shoulder” (**Fig. 2-2b**). We also calculated the spectral intensities of these peaks before and after 18-hour incubation with cells (**Fig. 2-2c**). This disclosed the specificity of SI to differentiate between the spectral characteristics of different types of silver NPs (Ag-NPs and Ag(s)-NPs).

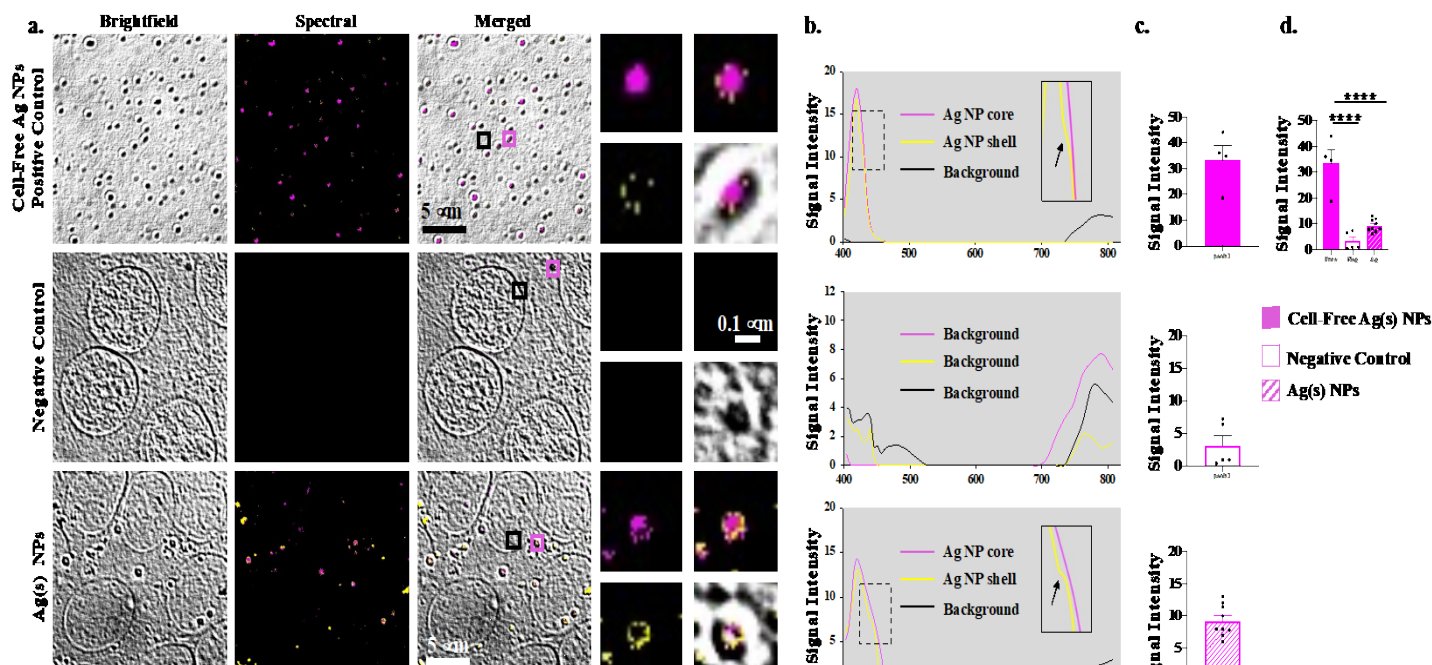


Figure 2-1: Identification of Ag(s)-NPs Spectra

(a) Brightfield images of the Ag(s)-NPs in the cell-free system (positive control), fixed cells (negative control), and 16-hour Ag(s)-NPs-treated cells (Ag(s)-NPs) were captured. The spectral images were extracted from the spectra library for the Ag(s)-NPs. Merged images illustrate superimposed brightfield and spectral images. The pink spectral image exhibits the core area of the Ag(s)-NPs cluster, while the yellow color represents the shell region. (b) The graphs illustrate the wavelength peaks at ~ 420 nm for the positive control and the incubated cells. The pink wavelength displays the intensity of the core area; the yellow wavelength shows the shell part (with a small shoulder; insert and arrow). The black color exhibits the spectrum of the background area. The negative control spectra were identified based on unmatched spectra from our libraries. (c) The bar graphs show the variation of intensity data points at 420 nm. (d) The signal intensities were compared among cell-free positive control, non-treated cells negative control, and Ag(s)-NPs-treated cells. $N=4-5$ for each positive and negative controls; $N=8$ for experimental groups. ****, $P<0.0001$.

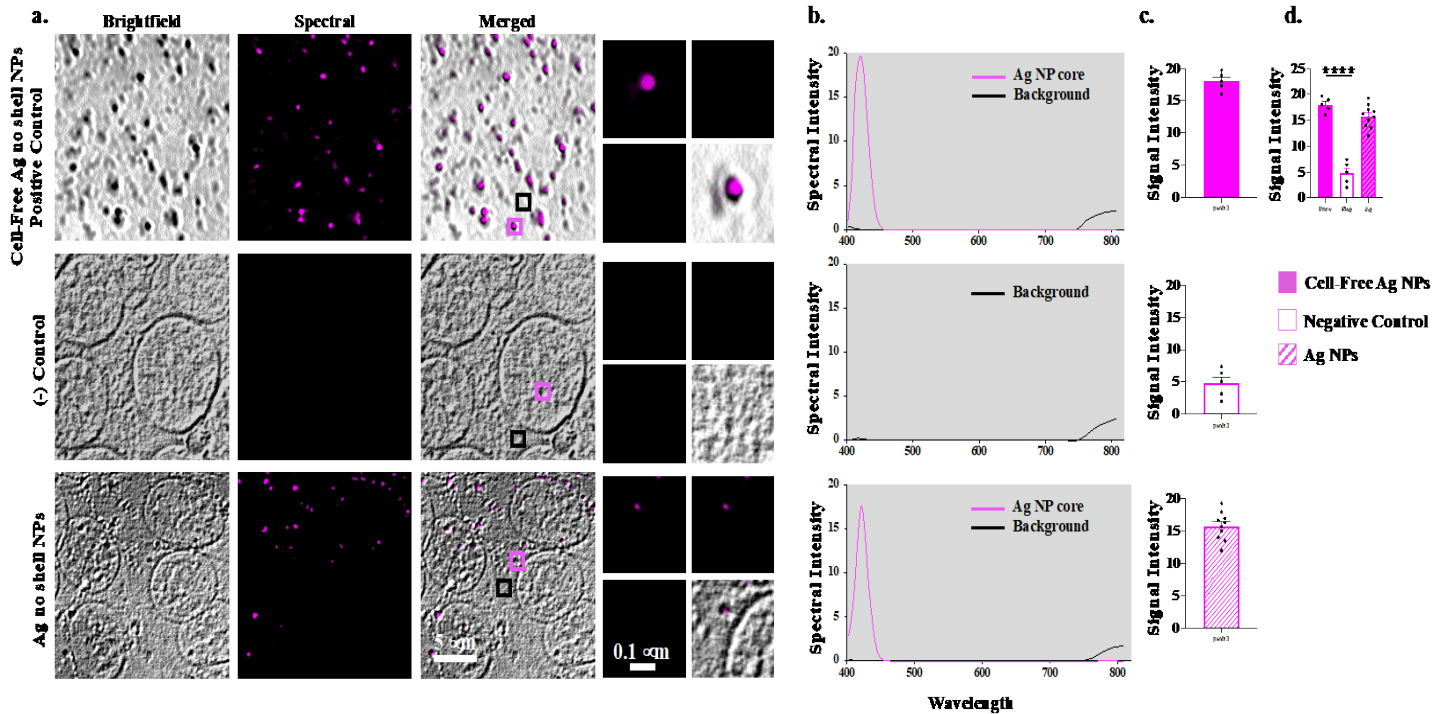


Figure 2-2: Identification of Ag-NPs Spectra

(a) Brightfield images are shown for Ag-NPs in the cell-free system (positive control), fixed cells (negative control), and 16-hour Ag-NPs-treated cells. The pseudo-colored spectral images were extracted from the spectra library for the Ag-NPs. Merged images exemplify superimposed brightfield and spectral images. The pink spectral image exhibits the core area of the Ag-NPs. (b) The graphs demonstrate the wavelength peaks of Ag-NPs clusters at ~420 nm for the positive control and the incubated cells. The pink wavelength presents the intensity of the core area. The black color displays the spectrum of the background area. The negative control spectra were identified based on unmatched spectra from our libraries. (c) The bar graphs show the variation of intensity data points at 420 nm. (d) The signal intensities were compared among cell-free positive control, non-treated cells negative control, and Ag-NPs-treated cells. N=4-5 for each positive and negative controls; N=8 for experimental groups. ****, $P < 0.0001$.

Spectra signature of Au-NPs was identified with a major peak at 552 nm.

Another inorganic NPs was prepared to further confirm the capabilities of SI to identify a different NP, Au-NPs (**Fig. 2-3a**). Capturing spectra between 400-800 nm revealed that the Au-NPs had a unique spectra peak ranged between 520 and 580 nm (**Fig. 2-3b**), consistent with previous study (Haiss et al., 2007). Background spectra without or with cells were captured to differentiate spectral intensity at 552 nm peak (**Fig. 2-3c**). The specific subcellular localization of Au-NPs in the cells could be determined by examining the spectral characteristics of each pixel in the image. In the fixed cells, after treated with Au-NPs for 18 hours, we could detect individuals or clusters of Au-NPs. To independently verify the microscopy spectra, we examined the Au-NPs spectra using traditional spectrophotometry (**Supp Fig. 1b**). The linearity of Au-NPs was observed at the peak of 536 nm, indicating that we could predict the singularity or number of NPs in each pixel of an image based on the peak intensity of the spectra. Extrapolating from these data, our studies suggested that Au-NPs tended to disperse more readily in the cells than in solution (**Fig. 2-3d**).

Spectral imaging showed dynamics Ag(s)-NP or Au-NP accumulation in the cell nucleus.

Once the spectral signatures for both Ag(s)-NPs and Au-NPs were identified and defined in the libraries, analytical software was used to perform spectral identity for each pixel of an image in order to identify pixels with spectral resemblance of Ag(s)-NPs or Au-NPs. Background spectral could be taken from the non-treated cells (negative control) or different areas within the field of view in the image (**See Method**). This was a powerful method to trace non-fluorescence inorganic substances. We thus applied this technique on the time-lapse imaging of cells treated with 0.1 mg Ag(s)-NPs in 2 mL cell media (**Fig. 2-4a; Supp Fig. 2**).

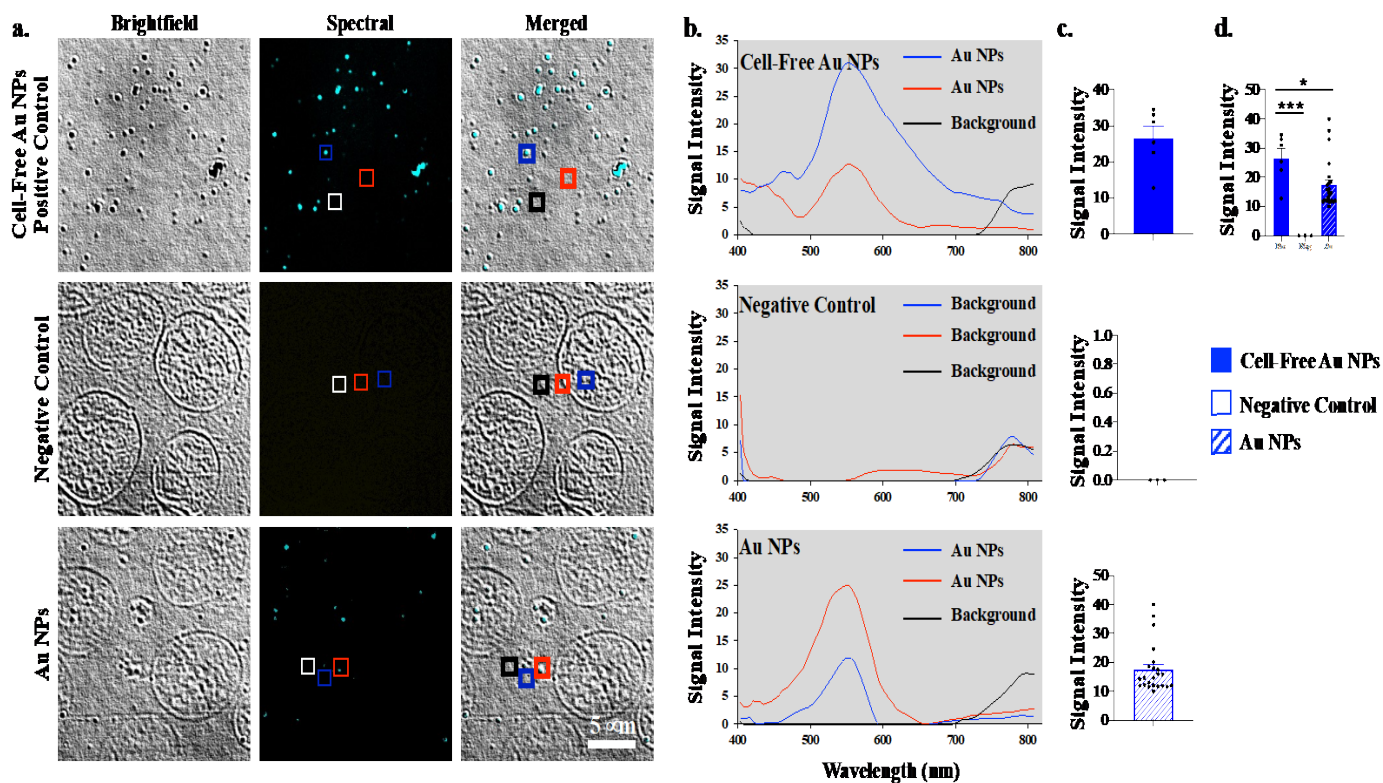


Figure 2-3: Identification of Au-NPs Spectra

(a) Brightfield images are shown for Au-NPs in the cell-free system (positive control), fixed cells (negative control), and 16-hour Au-NPs-treated cells. The pseudo-colored spectral images were extracted from the spectra libraries for Au-NPs. Merged images show combined brightfield and spectral images. (b) The graphs show the wavelength characteristics of the Au-NPs cluster at ~536 nm for the positive control and with cell incubation. Au-NPs graphs were shown after an automatic background subtraction by the software (See Method). The blue line displayed the area that contains higher wavelength intensity, and the red showed the region with less intensity. The background exhibited as a black color wavelength. The negative control graph shows the wavelengths. The negative control spectra were identified based on unmatched spectra from our libraries. (c) The bar graphs present the variation of intensity data points of the Au-NPs cluster peak of 536 nm. (d) The signal intensities were compared among cell-free positive control, non-treated cells negative control, and Au-NPs-treated cells. N=6 for each positive and negative controls; N=24 for experimental groups. *, P<0.05; ***, P<0.001.

We observed the continuous accumulation of Ag(s)-NPs in the cells. Our libraries could distinctively differentiate the core (pink color) and shell (yellow color) clusters of Ag(s)-NPs. Once the pixel identity of Ag(s)-NP signature spectra was identified, we randomly selected a pixel to study individual spectra after background subtraction (**Fig. 2-4b; Supp Fig. 3**). We quantified spectra representing NPs in the cytoplasm or nucleus within single cells (**Fig. 2-4c**). It was apparent that our Ag(s)-NPs were dynamically moving in and out of the cells, as depicted in the fluctuation in the total NPs in a single cell. The NPs were also moving in and out of the cell nucleus, as shown by the number of NPs in the nucleus at each time point. In this particular study, cells were also moving in or out from our field of view. More Ag(s)-NPs would eventually accumulate in the cells. Ag(s)-NPs would subsequently accumulate in the cell nucleus (**Supp Fig 2; Supp Fig. 3**).

We next studied time-lapse imaging of Au-NPs in single living cells (**Fig. 2-5a; Supp Fig. 4**). We noted the continuous accumulation of Au-NPs in the cells. Once the pixel resembling Au-NP spectral signature was identified, we randomly selected a pixel to study individual spectra after background subtraction (**Fig. 2-5b; Supp Fig. 5**). Through the time-lapse imaging to detect the movements of Au-NPs, we could quantify potential NPs in the cytoplasm or nucleus within single cells (**Fig. 2-5c**). It was apparent that Au-NPs were dynamically moving in and out of the cells, as indicated by the fluctuation in total NPs in a single cell at a single time point.

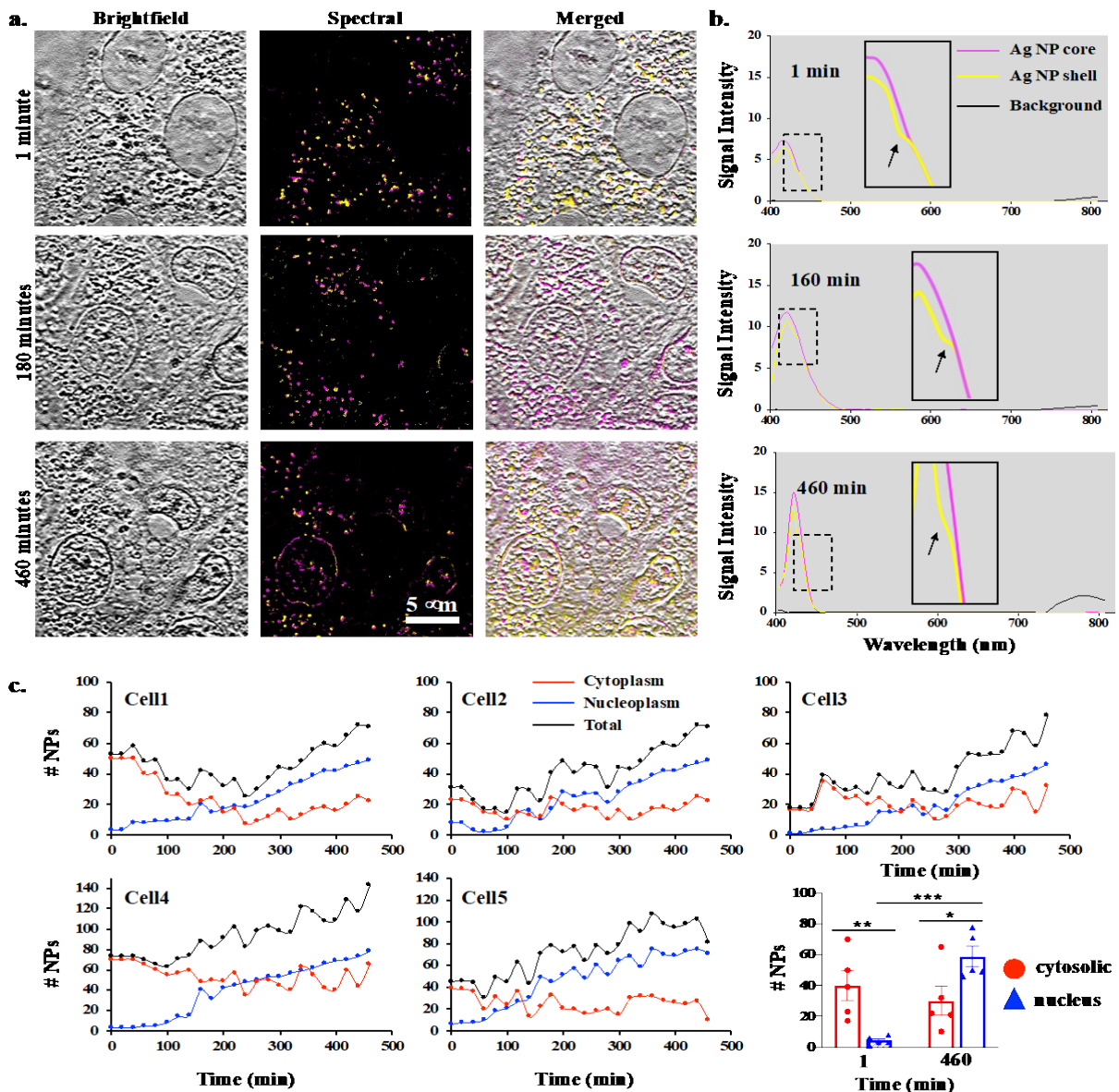


Figure 2-4: Time-lapse Imaging of Ag(s)-NPs

(a) Sequential time imaging of cells treated with 0.1 mg of Ag(s)-NPs in 2 mL media was captured for about 8 hours. Brightfield images and spectral scans were taken every 20 minutes (Supp Fig. 4). (b) Spectral analysis was performed at the end of 8 hours after subtraction from the background spectra (Supp Fig. 5). The Ag(s)-NPs libraries differentiated the core and shell of NP clusters. The pink wavelength displays the intensity of the core area; the yellow wavelength shows the shell part (with a small shoulder; insert and arrow). (c) Line graphs illustrate the time-lapse analysis from 5 independent experiments. A number of Ag-NPs (#NPs) was measured in one cell at each time point. Total #NPs were calculated from localization NPs in the cytoplasm (outside the nucleus) and nucleoplasm (inside the nucleus) within a cell. Comparisons were made at the beginning (1 min) and end (460 min) of the 8-hour experiments. N=5. *, P<0.05; **, P<0.01; ***, P<0.001.

Similarly, NPs were in and out of the cell nucleus as depicted by the number of NPs in the nucleus at each time point. As time passed, more NPs accumulated in the cells, but this accumulation was started from the cytoplasm and followed by the nucleus. It was evident that Au-NPs preferentially localized in the cell nucleus (**Supp Fig. 4; Supp Fig. 5**). While both Au-NPs and Ag(s)-NPs are largely known to localize in the nucleus (Berbeco et al., 2012), (Asharani et al., 2009), we showed for the first time the dynamics movements of Au-NPs and Ag-NPs in cytosol and nucleus (**Supp Fig. 2; Supp Fig. 4**).

Electron microscopy and silver-staining were used to verify the spectral imaging approach.

To verify our subcellular localization findings of NPs in time-lapse imaging studies, we performed transmission electron microscopy (TEM) and silver staining analyses. The TEM captured images cells treated with Ag(s)-NPs, Ag-NPs, and Au-NPs for 16 hours (**Fig. 2-6a; Fig. 2-7a**). While we were not able to capture the dynamics of these NPs due to the sample fixation, the TEM studies confirmed the accumulation of NPs in the cell nucleus. Likewise, the localization of NPs was confirmed to be mostly in the nucleus of cells using a silver staining to generate darker brown contrast in phase images (**Fig 2-6b; Fig. 2-7b**). Because the contrast was primarily enhanced by metallic silver attached at the peripheral of the NPs, the spectral signatures within the NPs were not much altered (**Fig 2-6c; Fig. 2-7c**).

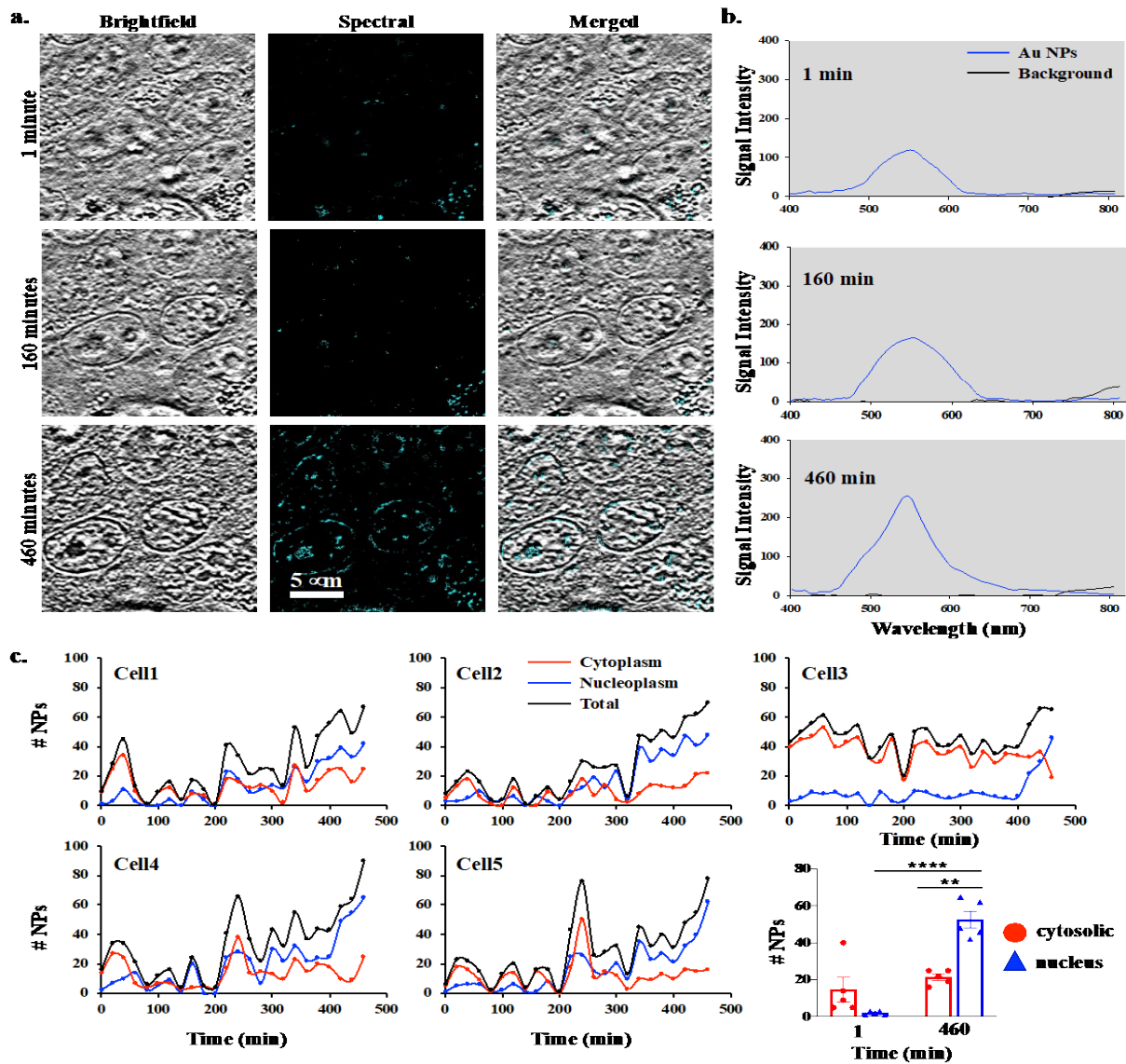


Figure 2-5: Time-lapse Imaging of Au-NPs

(a) Sequential time imaging of cells treated with Au-NPs was captured for about 8 hours. Brightfield image and spectral scan were taken at every 20 minutes (Supp Fig. 7). (b) Spectral analysis was performed at the end of 8 hours after subtraction from the background spectra (Supp Fig. 8). (c) Line graphs illustrate the time-lapse analysis from 5 independent experiments. Number of Au-NPs (#NPs) was measured in one cell at each time point. Total #NPs were calculated from localization NPs in cytoplasm (outside nucleus) and nucleoplasm (inside nucleus) within a cell. Comparisons were done at the beginning (1 min) and end (460 min) of the 8-hour experiments. N=5. **, P<0.01; ****, P<0.0001.

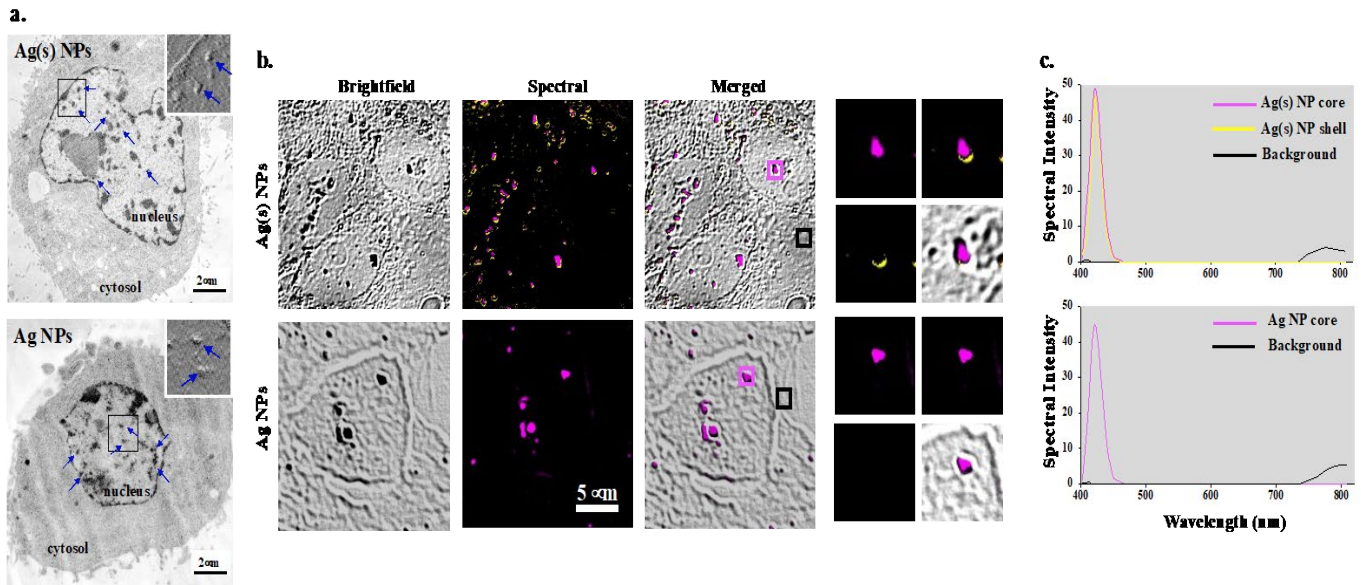


Figure 2-6: TEM & Silver Staining of Ag(s)-NPs and Ag-NPs

(a) TEM analyses were performed after treatment of Ag(s)-NPs or Ag-NPs for 16 hours. An embossing filter was applied in some regions of cell nucleus for better clarity of the presence of NPs (insert with arrows). (b) Cells after silver staining show brightfield images of the Ag(s)-NPs and Ag-NPs treated cells for 16 hours. The spectral images were extracted and pseudo-colored for the Ag(s)/Ag-NPs. Merged images revealed superimposed brightfield and spectral images to show the location of Ag(s)/Ag-NPs in the cell nucleus. The pink pseudocolor shows the core area of the Ag(s)/Ag-NPs, while the yellow color represents the shell region of Ag(s)-NPs. (c) The spectral graphs clarify the wavelength peaks of Ag(s)/Ag-NPs at ~420 nm. The pink wavelength exhibits the intensity of the core area; the yellow wavelength displays the shell region. The black color shows the spectrum of the background area. N=5.

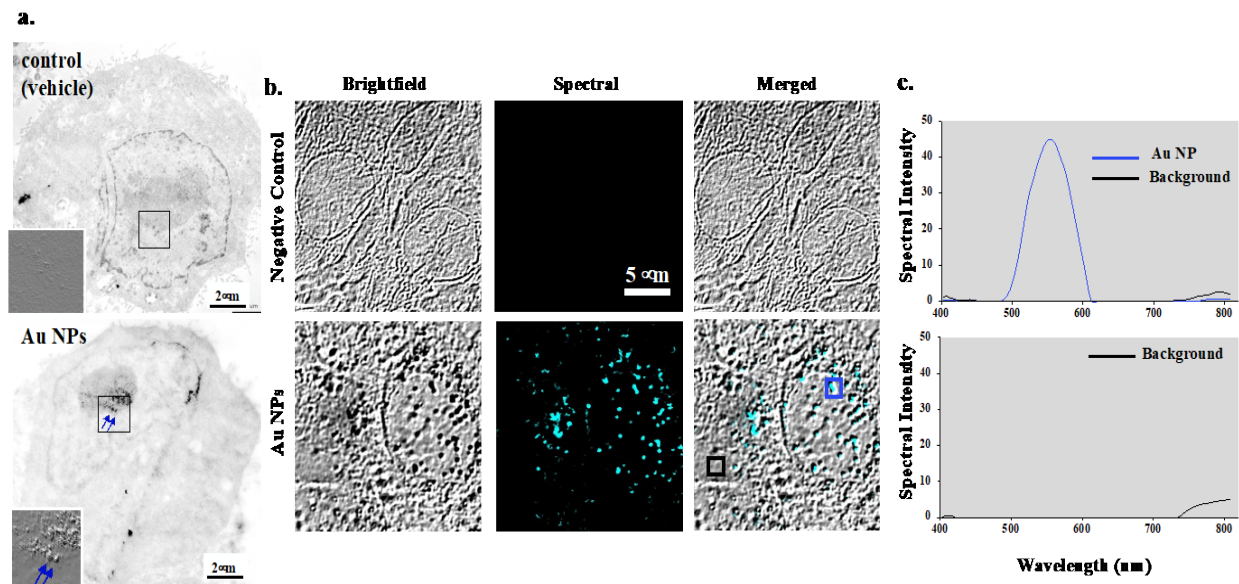


Figure 2-7: TEM & Silver Staining of AuNPs

(a) TEM analyses were performed after treatment of saline (control) or Au-NPs for 16 hours. An embossing filter was applied in some regions of cell nucleus for better clarity of the presence of NPs (insert with arrows). **(b)** Brightfield images of the silver stained non-treated (control) or 16 hours Au-NPs treated cells. The spectral images were extracted and pseudo-colored for the Au-NPs. Merged images revealed superimposed brightfield and spectral images to show the location of Au-NPs in the cell nucleus. **(c)** The spectral graphs clarify the wavelength peaks of Au-NPs at ~550 nm. N=5

Verification of spectral imaging approach was performed *in vivo* using ICP-MS.

We next assessed the practicality of SI to study the distribution of the NPs within mouse organ tissues. Remarkably, we found that distributions of the Ag(s)-NPs, Ag-NPs and Au-NPs in kidney, spleen, liver and heart tissues (**Fig. 2-8a, Figs. 2-9&2-10**). Importantly, the spectral characteristics of the core and shells of Ag(s)-NPs were not altered (**Fig. 2-8b,c**). Based on our quantitative analyses, we showed that Ag(s)-NPs and Ag-NPs were distributed highly in kidney and spleen, respectively (**Fig. 2-11a**). On the other hand, Au-NPs were in the liver (**Fig. 2-12a**). As a validation of the NPs distribution within the organs, we conducted ICP-MS analyses. Of note, ICP-MS method and its standard curve did not differentiate between Ag(s)-NPs and Ag-NPs (**Fig. 2-12b**). We performed separate analyses of those tissues for Ag(s)-NPs, Ag-NPs or Au-NPs (**Fig. 2-11b, Fig. 2-12c**). We next examined the correlation analyses of the NPs distribution. We found a significant correlation in Ag(s)-NPs and Ag-NPs distributions in SI and ICP-MS among the tissues (**Fig. 2-11c**). Likewise, a similar correlation was observed in Au-NPs (**Fig. 2-12d**), indicating a consistency between SI and ICP-MS approaches.

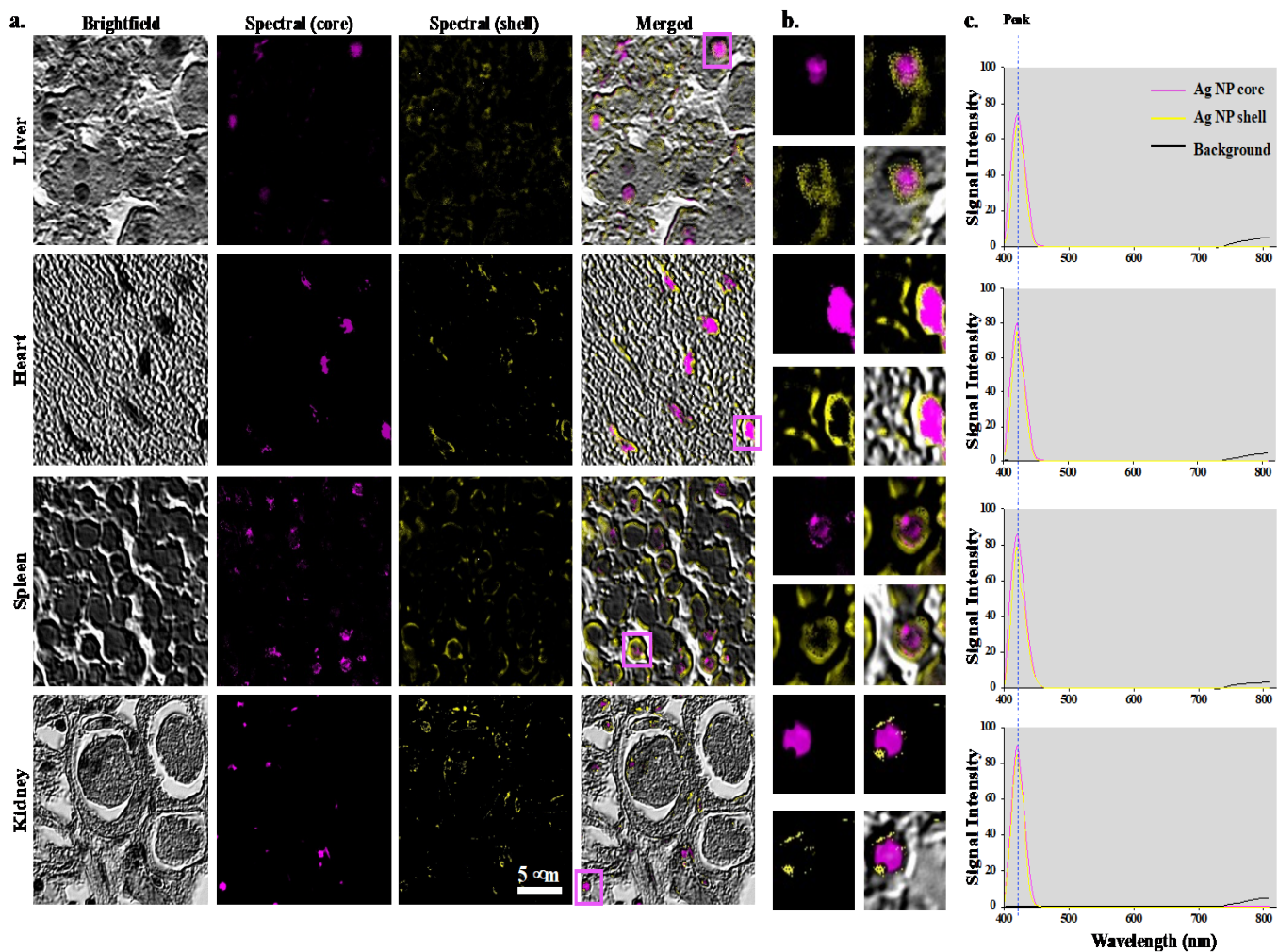


Figure 2-8: Distribution of Ag(s)-NPs in Animal Tissues

(a) Brightfield images of the Ag(s)-NPs at different organs tissues (liver, heart, spleen kidney) after intravenous injection with Ag(s)-NPs for 24 hours are shown. The spectral images were extracted from the spectra libraries for Ag(s)-NPs. Merged images display combined brightfield and spectral images. (b) The pink pseudo-colored images show the core area of the Ag(s)-NPs, while the yellow color exemplifies the shell region. (c) The graphs reveal the wavelength characteristics of the Ag(s)-NPs cluster at ~ 420 nm. The pink wavelength exhibits the intensity of the core area; the yellow wavelength displays the shell part. The background is shown as a black color wavelength. $N=5$.

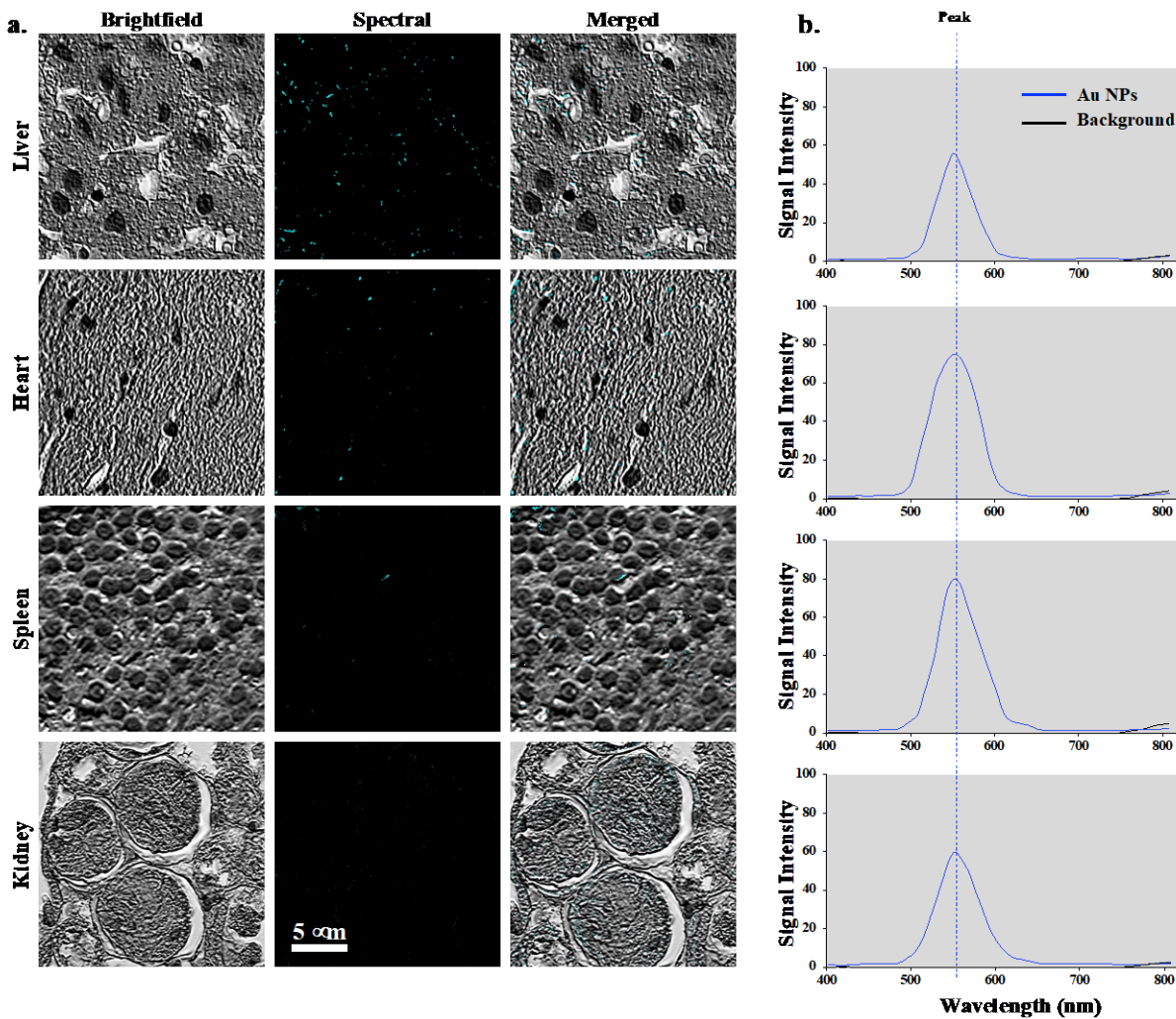


Figure 2-9: Distribution of AgNPs in Animal Tissues

(a) Brightfield images of the Ag-NPs in different organs tissues (liver, heart, spleen kidney) after intravenous injection of Ag-NPs for 24 hours. The spectral images were extracted from the spectra libraries for Ag-NPs. Merged images display combined brightfield and spectral images. (b) The Ag-NPs were shown in the pink pseudo-colored images. (c) The graphs reveal the wavelength characteristics of the Ag-NPs cluster at ~420 nm. The pink wavelength exhibits the intensity of the core area; the yellow wavelength displays the shell part. The background is shown as a black color wavelength. N=5.

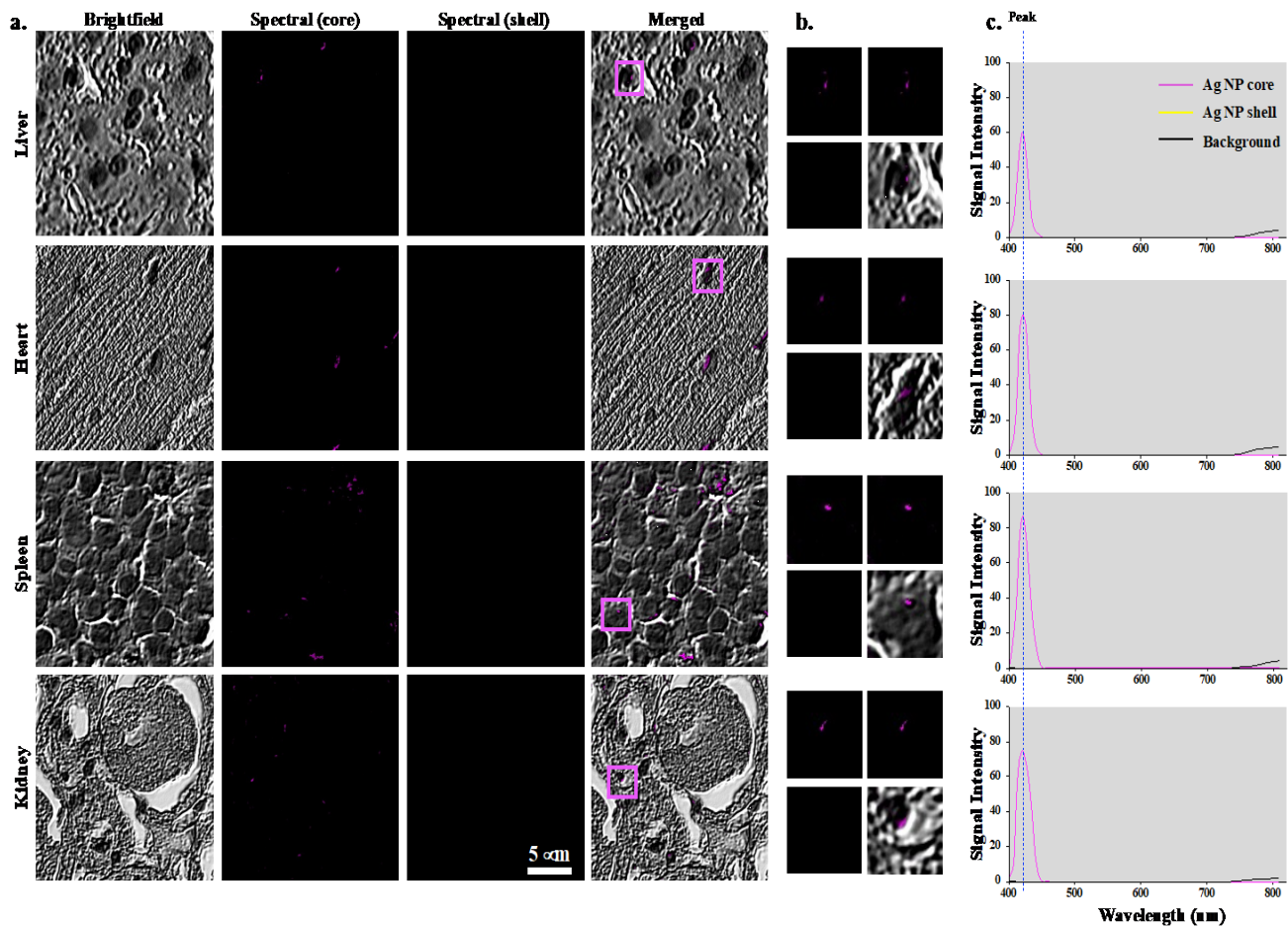


Figure 2-10: Distribution of AuNPs in Animal Tissues

(a) Brightfield images of the Au-NPs in different organs tissues (liver, heart, spleen kidney) after intravenous injection of Au-NPs for 24 hours. The spectral images were extracted from the spectra libraries for Au-NPs. Merged images display combined brightfield and spectral images. (b) The graphs reveal the wavelength characteristics of the Au-NPs at ~550 nm. The blue wavelength exhibits Au-NPs. The background is shown as a black color wavelength. N=5.

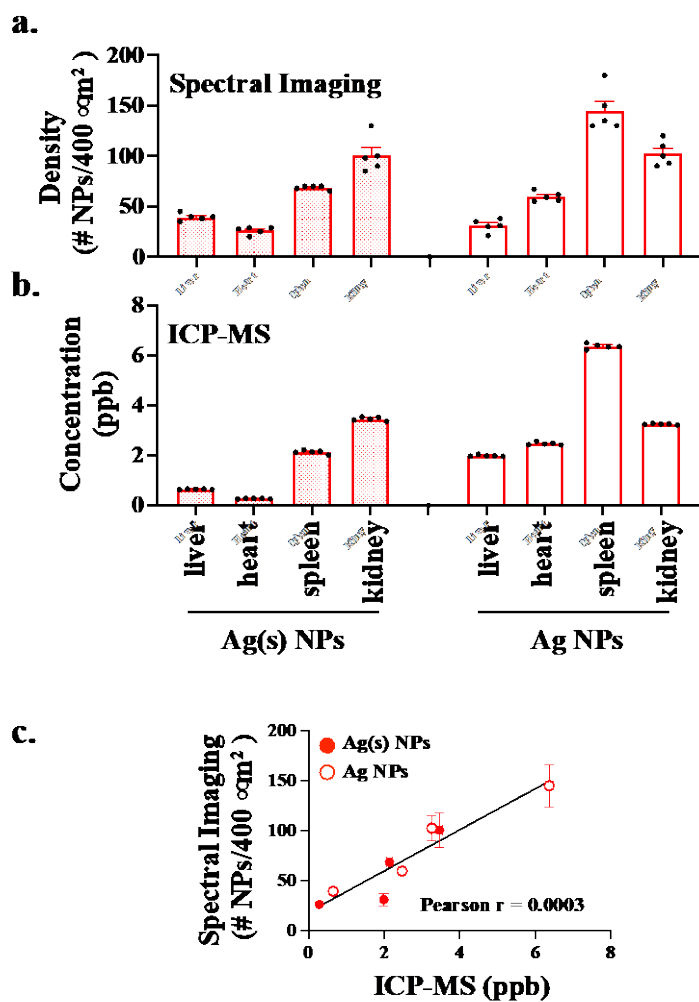


Figure 2-11: Correlation analysis of Ag(s)-NP and Ag-NP distributions in the tissues using spectral imaging and ICP-MS

The bar graphs exhibit the distributions of Ag(s)-NPs and Ag-NPs in liver, heart, spleen, kidney, which were done performed using spectral imaging (a) or ICP-MS (b). (c) The correlation analysis of the distribution of Ag(s)-NPs and Ag-NPs in different organs between ICP-MS and spectral imaging is shown. N = 5 for each group and organs.

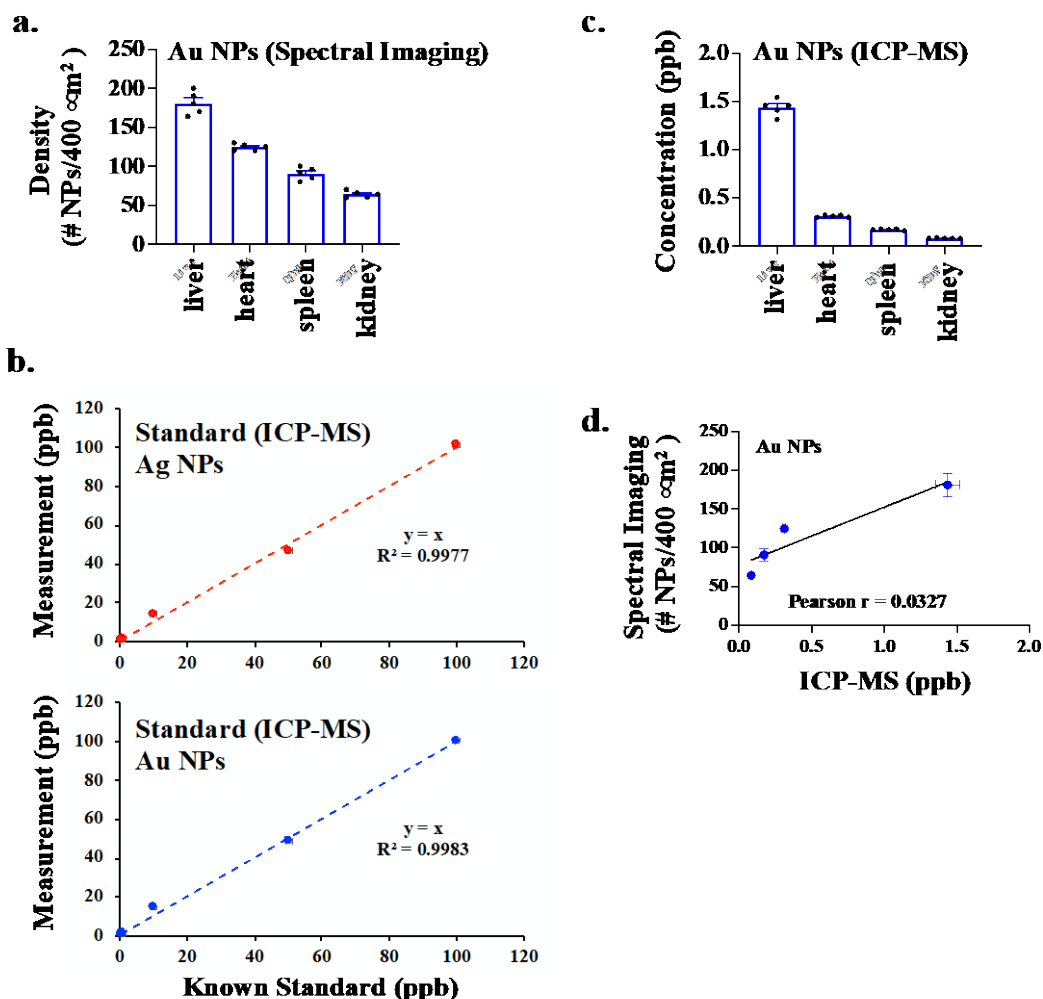


Figure 2-12: Correlation analysis of AuNP distributions in the tissues using spectral imaging and ICP-MS

(a) Tissue distribution of Au-NPs by spectral imaging is summarized in the bar graph. (b) Representative standard curves for ICP-MS are shown for Ag(s)-NPs and Au-NPs (0.5 to 100 ppb). (c) Tissue distribution of Au-NPs by ICP-MS is summarized in the bar graph. (d) The correlation analysis of the distribution of Au-NPs in different organs between ICP-MS and spectral imaging was performed. N=5 for each group.

2.5 Discussion

The significance of the use of SI in our studies are as follows. *First*, we were able to identify and quantify the presence of NPs without the need to destruct or liquify the samples. This allowed us to perform live-cell imaging that was otherwise not possible. *Second*, we could calibrate the spectra library by using both imaging and the singularity/plurality of spectra “signature” of a chemical. In Ag(s)-NPs, for example, we could pick up the plurality of spectra at the 420 nm, i.e., peak with or without a shoulder. Looking at the images, we showed that the peaks without shoulder were always at the center of NPs, whereas the peaks with a shoulder were localized at the peripheral. *Third*, we did not need to label our NPs with fluorescent. Labeling NPs required an additional step in the synthesis process, making the process more expensive and laborious. Labeled NPs could also alter the molecular functions and characteristics of NPs (Snipstad et al., 2017), (Tenuta et al., 2011a), (Corbo et al., 2016). *Fourth*, SI was also applicable to fluorescent or auto-fluorescent molecules. Using SI, we were able to perform fluorescent molecules fairly easily based mainly on its predominant fluorescence spectra (data not shown) (Alshammari et al., 2021). Note that the spectral identities might be different between non-labeled and fluorescent-labeled NPs. A fluorescence microscopy might be more practical to detect the fluorescent-labeled NPs. *Fifth*, the SI approach was a simple yet inexpensive method for unlabeled NPs, resolution of which was depended on the quality of lens and camera from standard optical microscopes. Unlike laser-based microscopic devices, such as Raman spectroscopy, SI systems could be installed on upright or inverted microscopes that were readily available in many research laboratories.

Using SI, we were able to observe the dynamic uptake, movement, and distribution of different types of free-labeled NPs in single cell. Conducting the live imaging technique with scanning the spectra from 400-800 nm, we were able to instigate the behaviors of the NPs in single cell, in which the NPs were eventually accumulate in the cell nucleus. The SI was validated by both TEM and silver staining studies, although TEM and silver staining techniques did not provide live-dynamics nature of NPs due to the requirement for cell fixation. In addition, we were able to study the distribution of NPs among tissue using the SI. We found that Ag(s)-NPs and Ag-NPs were primarily localized in kidney and spleen, respectively. On the other hand, Au-NPs were distributed primarily in the liver. Of note, these tissues could be easily visualized with a standard H&E staining, allowing easier sample preparation relative to the ICP-MS approach. Importantly, the SI was confirmed by the conventional ICP-MS technique with regards to tissue distribution analyses.

A few label-free methods have been produced for observing NPs in live cells. For examples, transitory absorption microscopy has been utilized to capture carbon nanotubes in cells, and scatter-enhanced phase-contrast microscopy has been utilized to assess the intracellular behavior of unlabeled silicon nanowires (Zimmerman et al., 2016b), (Tong et al., 2011). Other approaches such as hyperspectral stimulated Raman scattering microscopy (B. Huang et al., 2018b), optical diffraction tomography (D. Kim et al., 2018b), and dark-field microscopy (Gibbs-Flournoy et al., 2011), have been utilized to investigate unlabeled NPs inside cells. However, using current technology to track unlabeled NPs in live cells in real-time with reliable spatial resolution remains a challenge. Besides, it is necessary to monitor both NPs and biomolecules to fully comprehend the interaction between NPs and cells/tissues. To the best of our knowledge, no technique has utilized a broader band of spectra 400-800 for real-time imaging in label-free NPs. The broader

spectra is required to extract more precise characteristics of a single molecule (Alshammari et al., 2021). Specifically, this approach provides a more specific fingerprinting for each NPs.

2.6 Conclusion

In summary, the combination of spectroscopy and imaging provide high-resolution spatial and temporal information of spectra characteristics in each pixel. This approach could serve as a valuable technique to understand distribution, dynamic movement, and behavior of NPs used in biomedical research and clinical medicine.

References

- Alshammari, Q. A., Pala, R., Katzir, N., & Nauli, S. M. (2021). Label-free spectral imaging to study drug distribution and metabolism in single living cells. *Scientific Reports*, *11*(1), 2703. <https://doi.org/10.1038/s41598-021-81817-0>
- António, D. C., Cascio, C., Gilliland, D., Nogueira, A. J. A., Rossi, F., & Calzolari, L. (2016). Characterization of silver nanoparticles-alginate complexes by combined size separation and size measurement techniques. *Biointerphases*, *11*(4), 04B309. <https://doi.org/10.1116/1.4972112>
- Asharani, P. V., Hande, M. P., & Valiyaveetil, S. (2009). Anti-proliferative activity of silver nanoparticles. *BMC Cell Biology*, *10*, 65. <https://doi.org/10.1186/1471-2121-10-65>
- Berbeco, R. I., Korideck, H., Ngwa, W., Kumar, R., Patel, J., Sridhar, S., Johnson, S., Price, B. D., Kimmelman, A., & Makrigiorgos, G. M. (2012). DNA damage enhancement from gold nanoparticles for clinical MV photon beams. *Radiation Research*, *178*(6), 604–608. <https://doi.org/10.1667/RR3001.1>
- Chen, L. Q., Fang, L., Ling, J., Ding, C. Z., Kang, B., & Huang, C. Z. (2015). Nanotoxicity of silver nanoparticles to red blood cells: Size dependent adsorption, uptake, and hemolytic activity. *Chemical Research in Toxicology*, *28*(3), 501–509. <https://doi.org/10.1021/tx500479m>
- Chen, L. Q., Xiao, S. J., Peng, L., Wu, T., Ling, J., Li, Y. F., & Huang, C. Z. (2010). Aptamer-based silver nanoparticles used for intracellular protein imaging and single nanoparticle spectral analysis. *The Journal of Physical Chemistry. B*, *114*(10), 3655–3659. <https://doi.org/10.1021/jp9104618>

- Claes, N., Asapu, R., Blommaerts, N., Verbruggen, S. W., Lenaerts, S., & Bals, S. (2018). Characterization of silver-polymer core-shell nanoparticles using electron microscopy. *Nanoscale*, *10*(19), 9186–9191. <https://doi.org/10.1039/c7nr09517a>
- Corbo, C., Molinaro, R., Parodi, A., Toledano Furman, N. E., Salvatore, F., & Tasciotti, E. (2016). The impact of nanoparticle protein corona on cytotoxicity, immunotoxicity and target drug delivery. *Nanomedicine (London, England)*, *11*(1), 81–100. <https://doi.org/10.2217/nnm.15.188>
- Ertem, E., Gutt, B., Zuber, F., Allegri, S., Le Ouay, B., Mefti, S., Formentin, K., Stellacci, F., & Ren, Q. (2017). Core-Shell Silver Nanoparticles in Endodontic Disinfection Solutions Enable Long-Term Antimicrobial Effect on Oral Biofilms. *ACS Applied Materials & Interfaces*, *9*(40), 34762–34772. <https://doi.org/10.1021/acsami.7b13929>
- Fayaz, A. M., Balaji, K., Girilal, M., Yadav, R., Kalaichelvan, P. T., & Venketesan, R. (2010). Biogenic synthesis of silver nanoparticles and their synergistic effect with antibiotics: A study against gram-positive and gram-negative bacteria. *Nanomedicine: Nanotechnology, Biology, and Medicine*, *6*(1), 103–109. <https://doi.org/10.1016/j.nano.2009.04.006>
- Gibbs-Flournoy, E. A., Bromberg, P. A., Hofer, T. P. J., Samet, J. M., & Zucker, R. M. (2011). Darkfield-confocal microscopy detection of nanoscale particle internalization by human lung cells. *Particle and Fibre Toxicology*, *8*(1), 2. <https://doi.org/10.1186/1743-8977-8-2>
- Haiss, W., Thanh, N. T. K., Aveyard, J., & Fernig, D. G. (2007). Determination of size and concentration of gold nanoparticles from UV-vis spectra. *Analytical Chemistry*, *79*(11), 4215–4221. <https://doi.org/10.1021/ac0702084>
- Huang, B., Yan, S., Xiao, L., Ji, R., Yang, L., Miao, A.-J., & Wang, P. (2018a). Label-Free Imaging of Nanoparticle Uptake Competition in Single Cells by Hyperspectral Stimulated

- Raman Scattering. *Small (Weinheim an Der Bergstrasse, Germany)*, 14(10).
<https://doi.org/10.1002/sml.201703246>
- Kim, D., Oh, N., Kim, K., Lee, S., Pack, C.-G., Park, J.-H., & Park, Y. (2018b). Label-free high-resolution 3-D imaging of gold nanoparticles inside live cells using optical diffraction tomography. *Methods (San Diego, Calif.)*, 136, 160–167.
<https://doi.org/10.1016/j.ymeth.2017.07.008>
- Lee, S., Bi, X., Reed, R. B., Ranville, J. F., Herckes, P., & Westerhoff, P. (2014). Nanoparticle size detection limits by single particle ICP-MS for 40 elements. *Environmental Science & Technology*, 48(17), 10291–10300. <https://doi.org/10.1021/es502422v>
- Ling, J., Li, Y. F., & Huang, C. Z. (2009). Visual sandwich immunoassay system on the basis of plasmon resonance scattering signals of silver nanoparticles. *Analytical Chemistry*, 81(4), 1707–1714. <https://doi.org/10.1021/ac802152b>
- Pala, R., Mohieldin, A. M., Shamloo, K., Sherpa, R. T., Kathem, S. H., Zhou, J., Luan, Z., Zheng, J.-G., Ahsan, A., & Nauli, S. M. (2019). Personalized Nanotherapy by Specifically Targeting Cell Organelles To Improve Vascular Hypertension. *Nano Letters*, 19(2), 904–914. <https://doi.org/10.1021/acs.nanolett.8b04138>
- Pala, R., Mohieldin, A. M., Sherpa, R. T., Kathem, S. H., Shamloo, K., Luan, Z., Zhou, J., Zheng, J.-G., Ahsan, A., & Nauli, S. M. (2019). Ciliotherapy: Remote Control of Primary Cilia Movement and Function by Magnetic Nanoparticles. *ACS Nano*, 13(3), 3555–3572.
<https://doi.org/10.1021/acsnano.9b00033>
- Patskovsky, S., Bergeron, E., Rioux, D., & Meunier, M. (2015). Wide-field hyperspectral 3D imaging of functionalized gold nanoparticles targeting cancer cells by reflected light

- microscopy. *Journal of Biophotonics*, 8(5), 401–407.
<https://doi.org/10.1002/jbio.201400025>
- Shekhawat, G. S., & Dravid, V. P. (2005). Nanoscale imaging of buried structures via scanning near-field ultrasound holography. *Science (New York, N.Y.)*, 310(5745), 89–92.
<https://doi.org/10.1126/science.1117694>
- Snipstad, S., Hak, S., Baghirov, H., Sulheim, E., Mørch, Ý., Lélú, S., von Haartman, E., Bäck, M., Nilsson, K. P. R., Klymchenko, A. S., de Lange Davies, C., & Åslund, A. K. O. (2017). Labeling nanoparticles: Dye leakage and altered cellular uptake. *Cytometry. Part A: The Journal of the International Society for Analytical Cytology*, 91(8), 760–766.
<https://doi.org/10.1002/cyto.a.22853>
- Spicer, G. L. C., Almassalha, L., Martinez, I. A., Ellis, R., Chandler, J. E., Gladstein, S., Zhang, D., Nguyen, T.-Q., Feder, S., Subramanian, H., de la Rica, R., Thompson, S. A., & Backman, V. (2018). Label free localization of nanoparticles in live cancer cells using spectroscopic microscopy. *Nanoscale*, 10(40), 19125–19130.
<https://doi.org/10.1039/c8nr07481j>
- Tenuta, T., Monopoli, M. P., Kim, J., Salvati, A., Dawson, K. A., Sandin, P., & Lynch, I. (2011a). Elution of labile fluorescent dye from nanoparticles during biological use. *PloS One*, 6(10), e25556. <https://doi.org/10.1371/journal.pone.0025556>
- Tetard, L., Passian, A., Venmar, K. T., Lynch, R. M., Voy, B. H., Shekhawat, G., Dravid, V. P., & Thundat, T. (2008). Imaging nanoparticles in cells by nanomechanical holography. *Nature Nanotechnology*, 3(8), 501–505. <https://doi.org/10.1038/nnano.2008.162>
- Tong, L., Liu, Y., Dolash, B. D., Jung, Y., Slipchenko, M. N., Bergstrom, D. E., & Cheng, J.-X. (2011). Label-free imaging of semiconducting and metallic carbon nanotubes in cells and

- mice using transient absorption microscopy. *Nature Nanotechnology*, 7(1), 56–61.
<https://doi.org/10.1038/nnano.2011.210>
- Vanhecke, D., Rodriguez-Lorenzo, L., Clift, M. J. D., Blank, F., Petri-Fink, A., & Rothen-Rutishauser, B. (2014). Quantification of nanoparticles at the single-cell level: An overview about state-of-the-art techniques and their limitations. *Nanomedicine (London, England)*, 9(12), 1885–1900. <https://doi.org/10.2217/nnm.14.108>
- Wang, F., Chen, B., Yan, B., Yin, Y., Hu, L., Liang, Y., Song, M., & Jiang, G. (2019). Scattered Light Imaging Enables Real-Time Monitoring of Label-Free Nanoparticles and Fluorescent Biomolecules in Live Cells. *Journal of the American Chemical Society*, 141(36), 14043–14047. <https://doi.org/10.1021/jacs.9b05894>
- Zimmerman, J. F., Parameswaran, R., Murray, G., Wang, Y., Burke, M., & Tian, B. (2016a). Cellular uptake and dynamics of unlabeled freestanding silicon nanowires. *Science Advances*, 2(12), e1601039. <https://doi.org/10.1126/sciadv.1601039>

Chapter 3: Identification of Organics Metabolite

Alshammari, Q. A., Pala, R., Katzir, N., & Nauli, S. M. (2021). Label-free spectral imaging to study drug distribution and metabolism in single living cells. *Scientific Reports*, *11*(1), 2703. <https://doi.org/10.1038/s41598-021-81817-0>

Author contributions

Q.A.A. collected data, analyzed data and drafted the manuscript. R.P. designed research and oversaw the study. N.K. participated in the spectral imaging system and software analysis. S.M.N. conceived the idea, designed research and oversaw the experimental progress. All authors were participating in finalizing the draft of the manuscript.

3.1 Abstract

During drug development, evaluation of drug and its metabolite is an essential process to understand drug activity, stability, toxicity and distribution. Liquid chromatography (LC) coupled with mass spectrometry (MS) has become the standard analytical tool for screening and identifying drug metabolites. Unlike LC/MS approach requiring liquifying the biological samples, we showed that SI (or spectral microscopy) could provide high-resolution images of dox and its metabolite dox'ol in single living cells. Using this new method, we performed measurements without destroying the biological samples. We calculated the rate constant of dox translocating from extracellular moiety into the cell and the metabolism rate of dox to dox'ol in living cells. The

translocation rate of dox into a single cell for spectral microscopy and LC/MS approaches was similar ($\sim 1.5 \text{ pM min}^{-1} \text{ cell}^{-1}$). When compared to spectral microscopy, the metabolism rate of dox was underestimated for about every 500 cells using LC/MS. The microscopy approach further showed that dox and dox'ol translocated to the nucleus at different rates of 0.8 and 0.3 pM min^{-1} , respectively. LC/MS is not a practical approach to determine drug translocation from cytosol to nucleus. Using various methods, we confirmed that when combined with a high-resolution imaging, spectral characteristics of a molecule could be used as a powerful approach to analyze drug metabolism. We propose that spectral microscopy is a new method to study drug localization, translocation, transformation and identification with a resolution at a single cell level, while LC/MS is more appropriate for drug screening at an organ or tissue level.

3.2 Introduction

A standard imaging gives the intensity at each pixel of the image, and a conventional spectrometer provides spectral information of chemical substances. SI merges these two elements by providing an intensity and spectral information for each pixel of an image (Garini et al., 2006). Spectral information from images has been used to distinguish physiological changes and disease states from tissue samples from various organs (Li et al., 2013). However, SI is yet to be confirmed for use in drug development. While SI might provide a variety of image information as seen in Raman or fluorescence microscopy technique, we here focused on the use of the spectral microscopy that uses the absorption and emission spectral information.

The SI system was first introduced by NASA and the remote earth sensing community for monitoring temperature change and weather pattern. The SI has since been used for utilizing in academic and biomedical applications. SI has been broadly developed as a useful quantitative

technique in biomedical research. For example, it has been proposed for the *in vivo* melanoma detection based on color dispersal and morphology of the lesions (Tomatis et al., 2005), determination of the blood–brain barrier opening process for drug release (Feng et al., 2019), examination of autophagy and apoptosis regions (Dolloff et al., 2011) and differential observation of vascular tissues from non-vascular regions of skin (Tumeh et al., 2007). In addition, SI is also used to monitor the dynamic alterations of the tumor vasculature in living animals (Mayes et al., 2008) and visualize drugs absorption delivered through topical application (Saar et al., 2011). Such approaches with unique spectral characteristics of molecules can provide detailed information with a high spatial and temporal resolution.

Drug metabolite identification can enhance our understanding of pharmacological response to improve lead compounds, distinguish new biochemical substances and reduce drug toxicity/interaction (Z. Zhang et al., 2009). Quadrupole time- of-flight (QTOF) liquid chromatography and mass spectrometry (LC/MS) are commonly used to identify drug metabolites. These methods provide distinguishable quantitation between parental drug and its metabolites, based on their mass-to-charge ratio (m/z). The matrix-assisted laser desorption ionization time-of-flight mass spectrometry (MALDI-TOF/MS) is another analytical system of identification and characterization based on the fast and precise evaluation of the mass of molecules. However, the major drawback of these approaches is that they will destroy the biological samples. Besides, none of these techniques allows subcellular localization of the organic substances in the biological samples without the use of labeling (X. Liu & Jia, 2007).

dox is one of the anthracycline molecules. It is one of the most effective and prescribed anti- cancer drug. The anticancer action of dox depends mostly on its direct interaction with nucleic acids,

leading to DNA damage and inhibition of DNA synthesis (Minotti et al., 2004). In general, dox is used in the medical treatment for breast cancer, leukemia, lymphomas, and sarcomas (Damiani et al., 2016). However, due to its potential metabolite, the use of dox has resulted in various side effects.

Evaluation of drug and its metabolite requires either labeling the drug molecule or liquifying the biological sample, despite the fact that such labeling is not stable and can alter the functionality of the molecules (Garini et al., 2006), (Rubakhin et al., 2011), (Tenuta et al., 2011b). In our current study, we chose non-labelled dox as our experimental drug due to its known spectral characteristic at 592 nm (Agudelo et al., 2014). We measured the spectrum at the range of 500 nm to 750 nm with a single triple band filter called “SKY” to detect the dox level in the samples. We also characterized dox metabolite, non-labelled dox’ol (Schaupp et al., 2015). Rhodamine 6G was also used to confirm our findings on dox, because rhodamine shares very similar emission spectra with dox. Our spectral microscopy data were confirmed and compared with the standard QTOF-LC/MS method. While both methods were corresponded to each other, we also found that the spectral microscopy had a better advantage to study cellular compartmentalization of small molecules.

3.3 Materials and Methods

Materials

Doxorubicin hydrochloride (MW: 579.98 g/mol, lot# Q5L8K -FB) was purchased from TCI America; doxorubicinol (hydrochloride; MW: 582 g/mol, lot# 22386) from Cayman Chemical Company anhydrous methanol HPLC grade ($\geq 99.8\%$, lot# SHBG6650V), acetonitrile HPLC grade (≥ 99.9) and rhodamine 6G (MW: 479.01 g/mol, lot# BCBP8335V) were obtained from

Sigma Aldrich (St. Louis, MO); trifluoroacetic Acid (TFA) from EMD Millipore Corporation; formic acid (lot# 2595C389) and sucrose from Fisher Scientific (Fair Lawn, NJ); LL-CPK1 (ATCC; CL101.1TM) porcine renal epithelial cells from proximal tubule were obtained from American Type Culture Collection (ATCC; Manassas, VA). Trypsin, penicillin-streptomycin solution (lot# 04619001), Dulbecco's Modified Eagle Medium (DMEM) (lot# 20818006), and phosphate-buffered saline (PBS) (lot# 05319001) were purchased from Corning (Manassas, VA). Fetal bovine serum (FBS) was obtained from Seradigm (Logan, UT); Mounting Media HistoChoice from Amresco; and, Lysis buffer from Thermo scientific (Rockford, IL), paraformaldehyde (PFA) from Electron Microscopy Services (Hatfield, PA); and protease inhibitor cocktail from Complete (Mannheim, Germany).

Cell culture

At 37 °C, 5 % CO₂, and 95 percent humidity, LL-CPK1 cells were grown to a confluent monolayer in DMEM supplemented with 10% FBS and 1% penicillin–streptomycin. When cells achieved 70–90 percent confluence, they were trypsinized (using a 0.05 percent solution of trypsin) on a regular basis for passage. Cells were grown to confluency before being treated with drugs (dox, dox'ol, or rhodamine) in our investigations.

UV–VIS and fluorescence spectrum detection

The ultraviolet-visible (UV–VIS) and fluorescence spectra for dox and rhodamine 6G were read using a spectrophotometer (SpectraMax M5 Microplate Reader). All compounds were prepared in methanol at various concentrations of 0.1, 0.25, 0.5, 0.75, and 1 M. All of the compounds' UV

spectrums were scanned using a wavelength range of 200–800 nm. For dox and rhodamine, the fluorescence spectrum ranged from 400 to 800 nm.

Detection and quantification of mass spectrometry and UV–VIS HPLC

To validate that extra peak in dox (520 nm) representing the metabolite species of dox (dox'ol), different concentrations of the pure dox'ol (0.5, 0.8, 1, 10 and 50 μM) and a mixture of pure dox and dox'ol (80 and 20%, respectively) prepared for confirmation with the mass spectra by Quadrupole Time-of-Flight (QTOF) Liquid chromatography-mass spectrometry (LC-MS) system (Bruker Impact II and Ultimate 3000 UPLC (Dionex)).

Cell treatment

Under normal growth conditions, cells were seeded into sterile 22×22 mm coverslips (Globe Scientific) in a 6 well plate (Greiner bio-one Cellstar®, total volume of 2 mL at each well) until they reached 70–80 percent confluency. The cells were then given 100 μL of dox'ol, with concentrations ranging from 0.1 to 50 mM. The cells were then rinsed three times in PBS and fixed for 10 minutes at room temperature in a fixing solution (2.5 mL PFA, 7.5 mL PBS, and 0.2 g sucrose). The coverslip was then placed on the slide, which held 25 μL of mounting material, and left at room temperature overnight.

Spectral imaging (spectral microscopy)

SI instrument (ASI Spectral Imaging System) and Olympus microscope (Model BX61) were used. Manual image acquisition conducted with 60X magnification fields. Xenon arc lamp was used as our light source. Spectral filter (SKY) used to identify the wavelengths of the pure dox, dox'ol and

rhodamine 6G. SKY filter produced a spectrum that had a background-subtracted spectral type. Each chemical was measured for its spectral characteristic, also known as spectral signature. After the spectrum of the background was subtracted, it was saved in a spectral library. The library was later on used for various spectral analysis tasks. For instance, to compare the dox spectrum with the background spectrum, we defined markers in the area that contained the chemical substance (dox) and in the area that did not have dox (background). Spectrum was collected from 400 to 800 nm with a step size of 20 nm. We subsequently displayed the two spectra (dox and background). The dox spectra were acquired by subtracting the background spectra. After that, we uploaded these spectra as libraries for further cell analysis. Subsequently, images of the cells that were treated with the chemicals were captured randomly by using SKY and brightfield filters. At least 10 field of views were captured per each concentration sample that was prepared. Afterward, we analyzed the images by using the spectral libraries of the chemicals and scanned all the areas to obtain the location that only matched within the chemical library. For dox, rhodamine, and dox'ol samples, we used SUN analysis (within the Spec- traView software, Applied Spectral Imaging), performed Spectral UNmixing, divided a set of images into layers that matched to the original spectra (libraries). This allowed us to quantify the amount and identify the location of the material according to its original spectra.

Our system used a standard microscopy set-up (**Fig. 3-1**). This set-up was widely available in most laboratories. The use of sagnac interferometer was also very common. The beam splitter split the light originating from the selected area in the sample into two beams. A set of mirrors led the beams down two paths of various lengths. At the end of the paths, the two beams combined. At the point when the two beams merged, they were super- imposed. The total intensity of these two superimposed beams was a function of the variance in the distance between the two paths. This

path variance was called the Optical Path Difference (OPD). The intensity of the merged beam was then captured by the Charged-Coupled Device (CCD) camera. Each measurement was called a frame, which was a simple gray level image measured by the CCD camera. Many frames were acquired, using different OPDs in each pixel to build a spectral image. At each OPD, this process arose simultaneously for each pixel in the image. At each pixel, all the frames acquired for that pixel were used to build an interferogram. An interferogram was an illustration of the light intensity, which might vary with each altering OPD. Each pixel's interferogram was transformed into that pixel's spectrum. The interferograms of all the pixels taken together permitted the rebuilding of the entire image's spectrum. Fourier transformation allowed us to convert the interferogram from each pixel into a pixel's spectrum. Through merging Fourier transformation with spectroscopy, we were able to further analyze the spectra of microscopic samples.

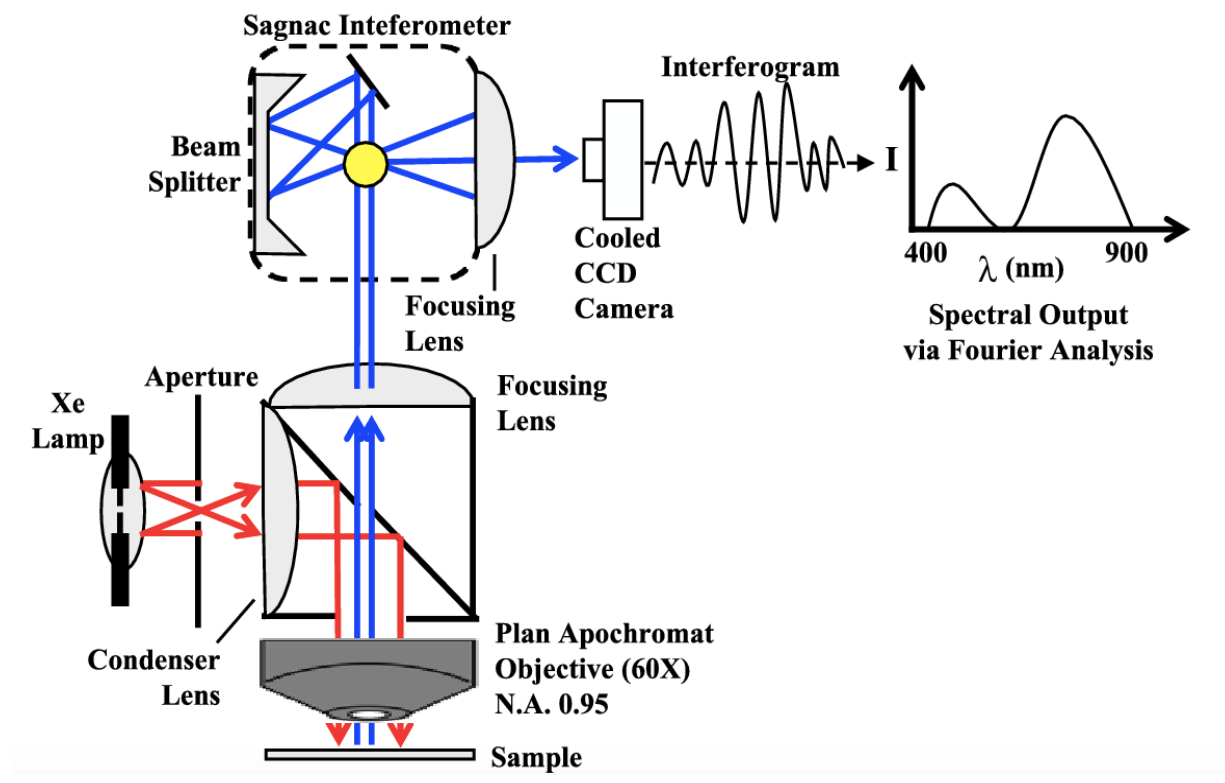


Figure 3-1: Diagram of the spectral microscopy set-up.

Time-lapse imaging

LLCPK cells were grown in six-well plate and treated with 1 nM dox or 0.01 nM rhodamine.

Cells were captured directly (without fixation) using brightfield and SI every 20 min for 8 h.

Cell Lysate

To validate that extra peak in dox (520 nm) representing the metabolite species of dox (dox'ol), different concentrations of the pure dox'ol (0.5, 0.8, 1, 10 and 50 μM) and a mixture of pure dox and dox'ol (80 and 20%, respectively) prepared to check the mass spectra by QTOF. In a different experiment, cells were treated with 2 μM of dox and dox'ol separately at different incubation times (18, 26, 42 h). Then, cells were washed using PBS by keeping the plates on the ice for all the steps. After that, 200 μL of lysis buffer supplemented with protease inhibitor cocktail were added to the cells; the cells were isolated by using a cell scraper (VWR; Radnor, PA) and transferred the lysate to a 5 mL Eppendorf. Afterward, the cells were centrifuged at $14,000\times g$ for 10 min at 4 $^{\circ}\text{C}$. Finally, the supernatant was collected by avoiding the pellet and put into new vials for QTOF analysis.

Metabolite identification

The major metabolite of dox is dox'ol, and alcohol metabolite is the primary metabolic route of dox metabolism to dox'ol (Schaupp et al., 2015), (Boucek et al., 1987), (X. Wang et al., 2019). Two-electrons of a side chain of the C-13 carbonyl group (**Fig. 3-2**) were reduced by aldo-keto reductase (AKR) and short-chain dehydrogenase/reductase (Zeng et al., 2019), (Salvatorelli et al., 2017). To confirm the peak at 520 nm was belonged to dox'ol, cells were treated with 100 μL dox'ol at different concentrations (0.1, 1, 10, 50 μM) with a total volume of 2 mL for 18 h. Then, cells were washed three times with PBS and fixed for 10 min in fixing solution at room temperature. After that, cells were mounted with 25 μL of Mounting Media overnight at room temperature. Finally, SI was used for further analysis by using the same approach of dox (manual image acquisition with 60X magnification fields, use SKY and bright-field filters, at least 10 capturing for each concentration).

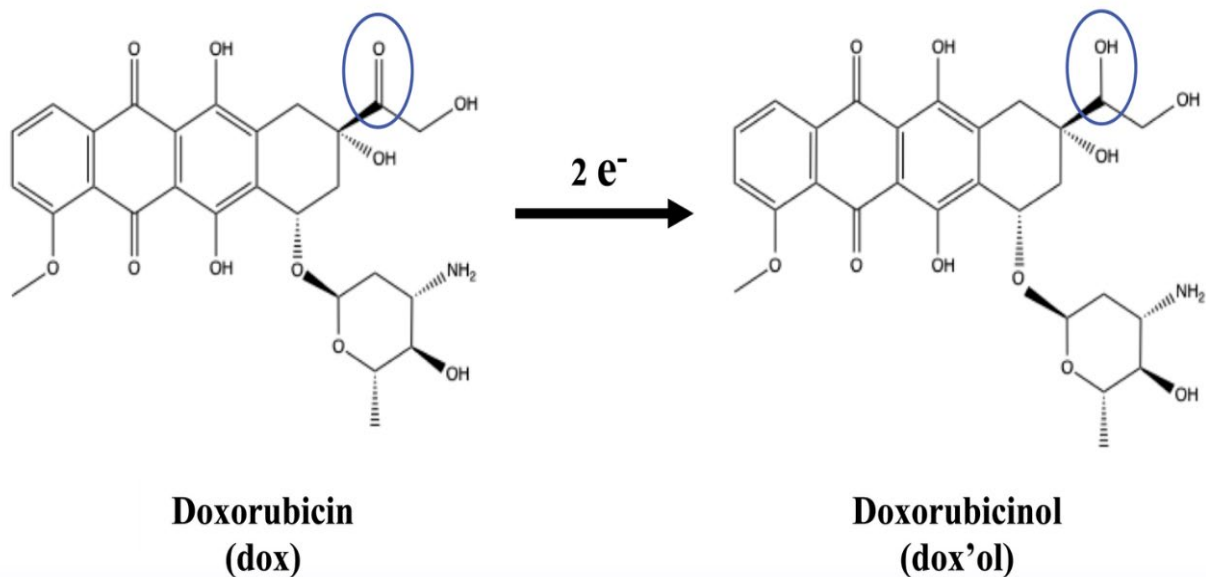


Figure 3-2: Diagram of Dox Converted to Dox'ol at the Side Chain of the C-13 Carbonyl Group.

Subcellular drug distribution

After capturing the brightfield image and spectral information of the cells, we analyzed the image using the spectral (or wavelength) library. We made boundaries for the nucleus as our region of interest (ROI) from the brightfield image (Supp Fig. S12). Because the cells were fully confluent, anything outside the ROI was considered cytoplasm. Please note that the spectral information initially contained no image; it only contained absorption/emission information, similar to a standard spectrophotometer. However, the spectral information containing dox-specific spectral could be extracted and converted to an image. The positive control provided information of dox-specific spectral, which had been stored in the library (after background subtraction). We could recall the spectral that resembled the spectra library (i.e. dox-specific spectra). These spectra were projected as a pseudocolored image. Thus, each pixel of the image contained its own spec-

information; in this case, the information was the dox-specific spectra. The pseudocolored image obtained and processed from the spectra information was then transferred to the brightfield image (containing ROI for nuclei). The superimposed pseudocolored and brightfield image was saved and labeled as a “merged” image. Thus, in the merged image we could obtain both ROI and spectral identity of dox to distinguish dox localization in nucleoplasm or cytoplasm.

Image and statistical analyses

Most of our image and statistical analyses were conducted by using SI software (GenASIs) version 7.2.7.34276 and GraphPad Prism software version 8. Microsoft Excel software version 16 was also used for linear regression analysis to obtain a standard calibration curve and linear equation. Comparisons between two groups were analyzed with two-tailed Student t-tests. Drawing of computer setup (Fig. 3-1) was made using Microsoft PowerPoint software version 16. ChemDraw version 18 was used to draw the chemical structures (Fig. 3-2). The spectral microscopy workflow (Supp Fig. S12) was self-created from the paid-online subscription at BioRender (Invoice #CEE5813A-0003; Receipt #2338-5420).

The intracellular distribution of dox was calculated from data collected at different time points. Unlike LC/ MS approach where different samples were used at each time point, SI allowed us to use a single same sample for multiple time points. We obtained the rate constant (k_1) of dox influx into a cell using SI approach (or cell lysate for LC/MS approach). Because one molecule of dox is converted to one molecule of dox'ol, the k_1 was calculated from the slope of total dox and dox'ol in a cell. Thus, k_1 is equivalent to the total dox and dox'ol in a cell for a given time.

We also calculated enzyme kinetics for dox using the enzyme kinetic Michaelis–Menten equation:

$$V = \frac{V_{\max}[\text{Dox}]}{K_m + [\text{Dox}]}$$

V is velocity of conversion from dox to dox'ol; dox'ol formation at a given time. V_{\max} is maximum rate of chemical conversion. [Dox] is the concentration of dox in a single cell or lysate. And, K_m is Michaelis–Menten constant. Using a similar idea as in k_1 , we calculated rate constant of drug influx into cell nucleus. We simply measured the accumulation of dox (k_2) and dox'ol (k'_2) in the nucleus. The rate constant was calculated from the slope of total dox or total dox'ol accumulated in the nucleus. Thus, k_2 and k'_2 are equivalent to the respective total dox and total dox'ol in a nucleus for a given time.

3.4 Results

The spectral microscopy system indicates localization of dox and its metabolite dox'ol to cell nucleus.

The pure dox spectral characteristics were captured using the SKY filter in cell-free (positive control) and fixed-cell systems. The spectral images revealed dox location in the cell, which mainly localized in the nucleus (**Supp Fig. 6a**). The characteristics spectra of the pure dox were recorded to have peaks at 592 and 670 nm. The spectral characteristics of dox were then uploaded and stored in the spectral library, and they were recalled and pseudo-colored during experimental cell analysis. The intensity in each pixel of the spectral was compared among the background (negative control) and different concentrations of dox (**Supp Fig. 6b**; see “**Materials and methods**”). Importantly, we were able to identify and quantify the amount and location of dox within single cells at a lower concentration. Please note that while we treated the cells with 1 nM

of dox, this did not imply that 1 nM of dox was detected inside the cells. This was discussed below. The intensity variations of the dox wavelengths were quantified for each dox concentration (**Supp Fig. 6c**). The spectra intensity was increased as higher concentrations of dox were used. Interestingly, we also observed a potential peak at 520 nm in the cells treated with a higher dose of dox. Because this peak was not observed in cell-free system, we hypothesized that 520 nm might represent a metabolite peak of dox.

Dox is known to be metabolized to dox'ol (Schaupp et al., 2015), (Boucek et al., 1987), (X. Wang et al., 2019). To investigate if the 520 nm peak was dox'ol, we scanned the wavelengths of dox'ol only, different concentrations of dox'ol, and dox/dox'ol mixture (**Fig. 3-3a**). We could confirm that the spectral peak of the dox'ol was at 520 nm (**Fig. 3-3b**). The spectral characteristics of dox'ol were uploaded and stored in the spectral library, and they were recalled and pseudo-colored in the other separate images for further analyses. In addition, the background spectra with or without the cells were recorded to distinguish spectral intensity at 520 nm peak. The intensity variations of the dox'ol wavelengths were next quantified for each dox'ol concentration (**Fig. 3-3c**). Cells treated with different concentrations of dox'ol showed the location of dox'ol within the cell samples, which was concentrated mainly in the nucleoplasm area. Hence, we confirmed for the first time the ability of spectral microscopy system to track and identify a high image resolution of parental drug dox and its metabolite dox'ol in single cells.

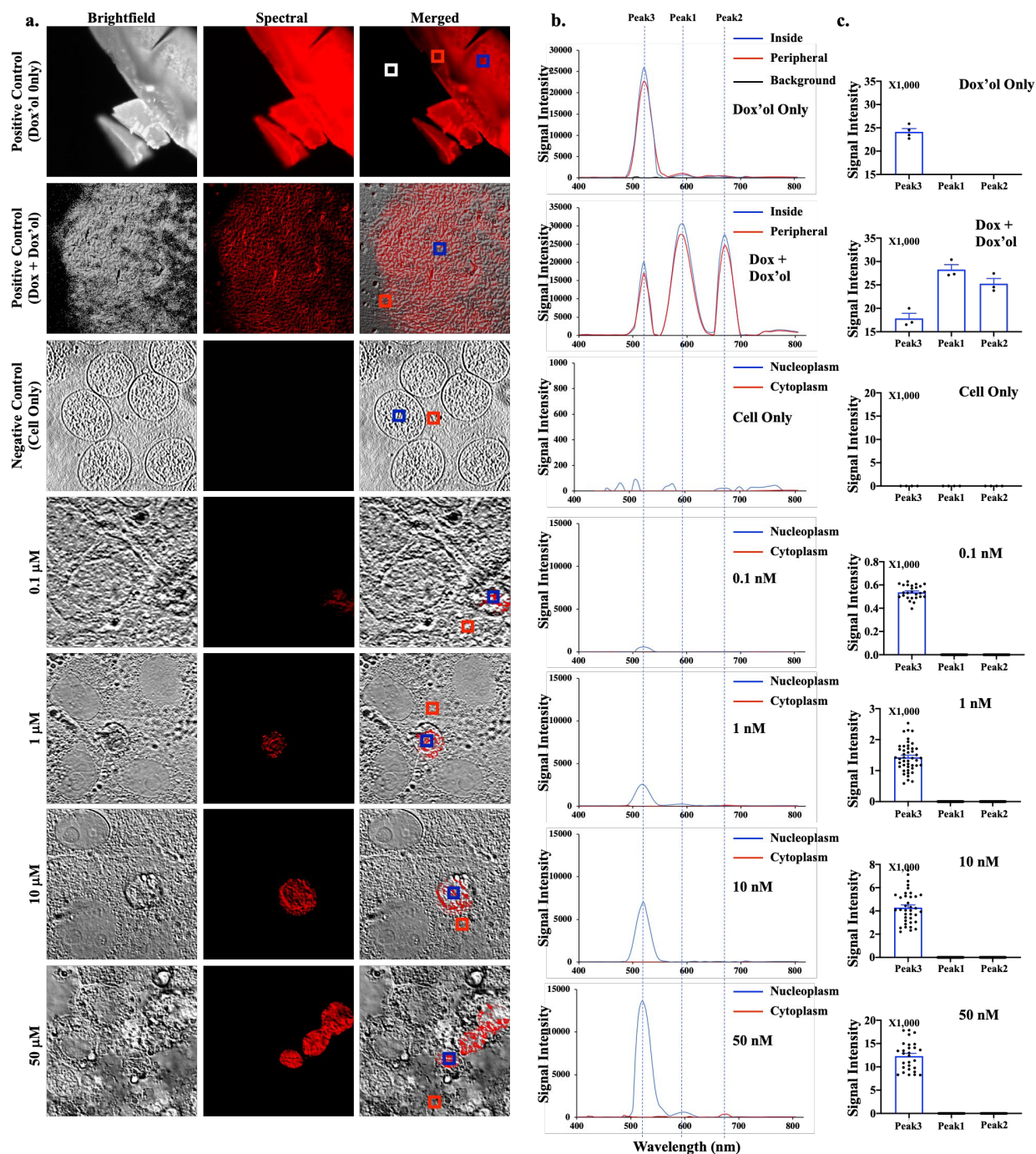


Figure 3-3: Spectral Imaging on dox'ol.

(a) Brightfield, emission spectral and merged images of dox'ol-only (dissolved dox'ol as a positive control), 2:3 of dox'ol:dox (positive control), non-treated cells (negative control), and 18-h dox'ol-treated cells at various concentrations. Cells were then fixed and imaged. White box = background; red box = lower signal intensity of dox'ol; blue box = higher signal intensity for dox'ol. (b) The graphs show the spectra characteristics of dox'ol, showing peak at 520 nm (Peak3). Dox is shown with peaks at 592 nm (Peak1) and 670 nm (Peak2). (c) The bar graphs exhibit the variations of the intensity data points for Peaks1, 2, and/or 3. $N = 3$ (control groups) and $N \geq 20$ (treatment groups). Scale Bar = 10 μm .

The spectral microscopy had a linearity for quantification purposes

We evaluated if the spectral microscopy system could have the linearity to quantify rhodamine (**Supp Fig. 7**), dox (**Supp Fig. 8**) and dox'ol (**Fig. 3-4**). Our approach included analyses of each peak individually (Peak 1 and Peak 2) and potential interaction between peaks (Peak1/Peak2). For rhodamine, we analyzed the linearity with (**Supp Fig. 7a**) and without (**Supp Fig. 7b**) the over-saturated point. Note that the saturated point in our spectral microscopy system was used to confirm rhodamine using the standard fluorescence microscope. The first major peak of rhodamine at 580 nm represented the linearity of spectral intensity that we could use for quantitation purposes for rhodamine. On the other hand, the linearity for dox was confirmed to be the major peak of 592 nm (**Supp Fig. 8a**). Because dox is associated to induce cell apoptosis (S. Wang et al., 2004), we took this opportunity to quantify cells with abnormal nucleus and/or smaller cell morphology (**Supp Fig. 8b**). Our data confirmed that we were using dox compound having activity at a very low concentration of nM. Because dox'ol showed only one peak at 520, we proceeded to analyze this peak (**Fig. 3-4**). The linearity of spectral intensity of dox'ol peaks from the spectral microscopy was confirmed at 520 nm. Our analyses indicated that the spectral microscopy system had potential capability for quantification.

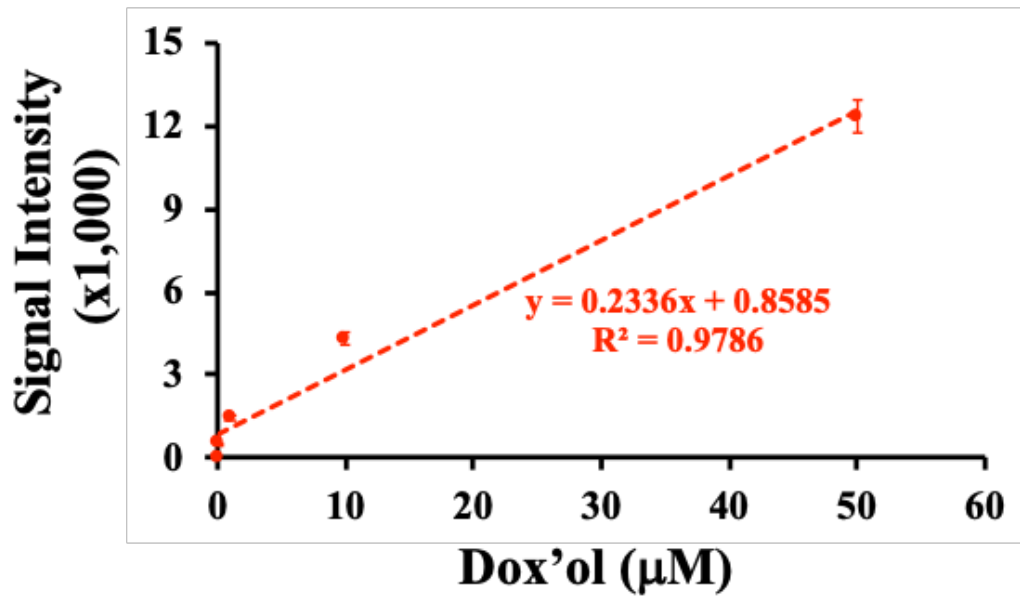


Figure 3-4: Analysis of linearity of dox'ol in spectral imaging

Linear regression analysis for the cells treated with dox'ol by spectral imaging. The graph illustrates the average intensities of the peak (520 nm). N = 3

The spectral microscopy could quantify the kinetic changes of intracellular levels of dox and dox'ol.

To understand pharmacokinetics of dox, we first performed a time-lapse study (**Fig. 3-5**) and analyzed the changes in spectral intensity for 0.01 nM of rhodamine (**Supp Figs. 9, 10**). Again, rhodamine was used as a control, because we could confirm its fluorescence easily using regular fluorescence microscope. There were increases in the amount of rhodamine with time in the cytoplasm area as depicted in the intensity increase. In the spectral microscopy system, the increase in the wavelength intensity included the peak at 515 nm, which was suspected to be rhodamine metabolite.

For quantitation purposes, we used our prior studies using the traditional LC/MS method for dox. For dox'ol, the linearity was found with the precursor ion at m/z 546 Da (**Fig. 3-7a**), consistent with a previous study (Schaupp et al., 2015). We could differentiate two precursor ions (peaks) at m/z 544 Da (dox) and 546 Da (dox'ol) in cell-free system as another verification of our LC/MS (**Fig. 3-7b**) and cell lysate as a correlation for our pharmacokinetic studies for dox (**Fig. 3-7c,d**). The intracellular distribution of dox was calculated from LC/MS to be $3.93 \pm 0.32 \mu\text{M}/\text{min}/\text{mg}$ of total protein with the K_m of enzyme kinetics of $0.19 \pm 0.02 \mu\text{M}/\text{mg}$ of protein.

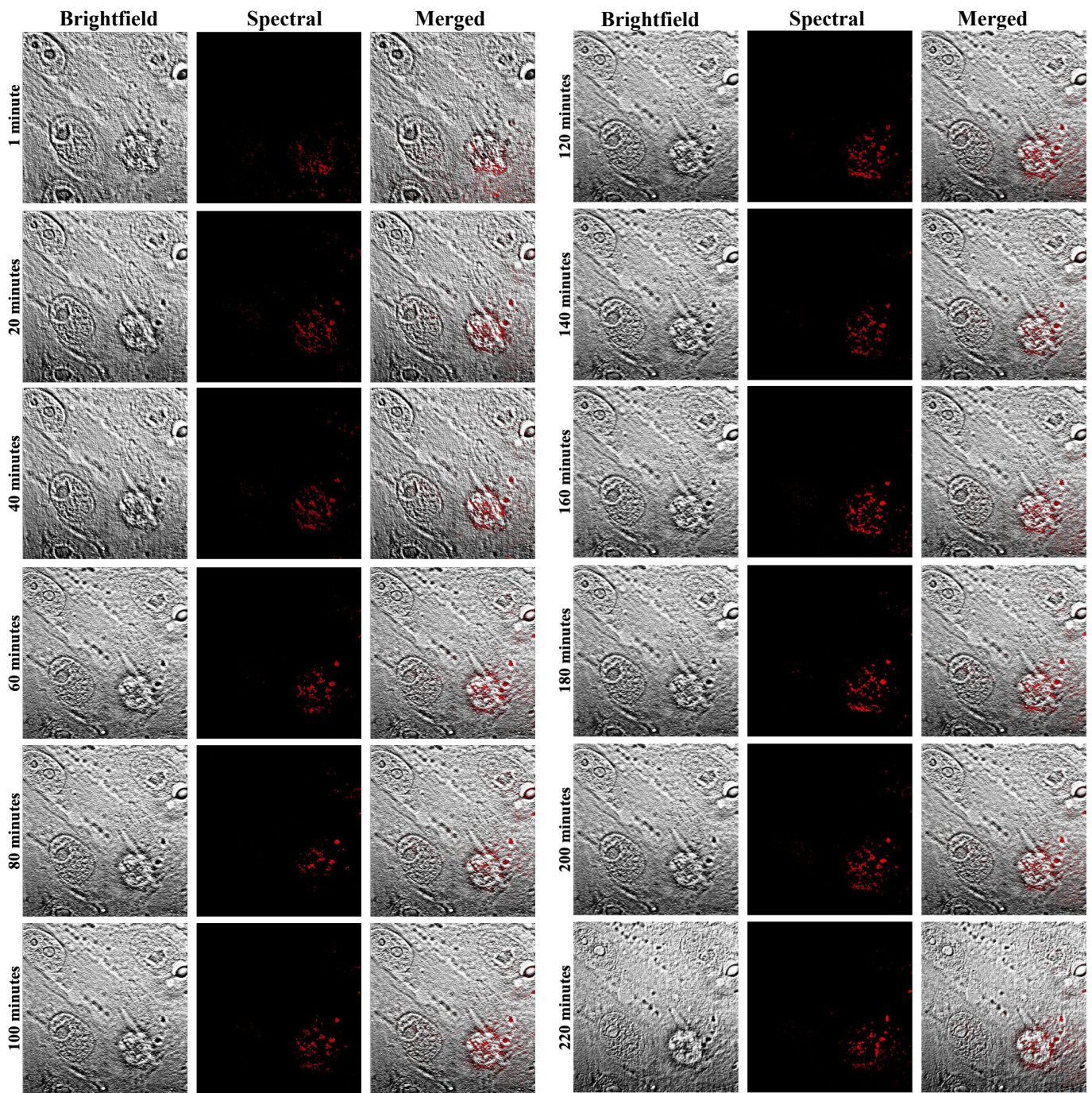
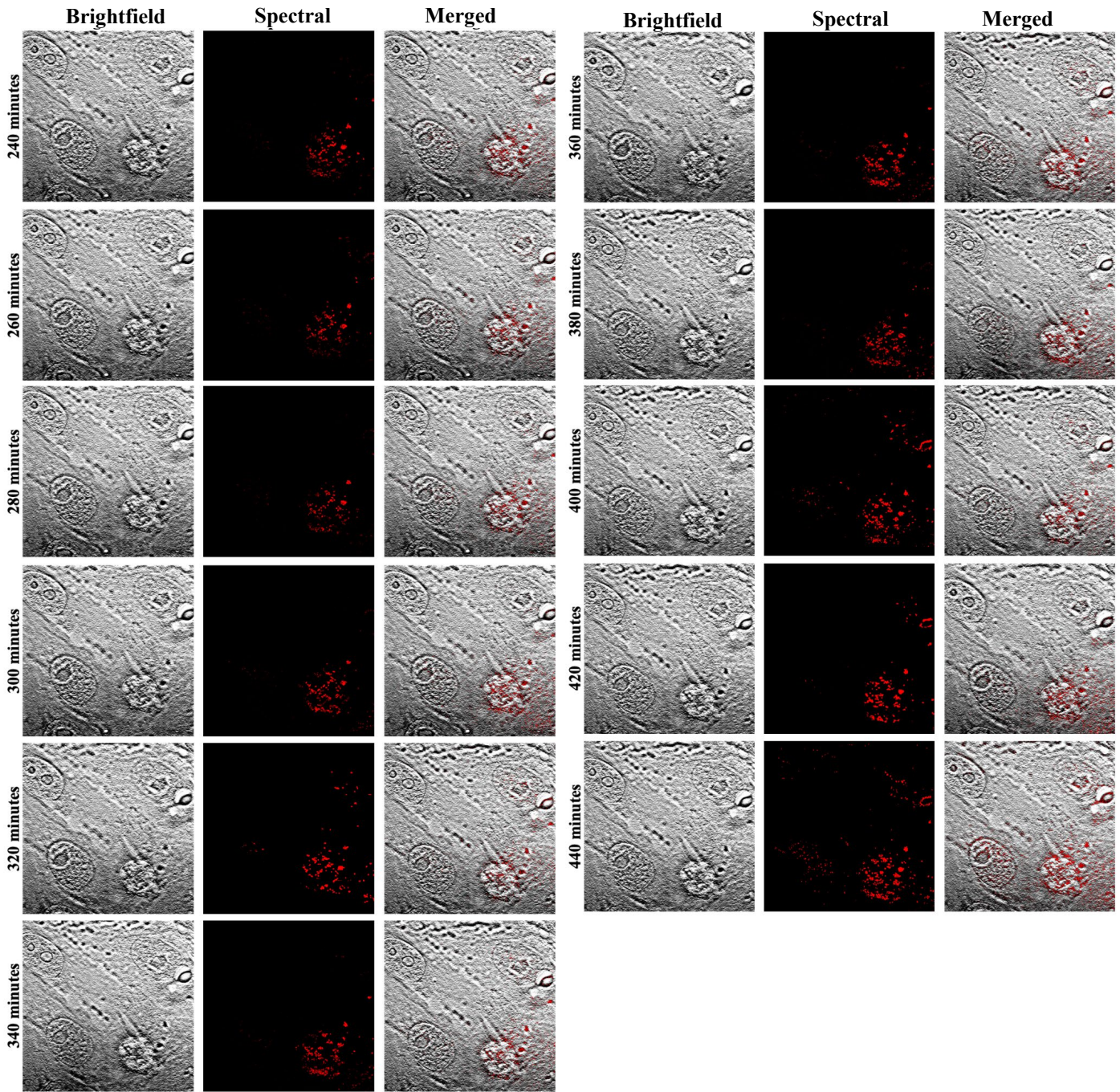


Figure 3-5: Time-lapse Imaging for The Cells That Treated With 1 nM Dox. Images were captured every 20 minutes for 440 minutes. Dox accumulated in the nucleus area more than in the cytoplasm.



Continue Figure 3-5

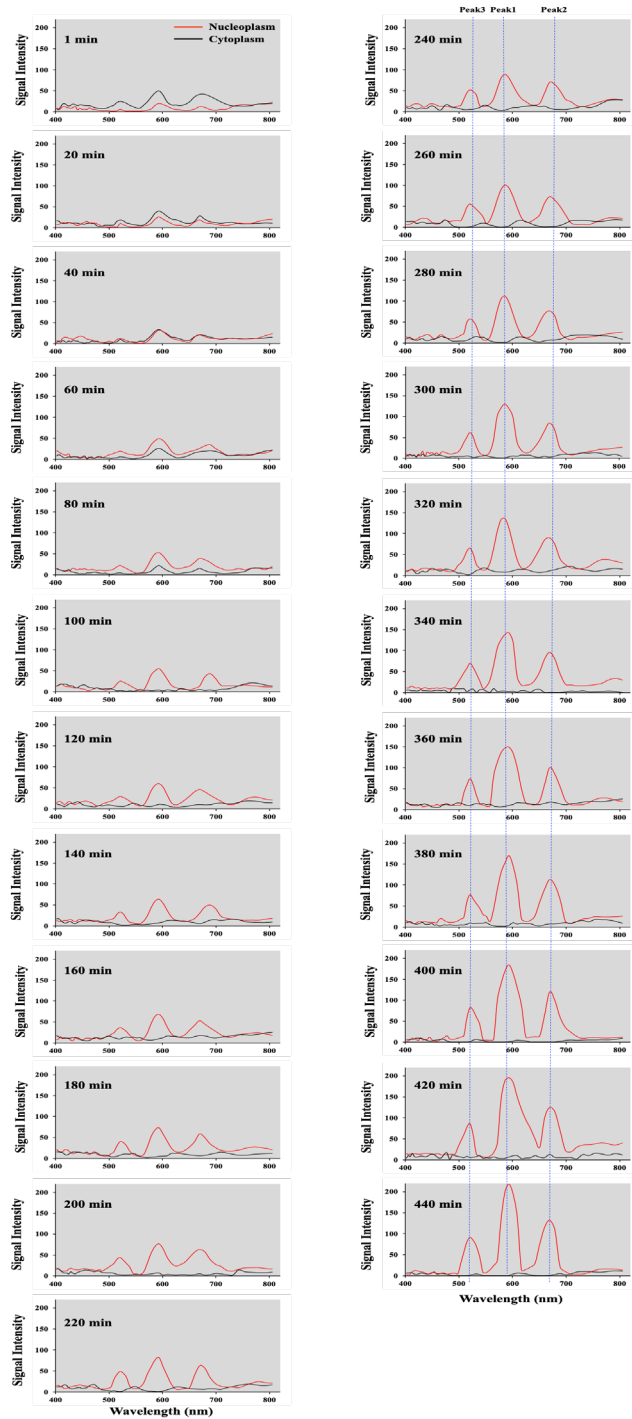


Figure 3-6: Line Graphs Represent Dox Wavelengths at Different Time Points.

The wavelength intensity increases over time. The red line represents the cytoplasm area, while black shows the background region, which is in the nucleoplasm. At the beginning of tracking, dox found in the cytoplasm area, but it then moved to the nucleoplasm area completely.

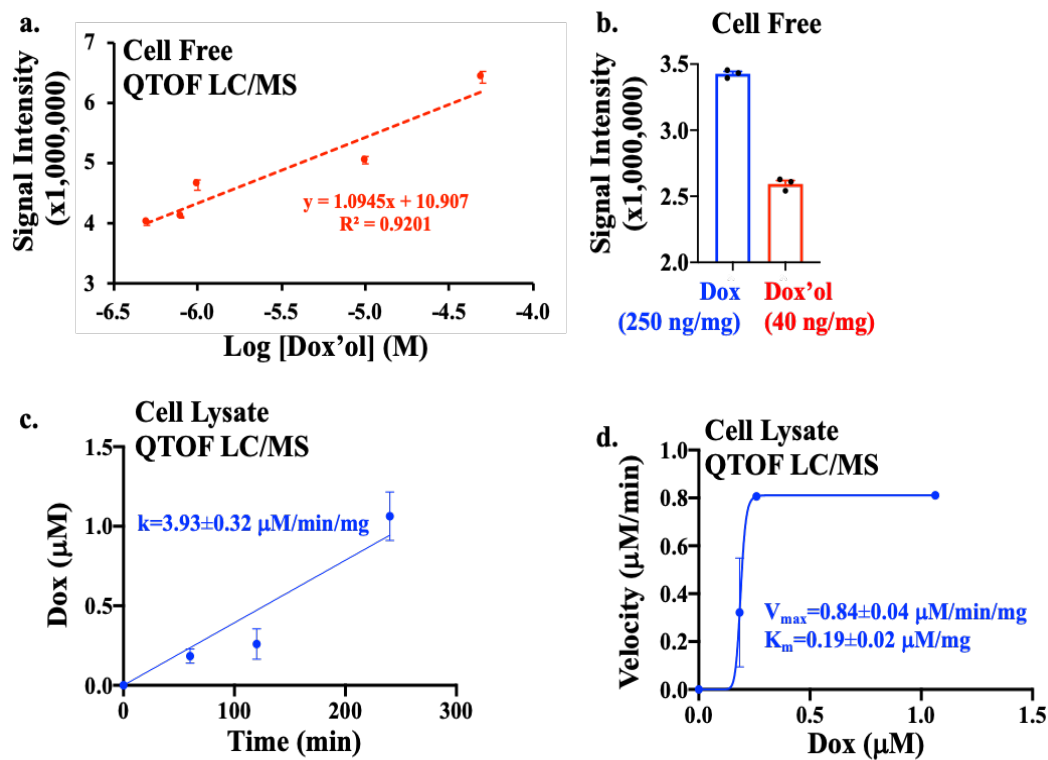


Figure 3-7: Linear Regression Analysis of Dox'ol Cell-free & Dox Cell Lysate

(a) Linear regression analysis of dox'ol-only in the cell-free system was performed from QTOF-LC/MS data. The linearity of dox'ol was detected at the precursor ion m/z 546 Da. (b) The bar graph shows a pure mixture of dox and a dox'ol in cell-free system by Q-TOF LC/MS. (c) Cells treated with 2 μM dox were collected at different time points and analyzed for dox (m/z 544 Da). Dox influx into the cells was calculated. (d) Cells treated with 2 μM dox were collected at different time points and analyzed for dox'ol (m/z 544 Da). Enzyme kinetics (V_{max} and K_m) were calculated based on the linear influx of dox. $N=3$.

The time-lapse of dox was next performed in single cells for about 7 h (**Supp Fig. 3-5**). Quantitative analysis of the spectral intensity of 1 nM dox indicated that dox was first accumulated in the cytoplasm in the first hour (**Figs. 3-6, 3-8**). Subsequently, a higher accumulation of dox was detected in the nucleoplasm (**Fig. 3-9a**). Of interest was the metabolite peak at 520 nm, which slowly and steadily increased (**Fig. 3-9b**). Given that dox (**Supp Fig. 6**) and dox'ol (**Fig. 3-3**) were represented by the respective spectra peaks of 592 and 520 nm, we calculated the rate constants of dox and dox'ol distributions in the cells and kinetic conversion of dox to dox'ol (**Fig. 3-9c**). The rate of dox accumulation in the cytoplasm was $1.49 \pm 0.04 \text{ pM min}^{-1}$. In the cytosol, dox was converted to dox'ol with enzymatic characteristics of V_{\max} at $0.24 \pm 0.01 \text{ pM min}^{-1}$ and K_m at $25.14 \pm 2.14 \text{ pM}$. Both dox and dox'ol were then distributed to the nucleus with rate constants of $0.84 \pm 0.02 \text{ pM min}^{-1}$ and $0.28 \pm 0.01 \text{ pM min}^{-1}$, respectively.

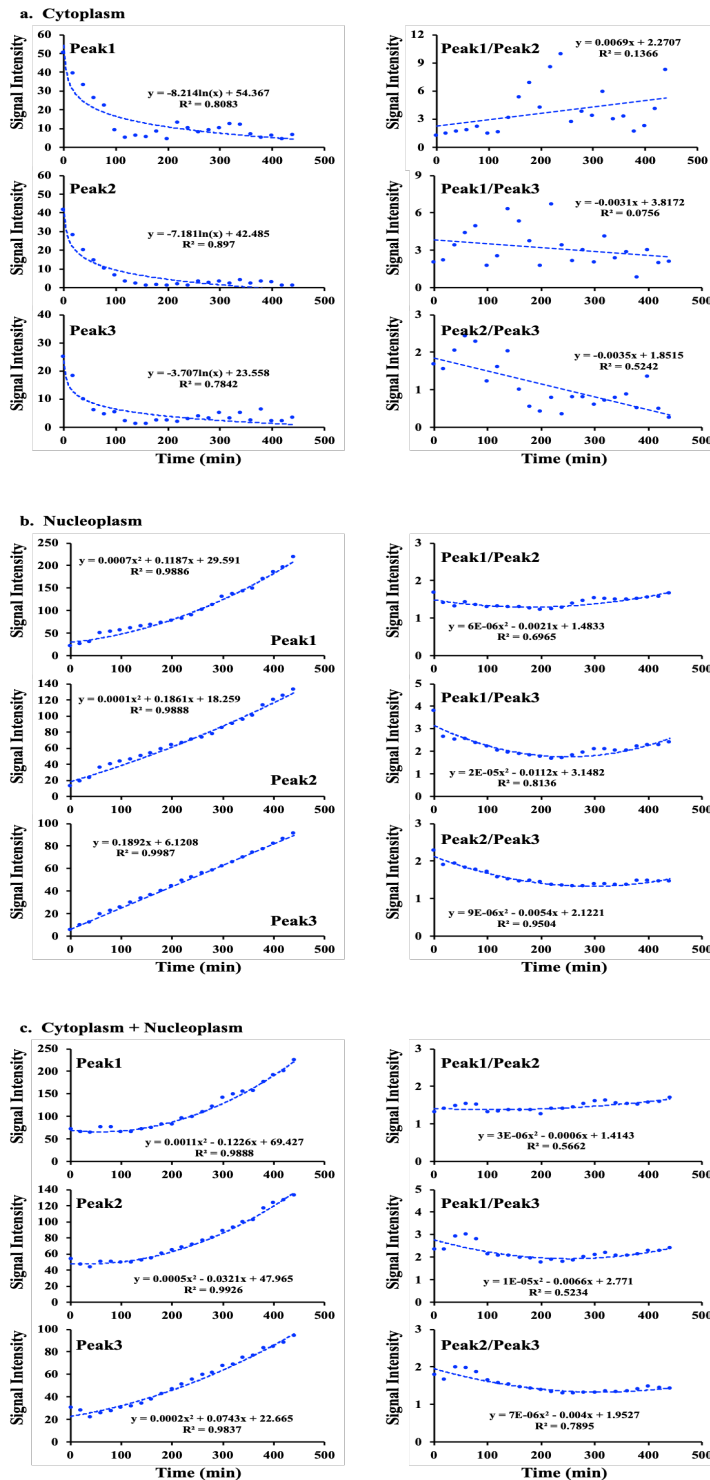


Figure 3-8: Curve-fit Analyses of Time-lapse Imaging for The Cells Treated With Dox

In cytoplasm (a), nucleoplasm (b) and entire cell (c). The left panels show the analyses of time-lapse imaging data points for the cells treated with rhodamine for Peak1 (592 nm), Peak2 (670 nm) and Peak3 (520 nm). The right panels represent the ratios of different peaks.

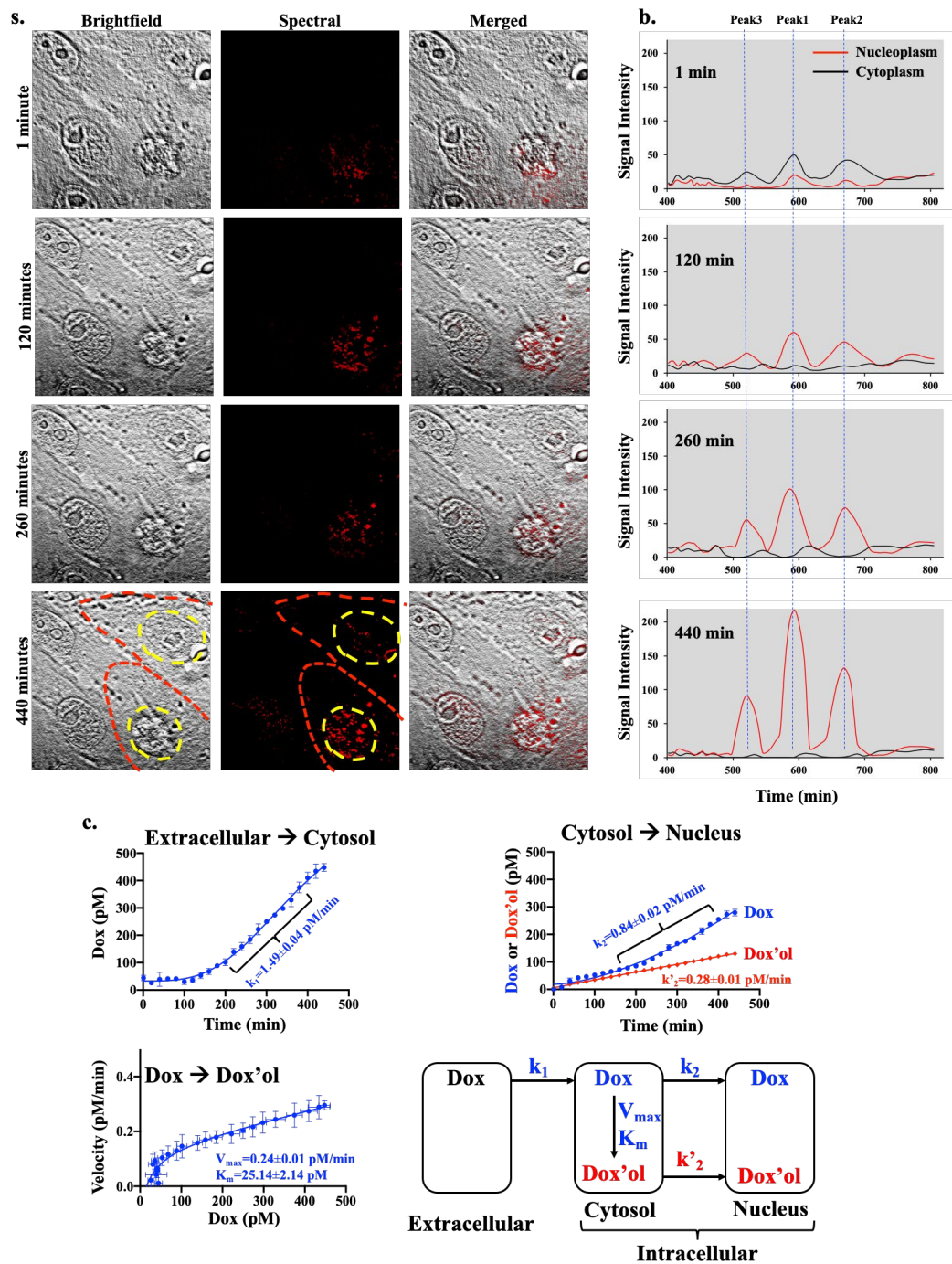


Figure 3-9: Metabolism of dox to dox'ol in Single Living Cells

(a) The time-lapse of brightfield, spectral and merged images are shown for cells treated with 1 nM dox for 440 minutes with red-line (cell border) and yellow-line (nucleus border). (b) The graphs depict the spectra intensity of peaks at 592 nm (Peak1; dox), 670 nm (Peak2) and 520 nm (Peak3; dox'ol). (c) The rate constants of dox influx into a cell (k_1) and nucleus (k_2) were calculated. The rate constant of dox'ol influx into a nucleus (k'_2) was greater than k_2 . The enzyme kinetics of dox metabolism was calculated for their maximum velocity (V_{max}) and Michaelis constant of dox affinity (K_m). A 3-compartment model for dox metabolism is illustrated. $N=4$.

3.5 Discussion

Because evaluation of drug and its metabolite is an essential process to understand drug activity, stability, toxicity and distribution during drug development (Deshaies, 2020), we compared the use of our novel technique to LC/MS, which is the standard analytical tool for screening and identifying drug metabolites (Rubakhin et al., 2011). Without labeling the drug and destroying the samples, we here demonstrated that spectral microscopy could allow us to analyze rates of drug metabolism and subcellular distribution. The significance of this method in drug discoveries is multiple. First, dox'ol is believed to contribute significantly to cardiotoxicity in cancer patients (Schaupp et al., 2015). Because dox is still used as chemotherapy regimens, further investigation of dox metabolism is warranted. Second, the cardiotoxicity of dox'ol is more complicated than once thought. It is generally thought that dox'ol interferes with cardiac contraction primarily by inhibiting membrane-associated ion channel (Boucek et al., 1987). Our data showed that the long-term effect of dox'ol in the cell nucleus, which was previously unknown, could not be ignored.

Using a standard LC/MS approach, the intracellular distribution of dox was calculated to be $3.93 \pm 0.32 \text{ Mm min}^{-1} \text{ mg}^{-1}$ of total protein (**Fig. 3-7**). To put this value into perspective from the spectral microscopy approach, we would need to assume that one mammalian cell has about 250 pg proteins (Cheung et al., 2013). This assumption would result in a rate constant of $\sim 1.5 \text{ pM min}^{-1} \cdot 1.5 \text{ cell}^{-1}$, compared to the microscopy approach of $\sim 1.5 \text{ pM min}^{-1} \text{ cell}^{-1}$ (**Fig. 3-9**). Using QTOF-LC/MS, we calculated the K_m of enzyme kinetics was $0.19 \pm 0.02 \text{ } \mu\text{M mg}^{-1}$ of protein (**Fig. 3-7**). With the same assumption of 250 pg protein/cell, the K_m was converted to about $\sim 25 \text{ pM}$ per 100 cells by the traditional approach compared to spectral microscopy of $\sim 25 \text{ pM}$ per one cell (**Fig. 3-9**).

Comparing the discrepancy ratios between 1:1.5 cells for distribution rate constant and 1:500 cells for enzyme kinetic K_m , we postulated that most of dox'ol metabolite were tightly bound to the DNA in the nucleus. As a result, the metabolism rate of dox to dox'ol might have been underestimated by 1 to 500 cells due to subcellular localization of dox'ol in the nucleus. During isolation from the cell lysate, the incomplete separation of nuclear dox/dox'ol could contribute to underestimation for the dox'ol formation by ~500 cells. It is important to note that the discrepancy did not imply that spectral microscopy provided more accuracies to calculate the respective distribution rate and enzyme kinetics. The reason was that both LC/MS and microscopy approaches were not equally comparable to one another. The spectral microscopy might provide a better resolution of drug disposition and metabolism at a single cell-resolution. On the other hand, LC/MS would provide a more robust analysis at an organ system level.

The spectral microscopy uses a combination of high-resolution imaging and spectroscopy techniques. This is a valuable approach that is currently under-utilized to study valuable biological and clinical samples. The advantages of the spectral microscopy include the following. First, it is not labor-intensive and time consuming for sample preparation to perform quantitative bioanalysis, compared to other methods. Second, there is no concern about matrix interfering with the drugs. Using a standard HPLC approach, matrix proteins, lipids or salts need to be removed either to prevent the column from clogging or to improve HPLC reliability, sensitivity and selectivity in the analysis. Third, the spectral microscopy approach requires no additional treatment to samples. In traditional fluorescence imaging, samples are to be tagged, treated or radio-labelled to increase the reliability of sample detection. The detection of drug and its metabolite becomes unlikely. Fourth, the high-resolution imaging provides spatial and temporal information of a drug and its metabolite. In contrast, a combination with spectroscopy gives valuable information of the drug metabolism

for each pixel of the image. The disadvantage of the spectral microscopy is that unlike regular imaging which is relatively more straightforward, it involves changing the optical pass differences to collect the essential information for the entire image. In addition, the spectral microscopy for the use of quantitation will still depend on LC/MS to help calibrate the linearity of the spectral signal.

3.6 Conclusion

Without labeling drugs and destroying the samples, SI is a novel method that allows us to analyze the dynamics of drug distribution and metabolism in single living cells (**Supp Fig. 12**). The spectral microscopy provides a high image resolution to track and identify dox and its metabolite dox'ol. The microscopy approach confirms that both dox and dox'ol are translocated to the nucleus at different rates, while rhodamine remains in cytoplasm. The use of novel spectral microscopy approach on dox, dox'ol and rhodamine is for the first time validated with a traditional approach of LC/MS.

References

- Agudelo, D., Bourassa, P., Bérubé, G., & Tajmir-Riahi, H.-A. (2014). Intercalation of antitumor drug doxorubicin and its analogue by DNA duplex: Structural features and biological implications. *International Journal of Biological Macromolecules*, *66*, 144–150. <https://doi.org/10.1016/j.ijbiomac.2014.02.028>
- Boucek, R. J., Olson, R. D., Brenner, D. E., Ogunbunmi, E. M., Inui, M., & Fleischer, S. (1987). The major metabolite of doxorubicin is a potent inhibitor of membrane-associated ion pumps. A correlative study of cardiac muscle with isolated membrane fractions. *The Journal of Biological Chemistry*, *262*(33), 15851–15856.
- Cheung, M. C., LaCroix, R., McKenna, B. K., Liu, L., Winkelman, J., & Ehrlich, D. J. (2013). Intracellular protein and nucleic acid measured in eight cell types using deep-ultraviolet mass mapping. *Cytometry. Part A: The Journal of the International Society for Analytical Cytology*, *83*(6), 540–551. <https://doi.org/10.1002/cyto.a.22277>
- Damiani, R. M., Moura, D. J., Viau, C. M., Caceres, R. A., Henriques, J. A. P., & Saffi, J. (2016). Pathways of cardiac toxicity: Comparison between chemotherapeutic drugs doxorubicin and mitoxantrone. *Archives of Toxicology*, *90*(9), 2063–2076. <https://doi.org/10.1007/s00204-016-1759-y>
- Deshaies, R. J. (2020). Multispecific drugs herald a new era of biopharmaceutical innovation. *Nature*, *580*(7803), 329–338. <https://doi.org/10.1038/s41586-020-2168-1>
- Dolloff, N. G., Ma, X., Dicker, D. T., Humphreys, R. C., Li, L. Z., & El-Deiry, W. S. (2011). Spectral imaging-based methods for quantifying autophagy and apoptosis. *Cancer Biology & Therapy*, *12*(4), 349–356. <https://doi.org/10.4161/cbt.12.4.17175>

- Feng, W., Zhang, C., Yu, T., Semyachkina-Glushkovskaya, O., & Zhu, D. (2019). In vivo monitoring blood-brain barrier permeability using spectral imaging through optical clearing skull window. *Journal of Biophotonics*, *12*(4), e201800330. <https://doi.org/10.1002/jbio.201800330>
- Garini, Y., Young, I. T., & McNamara, G. (2006). Spectral imaging: Principles and applications. *Cytometry. Part A: The Journal of the International Society for Analytical Cytology*, *69*(8), 735–747. <https://doi.org/10.1002/cyto.a.20311>
- Li, Q., He, X., Wang, Y., Liu, H., Xu, D., & Guo, F. (2013). Review of spectral imaging technology in biomedical engineering: Achievements and challenges. *Journal of Biomedical Optics*, *18*(10), 100901. <https://doi.org/10.1117/1.JBO.18.10.100901>
- Liu, X., & Jia, L. (2007). The conduct of drug metabolism studies considered good practice (I): Analytical systems and in vivo studies. *Current Drug Metabolism*, *8*(8), 815–821. <https://doi.org/10.2174/138920007782798153>
- Mayes, P., Dicker, D., Liu, Y., & El-Deiry, W. (2008). Noninvasive vascular imaging in fluorescent tumors using multispectral unmixing. *BioTechniques*, *45*(4), 459–460, 461–464. <https://doi.org/10.2144/000112946>
- Minotti, G., Menna, P., Salvatorelli, E., Cairo, G., & Gianni, L. (2004). Anthracyclines: Molecular advances and pharmacologic developments in antitumor activity and cardiotoxicity. *Pharmacological Reviews*, *56*(2), 185–229. <https://doi.org/10.1124/pr.56.2.6>
- Rubakhin, S. S., Romanova, E. V., Nemes, P., & Sweedler, J. V. (2011). Profiling metabolites and peptides in single cells. *Nature Methods*, *8*(4 Suppl), S20–29. <https://doi.org/10.1038/nmeth.1549>

- Saar, B. G., Contreras-Rojas, L. R., Xie, X. S., & Guy, R. H. (2011). Imaging drug delivery to skin with stimulated Raman scattering microscopy. *Molecular Pharmaceutics*, 8(3), 969–975. <https://doi.org/10.1021/mp200122w>
- Salvatorelli, E., Menna, P., Chello, M., Covino, E., & Minotti, G. (2017). Modeling Human Myocardium Exposure to Doxorubicin Defines the Risk of Heart Failure from Low-Dose Doxorubicin. *The Journal of Pharmacology and Experimental Therapeutics*, 362(2), 263–270. <https://doi.org/10.1124/jpet.117.242388>
- Schaupp, C. M., White, C. C., Merrill, G. F., & Kavanagh, T. J. (2015). Metabolism of doxorubicin to the cardiotoxic metabolite doxorubicinol is increased in a mouse model of chronic glutathione deficiency: A potential role for carbonyl reductase 3. *Chemico-Biological Interactions*, 234, 154–161. <https://doi.org/10.1016/j.cbi.2014.11.010>
- Tenuta, T., Monopoli, M. P., Kim, J., Salvati, A., Dawson, K. A., Sandin, P., & Lynch, I. (2011a). Elution of labile fluorescent dye from nanoparticles during biological use. *PloS One*, 6(10), e25556. <https://doi.org/10.1371/journal.pone.0025556>
- Tomatis, S., Carrara, M., Bono, A., Bartoli, C., Lualdi, M., Tragni, G., Colombo, A., & Marchesini, R. (2005). Automated melanoma detection with a novel multispectral imaging system: Results of a prospective study. *Physics in Medicine and Biology*, 50(8), 1675–1687. <https://doi.org/10.1088/0031-9155/50/8/004>
- Tumeh, P. C., Lerner, J. M., Dicker, D. T., & El-Deiry, W. S. (2007). Differentiation of vascular and non-vascular skin spectral signatures using in vivo hyperspectral radiometric imaging: Implications for monitoring angiogenesis. *Cancer Biology & Therapy*, 6(3), 447–453. <https://doi.org/10.4161/cbt.6.3.4019>

- Wang, S., Konorev, E. A., Kotamraju, S., Joseph, J., Kalivendi, S., & Kalyanaraman, B. (2004). Doxorubicin induces apoptosis in normal and tumor cells via distinctly different mechanisms. Intermediacy of H(2)O(2)- and p53-dependent pathways. *The Journal of Biological Chemistry*, 279(24), 25535–25543. <https://doi.org/10.1074/jbc.M400944200>
- Wang, X., Hui, R., Chen, Y., Wang, W., Chen, Y., Gong, X., & Jin, J. (2019). Discovery of Novel Doxorubicin Metabolites in MCF7 Doxorubicin-Resistant Cells. *Frontiers in Pharmacology*, 10, 1434. <https://doi.org/10.3389/fphar.2019.01434>
- Zeng, X., Cai, H., Yang, J., Qiu, H., Cheng, Y., & Liu, M. (2019). Pharmacokinetics and cardiotoxicity of doxorubicin and its secondary alcohol metabolite in rats. *Biomedicine & Pharmacotherapy = Biomedecine & Pharmacotherapie*, 116, 108964. <https://doi.org/10.1016/j.biopha.2019.108964>
- Zhang, Z., Zhu, M., & Tang, W. (2009). Metabolite identification and profiling in drug design: Current practice and future directions. *Current Pharmaceutical Design*, 15(19), 2220–2235. <https://doi.org/10.2174/138161209788682460>

Chapter 4: Summary

In the biomedical research, there is a necessity for an easy and inexpensive system to study drugs at the levels of cells and tissues. Among inorganic molecules such as NPs, inductively coupled plasma mass spectrometry (ICP-MS) and inductively-coupled plasma atomic emission spectroscopy (ICP-AES) are conventional methods used for the quantification of the NPs. Besides matrix interference, chemical involvement, the requirement of a liquid sample, plasma sensitivity to organic solvents are all disadvantages of ICP linked procedures. While fluorescent-conjugated NPs are commonly used to detect NP localization in live biological samples, they may interfere with NP function, localization, cytotoxicity, and biodistribution. However, the combination of imaging and spectroscopy in SI provides high-resolution spatial and temporal information of spectra characteristics in each pixel. Here, we were able to use SI to identify and quantify the presence of NPs without the need to destruct or liquify the samples. This allowed us to conduct live-cell imaging, which would not have been possible otherwise. We could calibrate the spectra library by combining imaging and the singularity/plurality of a chemical's spectra "signature." We could pick up various spectra at 420 nm in Ag(s)-NPs, for example, peak with or without a shoulder. We discovered that peaks without a shoulder were always found in the core of NPs, whereas peaks with a shoulder were found on the periphery. Also, we didn't need to use fluorescent to mark our NPs. Labeling NPs necessitated an extra step in the synthesis process, making it more expensive and time-consuming. We were able to examine the dynamic uptake, mobility, and distribution of several types of free-labeled NPs in single cells using SI.

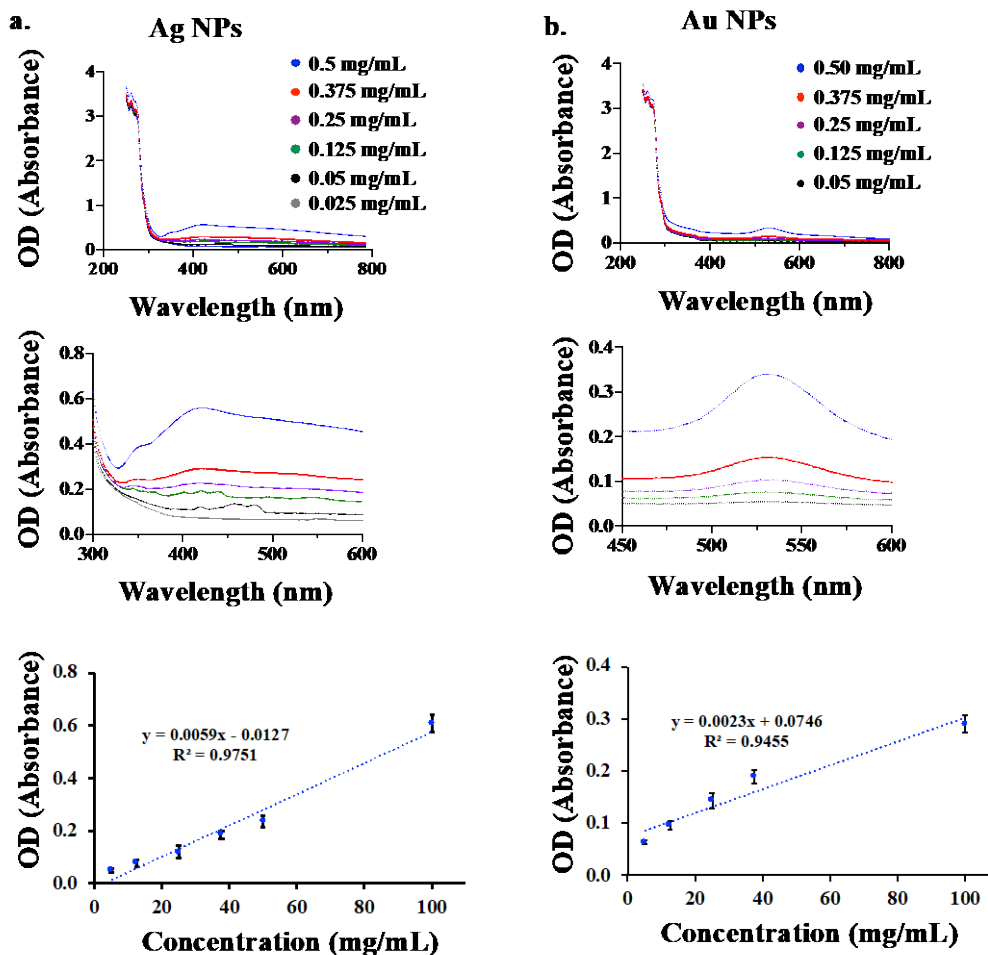
We were able to trigger the behaviors of the NPs in single cells using a live imaging approach that scanned spectra, and we found that NPs eventually accumulated in the cell nucleus. Among tissues,

Ag(s)-NPs and Ag-NPs were identified largely in the kidney and spleen, respectively. Au-NPs, on the other hand, were found distributed largely in the liver. Furthermore, among organic molecules, we discovered for the first time that SI is a revolutionary tool for analyzing the kinetics of drug distribution and metabolism in single living cells without tagging the drug or damaging the samples. The dox metabolite, dox'ol, is tracked and identified using spectral microscopy, which has a high image resolution. According to the microscopy method, both dox and dox'ol are translocated to the nucleus at varying rates, whereas rhodamine stays in the cytoplasm.

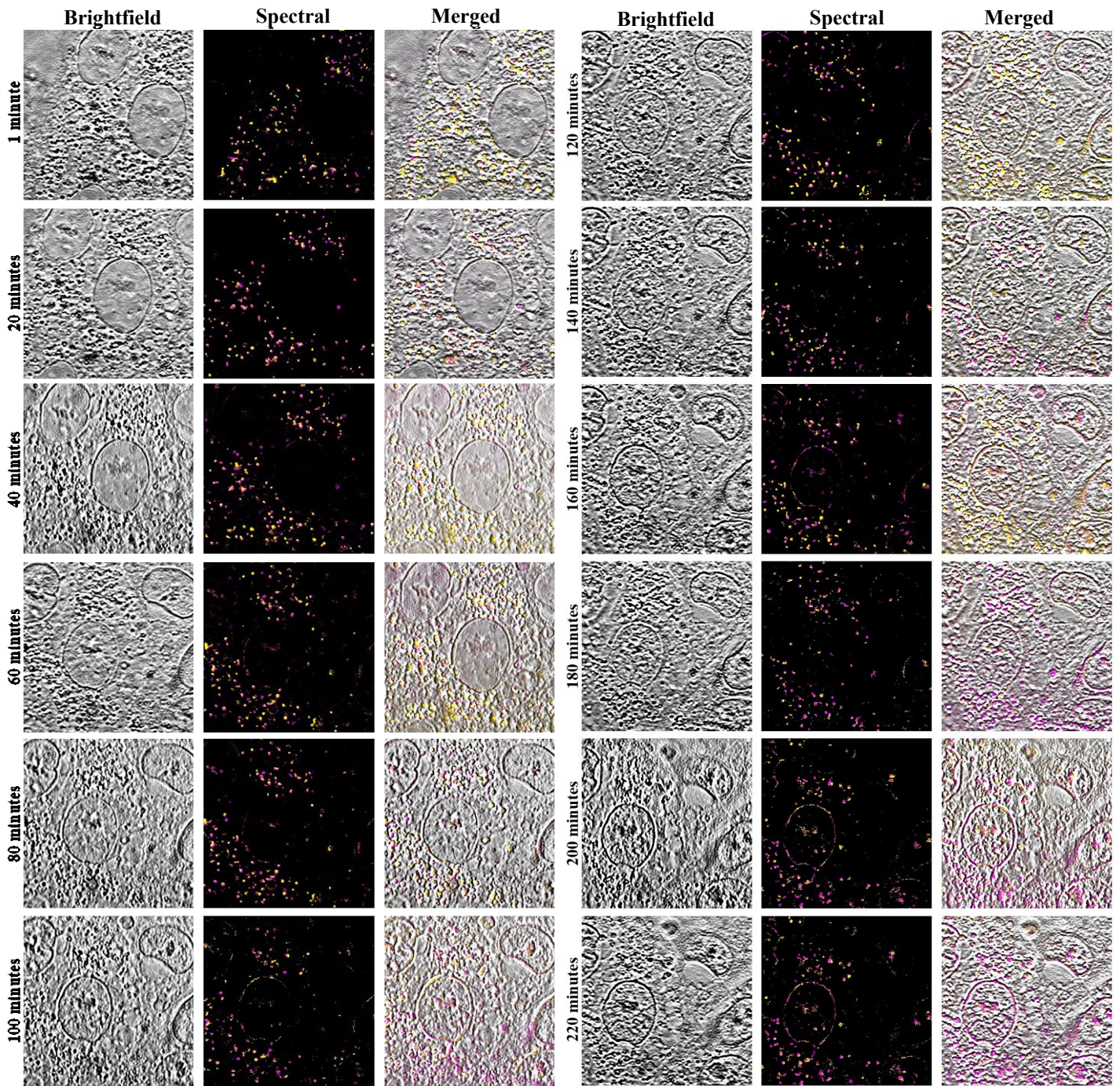
Future Directions:

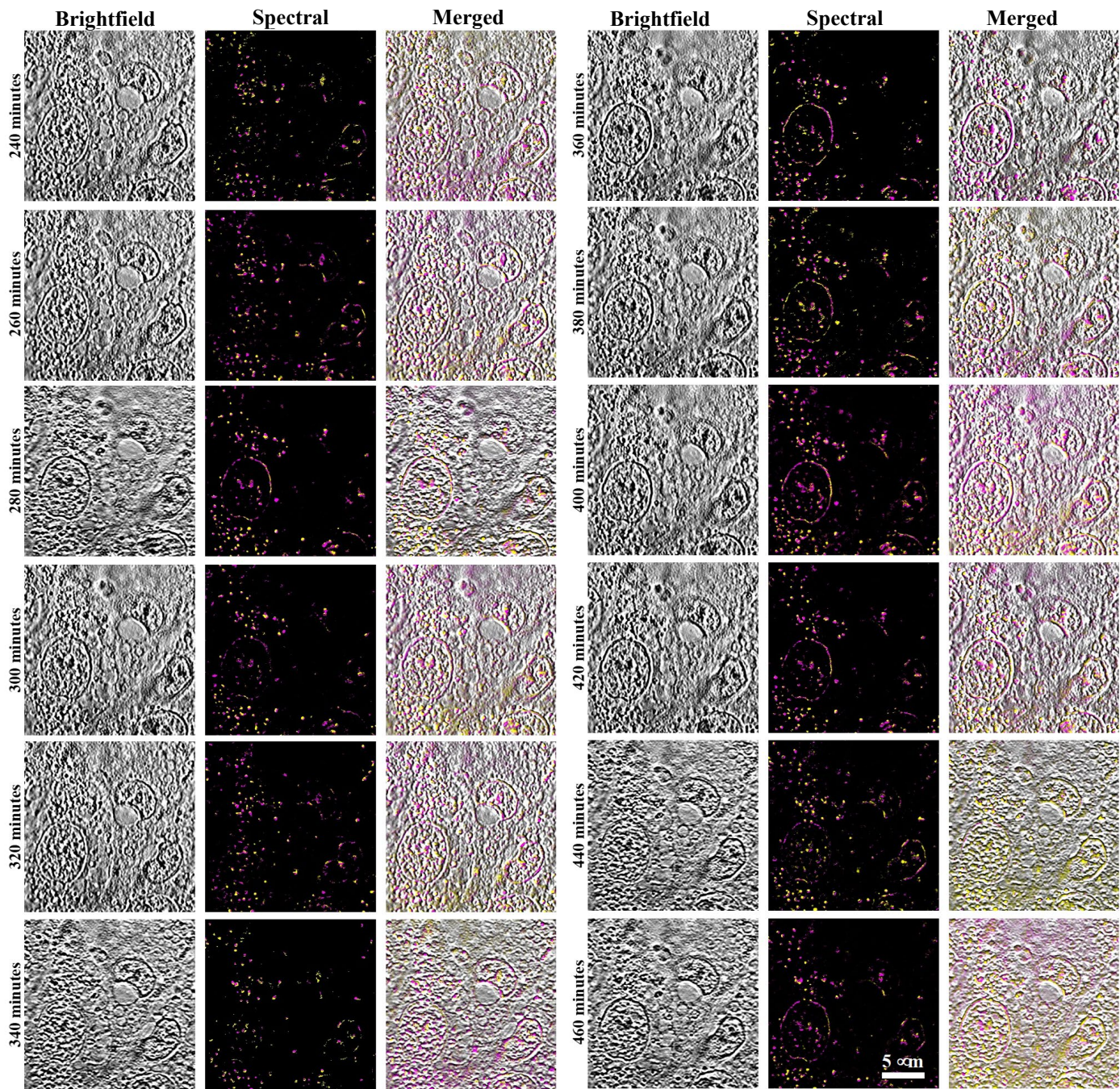
We have revealed that SI could serve as a valuable technique to understand the distribution, dynamic movement, and behavior of drugs and NPs used in biomedical research and clinical medicine. Investigation/scanning more and different types of inorganic and organic molecules will be our next step. The availability of a library of spectra recorded from various molecules will allow us to use SI in many medical applications.

Supplementary Information

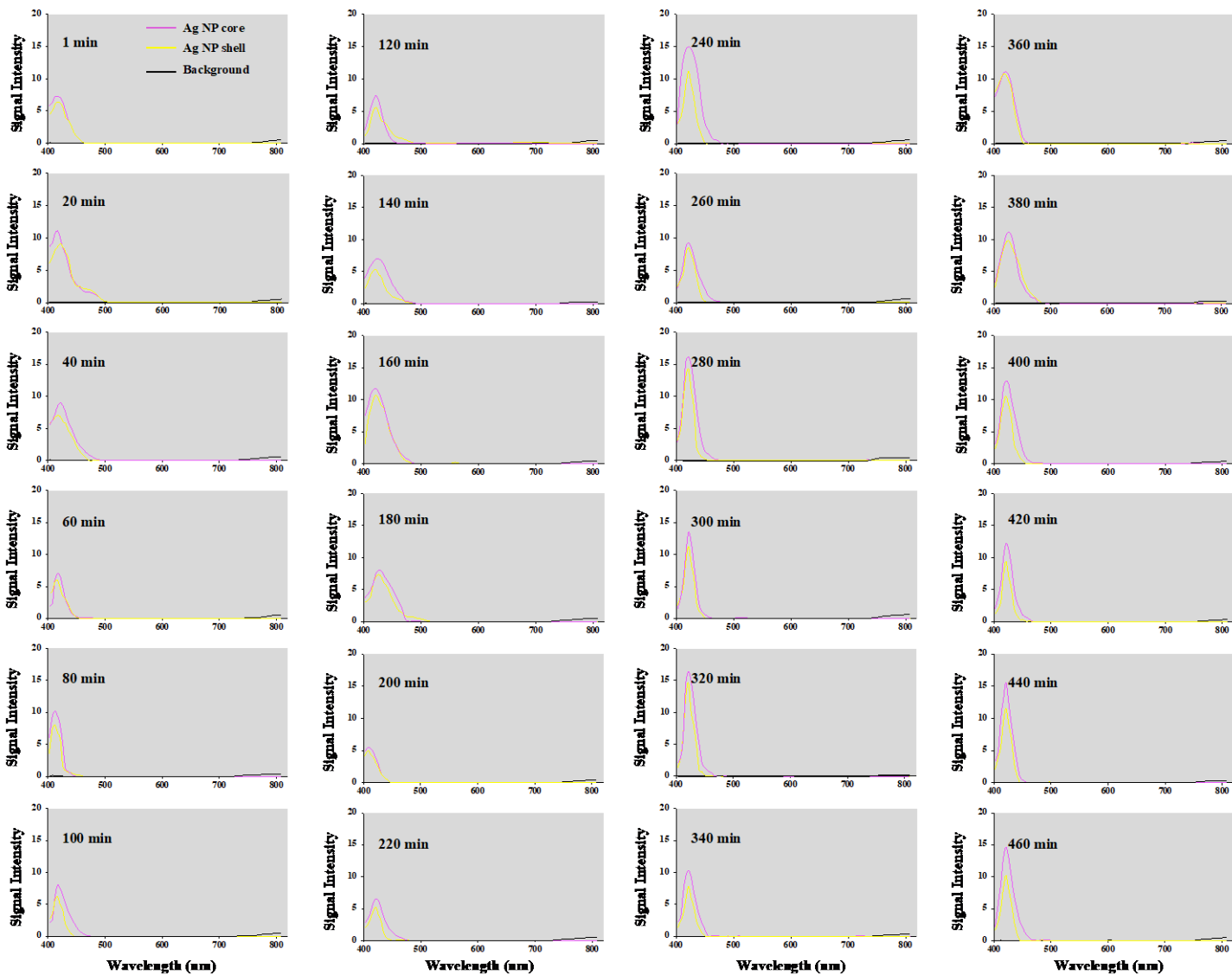


Supp Fig 1. UV-VIS spectra of Ag(s)-NPs (a) and Au-NPs (b) with maximum wavelengths at 420 and 536 nm, respectively. Different lines represent different concentrations. The middle panels present the magnified areas of NPs peaks. The lower panels show linear regression analysis of the corresponding peaks of Au-NPs and Ag(s)-NPs at different concentrations.

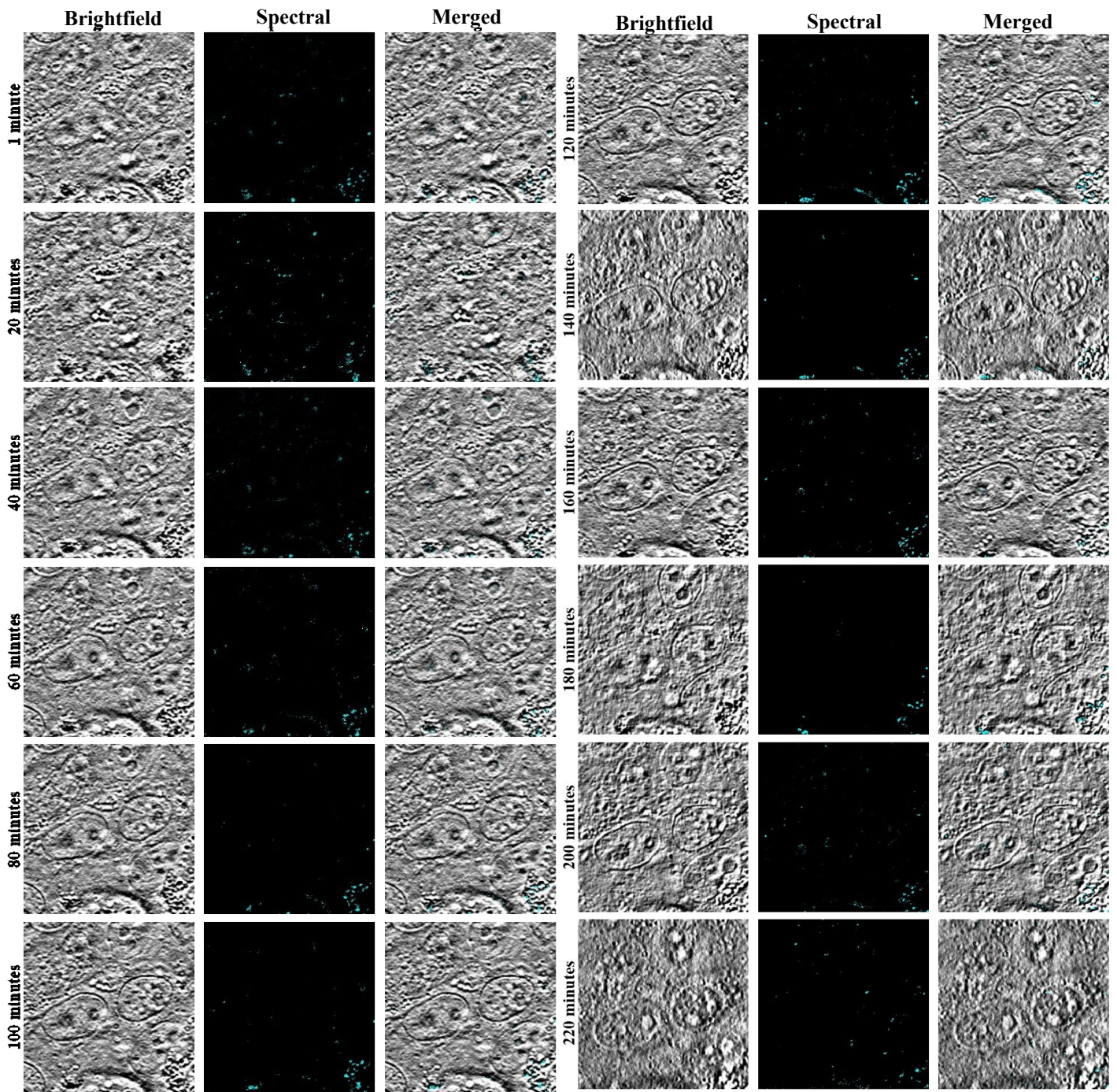


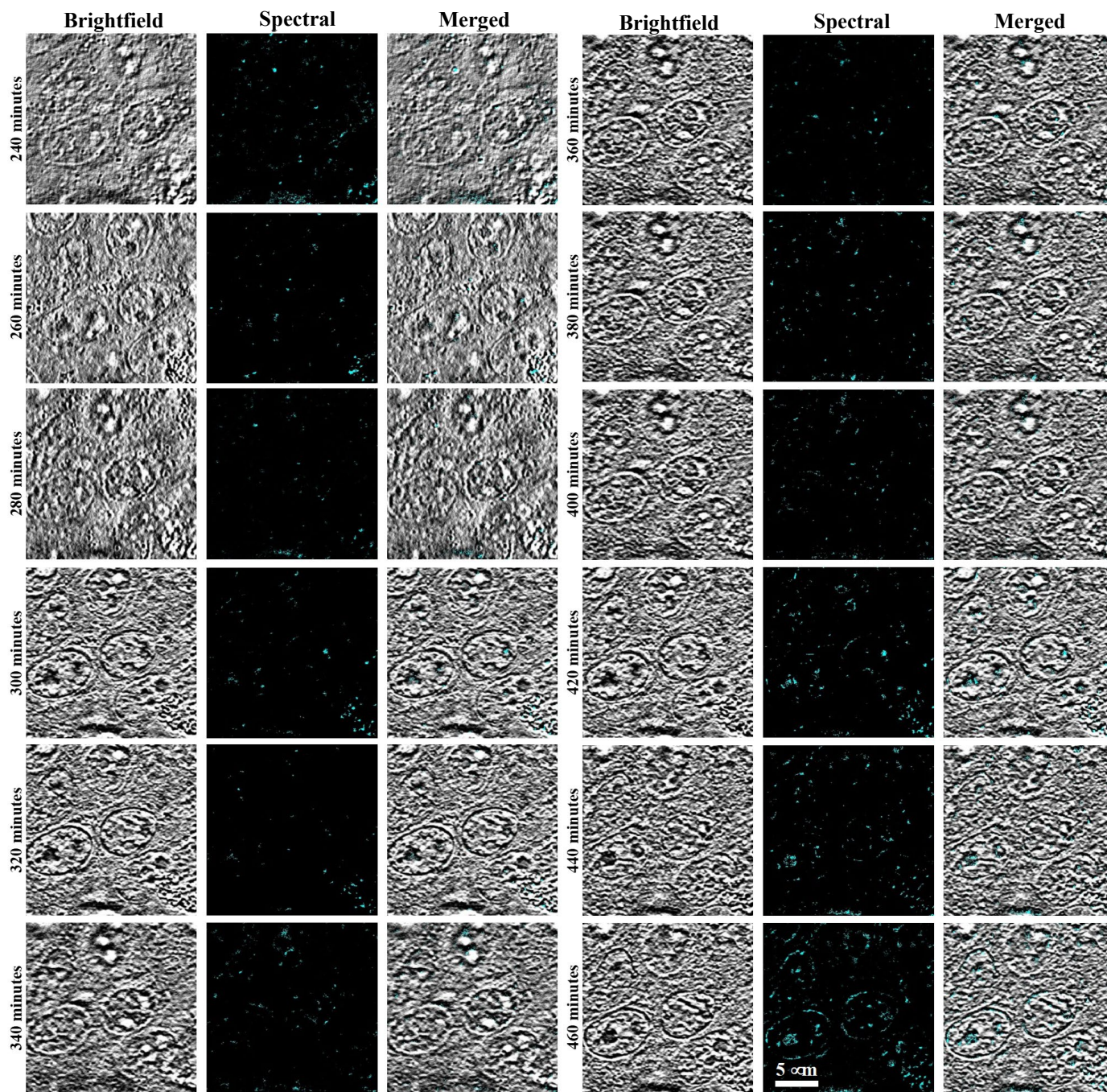


Supp Fig 2. Time-lapse imaging for the cells treated with 0.1 mg of Ag(s)-NPs in 2mL media. Images were captured every 20 minutes for about 8 hours. Over time, the number of Ag(s)-NPs increases in the nucleoplasm area.

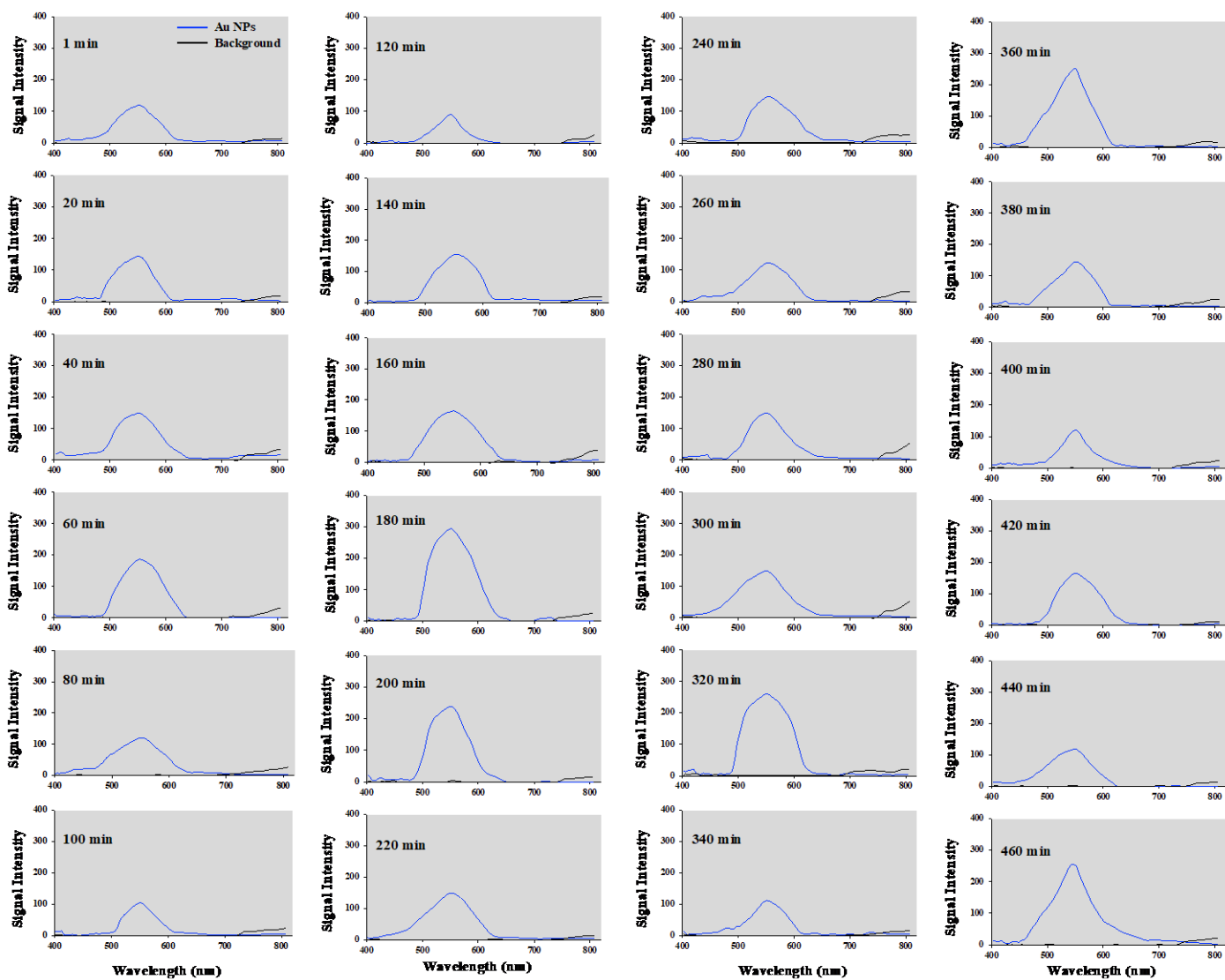


Supp Fig 3. Different graphs represent different Ag(s)-NP wavelengths. The pink lines represent the core area of Ag(s)-NPs, while the yellow lines show the shell of Ag(s)-NPs. The black lines represent the background area.

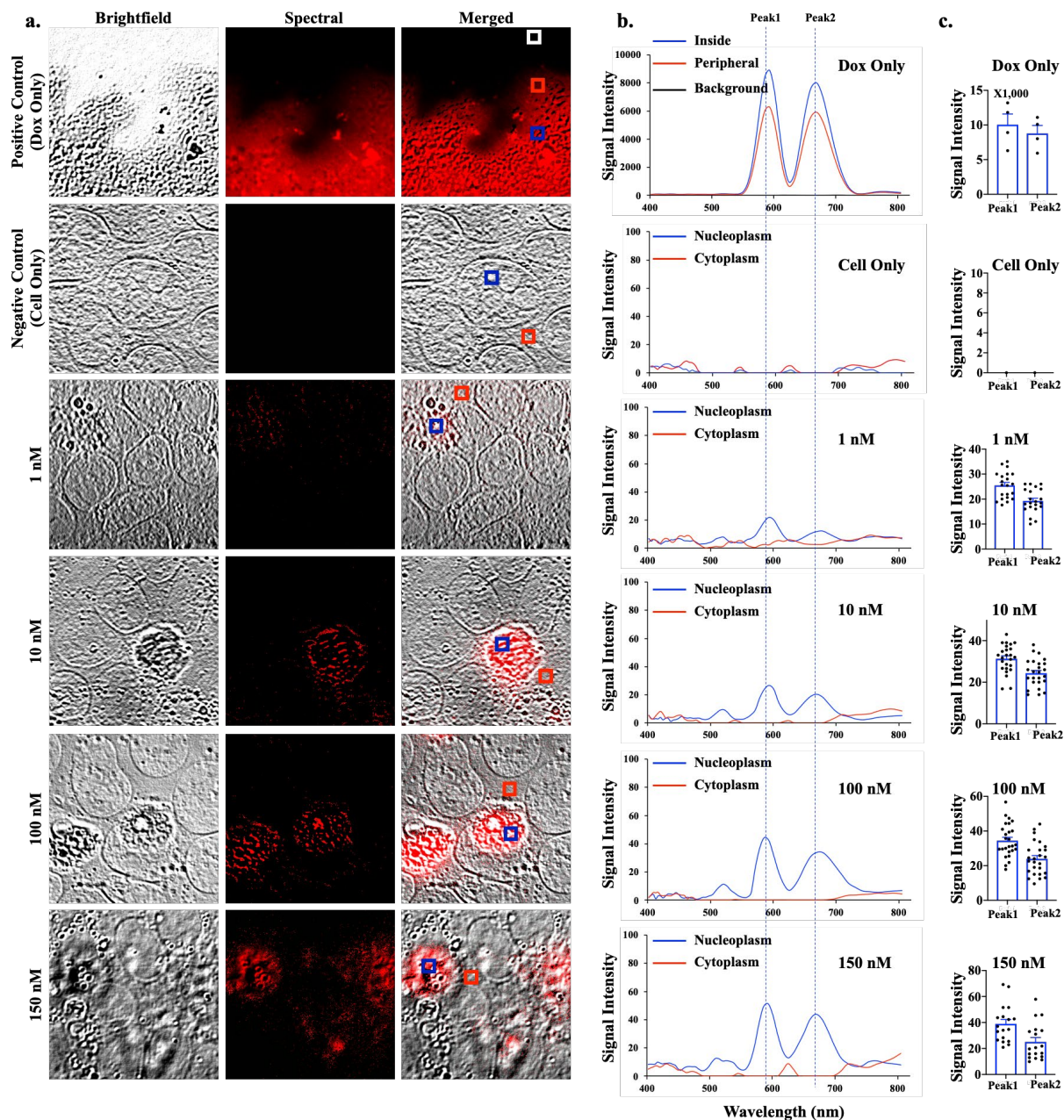




Supp Fig 4. Time-lapse imaging for the cells treated with Au-NPs. Images were captured every 20 minutes for 7 hours and 40 minutes. Over time, the number of Au-NPs increased in the nucleoplasm area.

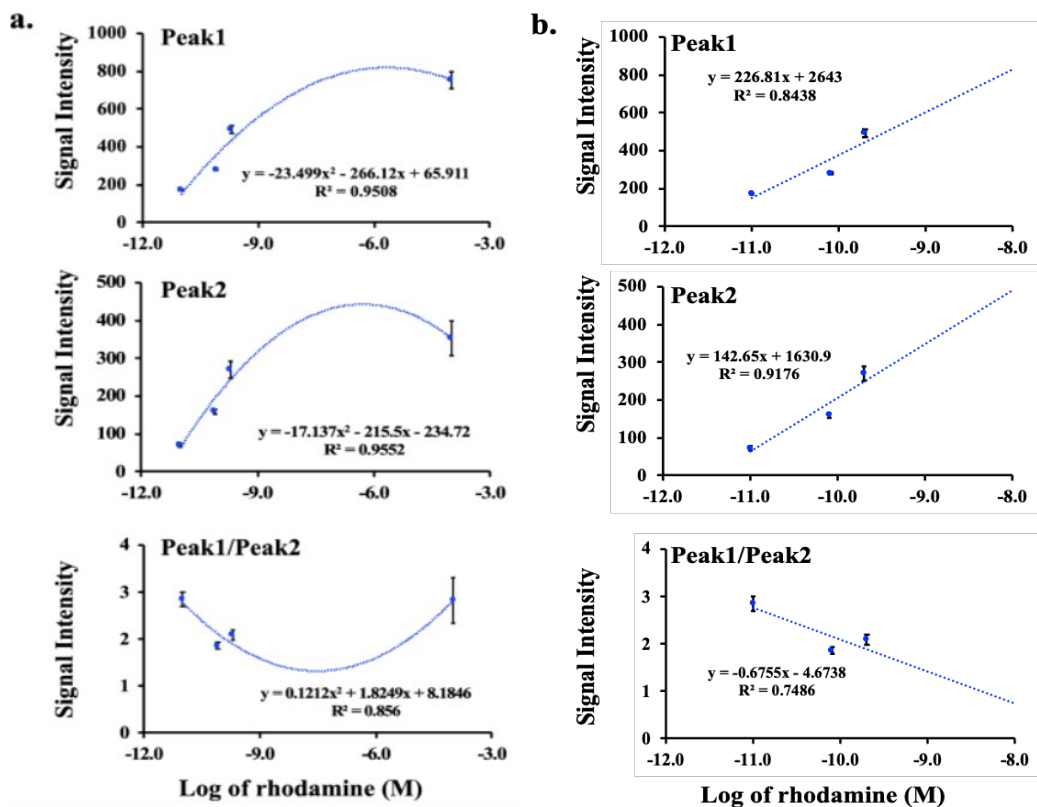


Supp Fig 5. Different graphs represent different Au-NPs cluster wavelengths with blue color, while black color exemplifies the background area.

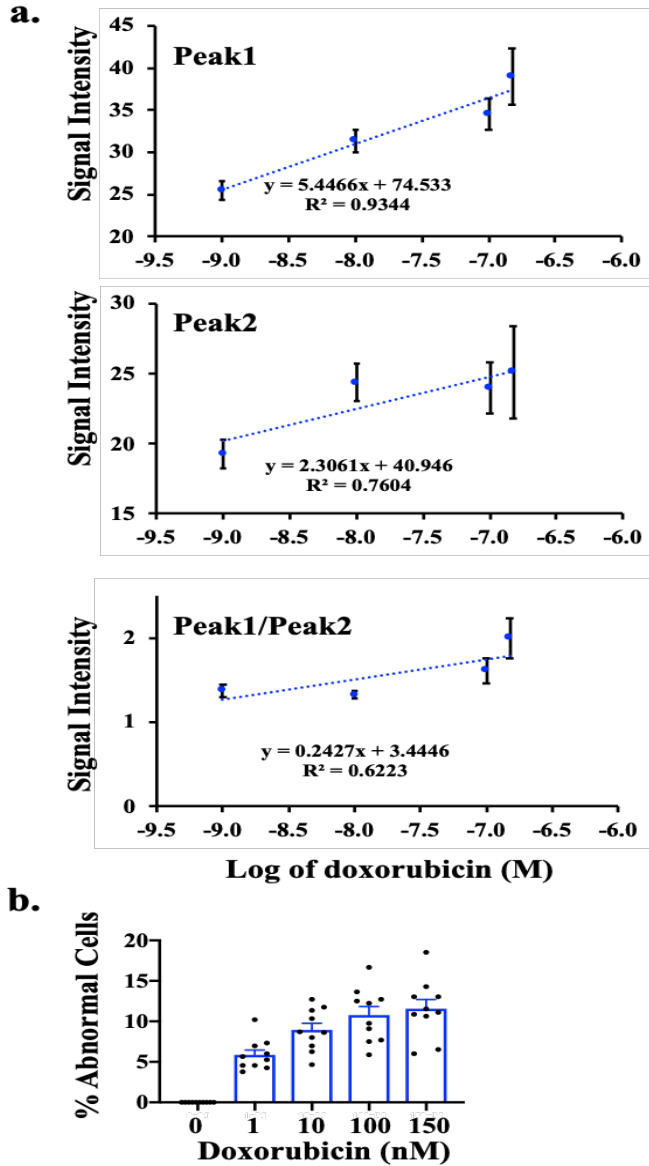


Supp Figure 6. Spectral imaging on dox.

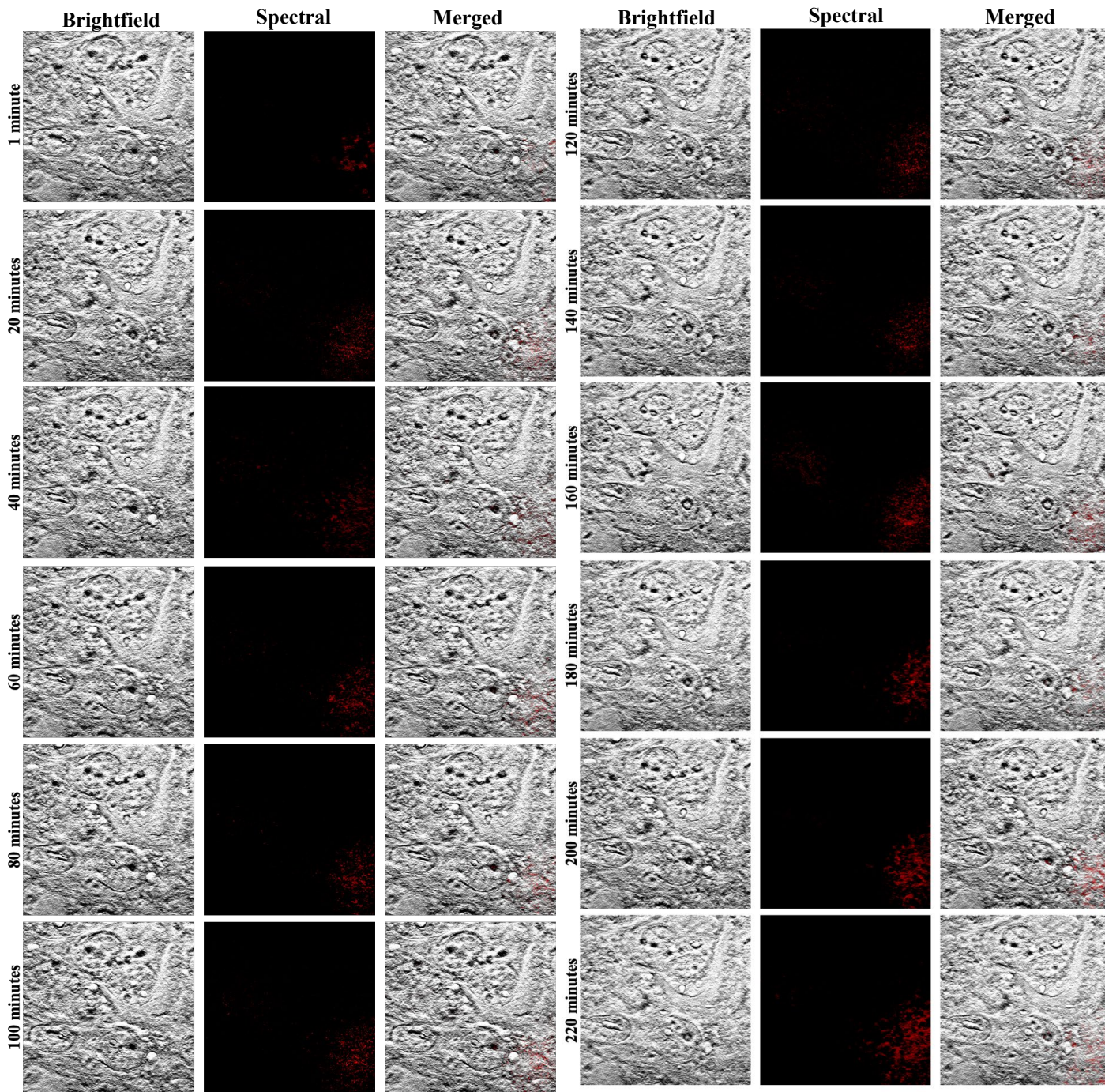
(a) Brightfield, emission spectral and merged images of dox-only (dissolved dox as a positive control), non-treated cells (negative control), and 18-h dox-treated cells at various concentrations. Cells were then fixed and imaged. White box = background; red box = lower signal intensity; blue box = higher signal intensity for dox. (b) The graphs show the spectra characteristics of dox, showing peaks at 592 nm (Peak1) and 670 nm (Peak2). (c) The bar graphs exhibit the variations of the intensity data points for Peak1, which was higher than Peak2. N = 4 (control groups) and N ≥ 20 (treatment groups). Scale Bar = 10 μm.

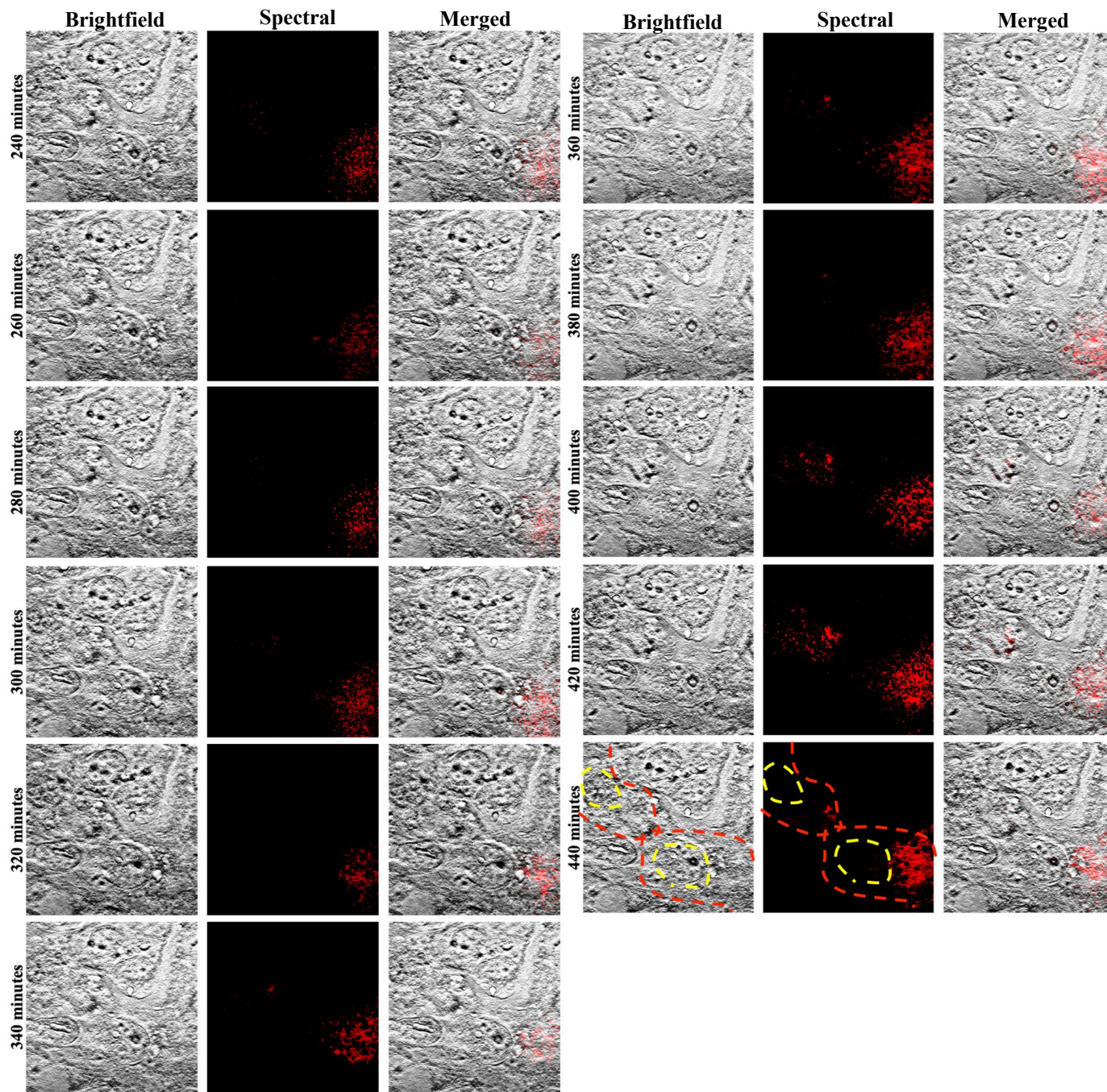


Supp Figure 7. Analysis of linearity of rhodamine in spectral imaging. Linear regression data analyses of the cells treated with different concentrations of rhodamine 6G with spectral imaging. The graphs represent the average intensities of Peak1 at 580 nm, Peak2 at 679 nm, or the ratio of Peak1/Peak2, which included the saturation point at 100 μ M **(a)** or without the saturation point **(b)**. $N \geq 20$.

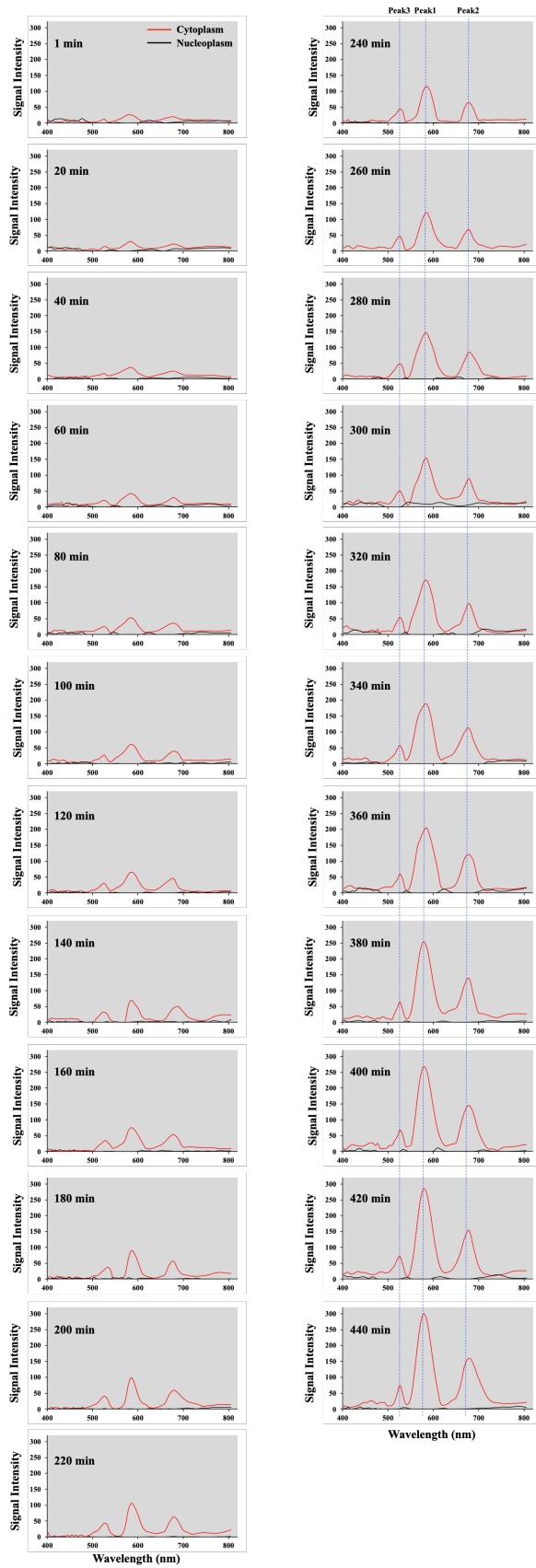


Supp Figure 8. Analysis of linearity of dox in spectral imaging. **(a)** Linear regression for the cells treated with dox captured from spectral imaging. The graphs illustrate the average intensities of Peak1 at 592 nm, Peak2 at 670, and the ratio of Peak1/Peak2. $N \geq 20$. **(b)** The bar graph displays the percentage of the abnormal cells (or dead cells) at different concentrations of dox. At least 50 cells were counted in $N \geq 9$ independent experiments.

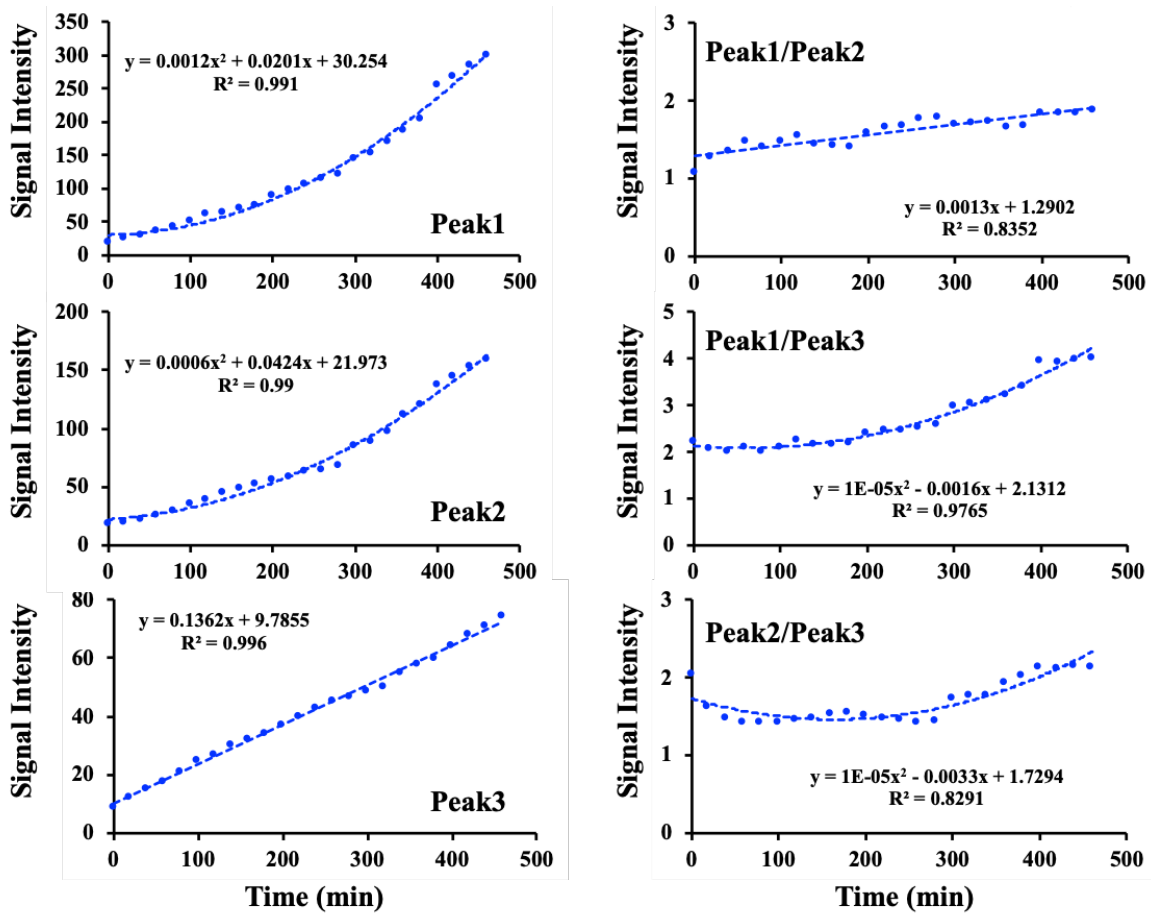




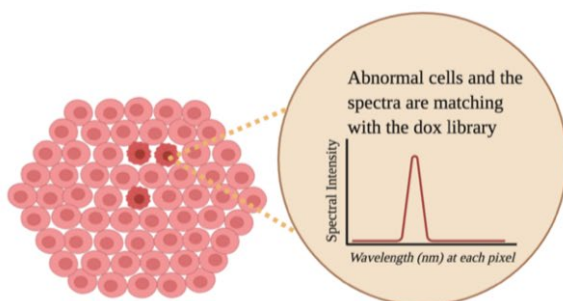
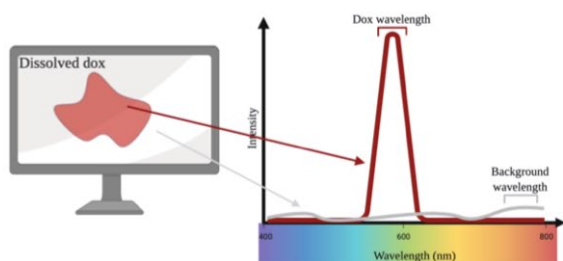
Supp Fig 9. Time-lapse imaging for the cells that treated with 0.01 nM rhodamine. Images were captured every 20 minutes for 440 minutes. Rhodamine accumulated in the cytoplasm more than in the nucleoplasm.



Supp Fig 10. Line graphs represent rhodamine wavelengths at different time points. The wavelength intensity increases over time. Red line represents the cytoplasm area, while black shows the background region, which is in the nucleoplasm.



Supp Fig 11. The left panels show the analyses of time-lapse imaging data points for the cells treated with rhodamine for Peak1 (580 nm), Peak2 (679 nm) and Peak3 (515 nm). The right panels represent the ratios of different peaks.



1

The spectral characteristics of a known drug or chemical is recorded. The spectral characteristics contains transmission, absorption and emission information of the drug. This information is subsequently stored in a library for identification of the same drug in future studies.

2

In our studies, brightfield image and spectral information are captured and collected. Brightfield image is used to visualize and identify the cell organelles. Drug-specific spectral can be recalled from the library, and this extracted information is then converted to a pseudocolored image, where each pixel of the image contains drug-specific spectra information.

3

The brightfield image and pseudocolored image can be merged to extract information about drug distribution and metabolism within a specific subcellular localization in a single cell.

Supp Fig 12. Overview of the spectral imaging workflow. The first step is to make a spectral library for the chemical of interest. The second step is to take an image and collect its spectral information. The third step is to use the spectral library to identify spectral of the chemical of interest from the image.